

1 SEARCH FOR $t\bar{t}Z' \rightarrow t\bar{t}t\bar{t}$ PRODUCTION IN THE MULTILEPTON FINAL STATE IN
2 pp COLLISIONS AT $\sqrt{s} = 13$ TEV WITH THE ATLAS DETECTOR

By

Hieu Le

A DISSERTATION

Submitted to
Michigan State University
in partial fulfillment of the requirements
for the degree of

Physics — Doctor of Philosophy

2025

ABSTRACT

13 Lorem ipsum dolor sit amet, consectetur adipiscing elit, sed do eiusmod tempor incididunt ut
14 labore et dolore magna aliqua. Ut enim ad minim veniam, quis nostrud exercitation ullamco
15 laboris nisi ut aliquip ex ea commodo consequat. Duis aute irure dolor in reprehenderit in
16 voluptate velit esse cillum dolore eu fugiat nulla pariatur. Excepteur sint occaecat cupidatat
17 non proident, sunt in culpa qui officia deserunt mollit anim id est laborum.

ACKNOWLEDGMENTS

- ¹⁹ Advisor: Reinhard Schwienhorst
- ²⁰ Postdoc: Binbin Dong
- ²¹ Committee
- ²² MSU group
- ²³ ATLAS analysis group
- ²⁴ Friend: Daniel, Grayson, Bella, Eric, Jordan
- ²⁵ Other friends: Jasper, Adam, Brittany
- ²⁶ Parents
- ²⁷ Spouse: Allen Sechrist
- ²⁸ ATLAS in general & funding agencies

PREFACE

³⁰ This is my preface. remarks remarks remarks

TABLE OF CONTENTS

31	List of Tables	vii
32	List of Figures	ix
33	KEY TO ABBREVIATIONS	xi
34	Chapter 1. Introduction	1
35	Chapter 2. Theoretical Overview	5
36	2.1 The Standard Model	5
37	2.1.1 Elementary particles	5
38	2.1.2 Mathematical formalism	9
39	2.1.2.1 Quantum chromodynamics	10
40	2.1.2.2 Electroweak theory	11
41	2.1.2.3 Higgs mechanism	14
42	2.2 Beyond the Standard Model	17
43	2.2.1 Top-philic vector resonance	17
44	2.2.2 BSM $t\bar{t}Z' \rightarrow t\bar{t}t\bar{t}$	19
45	2.2.3 Current exclusion limits	20
46	Chapter 3. LHC & ATLAS Experiment	22
47	3.1 The Large Hadron Collider	22
48	3.1.1 Overview	22
49	3.1.2 LHC operations	24
50	3.1.3 Physics at the LHC	25
51	3.2 The ATLAS detector	25
52	3.2.1 Inner detector	28
53	3.2.2 Calorimeter systems	29
54	3.2.3 Muon spectrometer	31
55	3.2.4 Trigger & data acquisition	33
56	Chapter 4. Particle Reconstruction & Identification	34
57	4.1 Primary reconstruction	34
58	4.1.1 Tracks	34
59	4.1.2 Vertices	35
60	4.1.3 Topological clusters	36
61	4.2 Jets	37
62	4.2.1 Jet reconstruction	38
63	4.2.2 Flavor tagging	39
64	4.3 Leptons	43
65	4.3.1 Electrons	43
66	4.3.2 Muons	46

67	4.4	Missing transverse momentum	48
68	4.5	Overlap removal	49
69	Chapter 5. Data & Simulated Samples	50
70	5.1	Data samples	50
71	5.2	Monte Carlo samples	50
72	5.2.1	$t\bar{t}Z'$ signal samples	51
73	5.2.2	Background samples	53
74	Chapter 6. Analysis Strategy	55
75	6.1	Event selection	55
76	6.1.1	Object definition	56
77	6.1.2	Event categorization	56
78	6.2	Analysis regions	57
79	6.2.1	Signal regions	59
80	6.2.2	Control regions	62
81	6.3	Background estimation	64
82	6.3.1	Template fitting for fake/non-prompt estimation	65
83	6.3.2	Charge misidentification data-driven estimation	65
84	6.3.3	$t\bar{t}W$ background data-driven estimation	67
85	Chapter 7. Systematic Uncertainties	70
86	7.1	Experimental uncertainties	70
87	7.1.1	Luminosity & pile-up reweighting	70
88	7.1.2	Leptons	70
89	7.1.3	Jets	72
90	7.1.4	Missing transverse energy	74
91	7.2	Modeling uncertainties	75
92	7.2.1	Signal and irreducible background uncertainties	75
93	7.2.2	Reducible background uncertainties	77
94	Chapter 8. Results	79
95	8.1	Statistical interpretation	79
96	8.1.1	Profile likelihood fit	79
97	8.1.2	Exclusion limit	82
98	8.2	Fit results	83
99	Chapter 9. Summary	89
100	References	90

¹⁰¹ List of Tables

¹⁰² Table 4.1: Overlap removal process for this analysis, applied sequentially from top to bottom	¹⁰³ 49
¹⁰⁴ Table 5.1: Summary of all HLT triggers used in this analysis. Events are required to pass at least one trigger	¹⁰⁵ 51
¹⁰⁶ Table 5.2: Summary of all Monte-Carlo samples used in this analysis. V refers to an EW ($W^\pm/Z/\gamma^*$) or Higgs boson. Matrix element (ME) order refers to the order in QCD of the perturbative calculation. Tune refers to the underlying-event tune of the parton shower (PS) generator.	¹⁰⁷ 52
¹¹⁰ Table 6.1: Summary of object selection criteria used in this analysis. ℓ_0 refers to the leading lepton in the event.	¹¹¹ 56
¹¹² Table 6.2: Definitions of signal, control and validation regions (VR) used in this analysis. N_{jets} and N_b refers to the number of jets and number of b -tagged jets respectively. ℓ_1 refers to the leading lepton, ℓ_2 refers to the subleading lepton and so on. H_T refers to the p_T scalar sum of all leptons and jets in the event. $m_{\ell\ell}$ refers to the dilepton invariant mass, which must not coincide with the Z -boson mass range of 81-101 GeV for SS2L+3L events.	¹¹³ 58
¹¹⁸ Table 6.3: Definitions of SR sub-regions. Events are sorted into different sub-regions based on the number of b -tagged jets and leptons present.	¹¹⁹ 60
¹²⁰ Table 6.4: List of possible assigned values for DFCAA.	63
¹²¹ Table 7.1: Summary of the experimental systematic uncertainties considered in this analysis.	¹²² 71
¹²³ Table 8.1: Normalization factors for backgrounds with dedicated CRs, obtained from a simultaneous fit in all CRs and SR under the background-only hypothesis. The nominal pre-fit value is 1 for all NFs and 0 for the scaling factors a_0 and a_1 . Uncertainties shown include both statistical and systematic uncertainties.	¹²⁴ 86
¹²⁵	¹²⁶

¹³⁸ List of Figures

¹³⁹ Figure 2.1: Particles within the SM and their properties.	6
¹⁴⁰ Figure 2.2: Feynman diagram for $t\bar{t}$ production and subsequent decay processes. Top quark decays into a W -boson and b -quarks, and W -boson can decay to a $q\bar{q}$ or a $\ell\nu_\ell$ pair.	¹⁴¹ 8
¹⁴²	
¹⁴³ Figure 2.3: Illustration of a common representation of the Higgs potential. Before SSB, the ground state $\phi(0)$ is located at A which is symmetric with respect to the potential. A perturbation to this state fixes the ground state energy $ \phi(0) ^2$ to a particular value at B, "spontaneously" breaking the symmetry and degeneracy in $ \phi(0) ^2$	¹⁴⁴ 15
¹⁴⁵	
¹⁴⁶	
¹⁴⁷	
¹⁴⁸ Figure 2.4: Feynman diagrams for tree level Z' production in association with (a) $t\bar{t}$, (b) tj (light quark) and (c) tW , decaying to final states containing (a) $t\bar{t}t\bar{t}$ or (b)(c) $t\bar{t}t$	¹⁴⁹ 19
¹⁵⁰	
¹⁵¹ Figure 2.5: Caption	20
¹⁵² Figure 2.6: Branching ratios for $t\bar{t}t\bar{t}$ decay. The same-sign dilepton and multilepton channels together forms the SSML channel.	¹⁵³ 20
¹⁵⁴ Figure 3.1: The full CERN accelerator complex as of 2022.	23
¹⁵⁵ Figure 3.2: Current and future timeline of LHC operations as of 2025 with corresponding center-of-mass energies and projected integrated luminosities. . .	¹⁵⁶ 24
¹⁵⁷ Figure 3.3: Summary of predicted and measured cross-section for SM processes at the LHC at different center-of-mass energies	¹⁵⁸ 26
¹⁵⁹ Figure 3.4: A cross section slice of the ATLAS detector showing different subsystems along with visualization of different types of particles traveling through the detector	¹⁶⁰ 27
¹⁶¹	
¹⁶² Figure 3.5: Cutaway illustration of the inner detector along with its subsystems. . .	28

163	Figure 3.6: Cutaway illustration of the calorimeter system including the EM, hadronic 164 and LAr forward calorimeters	30
165	Figure 4.1: Stages of topo-cluster formation corresponding to each threshold. In (a), 166 proto-clusters are seeded from cells with adequate signal significance $\zeta_{\text{cell}}^{\text{EM}}$. 167 The clusters are further merged and split in (b) according to a predefined 168 cluster growth threshold. The process stops in (c) when all sufficiently 169 significant signal hits have been matched to a cluster.	37
170	Figure 4.2: Jet energy scale calibration sequence for EM-scale jets.	39
171	Figure 4.3: Overview of the GN2 architecture. The number of jet and track features 172 are represented by n_{jf} and n_{tf} respectively. The global jet representation 173 and track embeddings output by the Transformer encoder are used as 174 inputs for three task-specific networks.	41
175	Figure 4.4: The c -, light- and τ -jet rejection rate as a function of b -tagging efficiency 176 for GN2 and DL1d using (a) jets in the $t\bar{t}$ sample, and (b) jets in the Z' 177 sample. The performance ratios of GN2 to DL1d are shown in the bottom 178 panels.	42
179	Figure 6.1: Post-fit background composition in each analysis region and sub-region. 180 The fit was performed using ideal pseudo-datasets (Asimov data) in the SR.	59
181	Figure 6.2: Caption	61
182	Figure 6.3: Charge flip rate calculated for SR and CR $t\bar{t}W$ in bins of $ \eta $ and p_{T}	67
183	Figure 7.1: Combined QmisID uncertainty rate for SR in bins of $ \eta $ and p_{T}	78
184	Figure 8.1: Observed (solid line) and expected (dotted line) upper limits as a function 185 of the Z' mass at 95% CL on the cross-section of $pp \rightarrow t\bar{t}Z'$ production 186 times the $Z' \rightarrow t\bar{t}$ branching ratio. The region above the observed limit is 187 excluded. The solid blue line represents the theoretical signal cross-section 188 with $c_t = 1$ at LO in QCD. The green and yellow bands represent the 189 68% ($\pm\sigma$) and 95% ($\pm 2\sigma$) confidence intervals respectively.	84
190	Figure 8.2: Comparison between data and post-fit prediction for the discriminant ob- 191 servable in each non-prompt and $t\bar{t}W$ background CR. The fit is per- 192 formed simultaneously in all CRs and SR under the background-only 193 hypothesis. The lower panel shows the ratio between data and post-fit 194 predictions. The shaded band represents the total uncertainty on the fit.	85

KEY TO ABBREVIATIONS

Physical & Mathematical Quantities

¹⁹⁷ χ^2 chi-squared

¹⁹⁸ d_0 transverse impact parameter

¹⁹⁹ ΔR angular distance

²⁰⁰ \sqrt{s} center-of-mass energy

²⁰¹ η pseudorapidity

²⁰² E_T transverse energy

²⁰³ E_T^{miss} missing transverse energy

²⁰⁴ Γ decay width

²⁰⁵ γ_5 chirality projection operator

²⁰⁶ γ_μ Dirac matrices

²⁰⁷ H_0 null hypothesis

²⁰⁸ H_T scalar sum of transverse momenta p_T of all objects in an event

²⁰⁹ \mathcal{L} Lagrangian

²¹⁰ $\mathcal{L}(\theta)$ likelihood function

²¹¹ L instantaneous luminosity

²¹² $m_{\ell\ell}$ dilepton invariant mass

²¹³ μ signal strength

²¹⁴ μ_F factorization scale

²¹⁵ μ_R renormalization scale

²¹⁶ N_{jets} number of jets/jet multiplicity

²¹⁷ $\mathcal{O}(n)$ on the order of n

²¹⁸ \mathcal{P} Poisson probability

²¹⁹ p_T transverse momentum

- ²²⁰ Q electric charge
²²¹ q_μ profile likelihood ratio
²²² σ standard deviation
²²³ $\sigma[b]$ cross-section
²²⁴ z_0 longitudinal impact parameter

Particles & Processes

- ²²⁵
- ²²⁶ γ^* virtual photon
²²⁷ gg gluon-gluon fusion
²²⁸ pp proton-proton
²²⁹ PbPb lead-lead
²³⁰ q quark
²³¹ $q\bar{q}$ quark-antiquark pair
²³² $t\bar{t}$ top/anti-top quark pair
²³³ $t\bar{t}X$ top pair in association with another particle
²³⁴ $t\bar{t}t\bar{t}$ four-top-quark
²³⁵ V massive vector bosons (W^\pm, Z)
²³⁶ H Higgs in association with a vector boson

Acronyms

- ²³⁷
- ²³⁸ **1LOS** one lepton, or two leptons of opposite charges
²³⁹ **2HDM** two-Higgs doublet model
²⁴⁰ **AF3** AtlFast3 fast simulation
²⁴¹ **ALICE** A Large Ion Collider Experiment
²⁴² **ATLAS** A Toroidal LHC ApparatuS
²⁴³ **AWAKE** Advanced WAKEfield Experiment
²⁴⁴ **BDT** boosted decision tree
²⁴⁵ **BR** branching ratio

- ²⁴⁶ **BSM** Beyond the Standard Model
- ²⁴⁷ **CB** combined muon
- ²⁴⁸ **CERN** European Organization for Nuclear Research
- ²⁴⁹ **CKM** Cabibbo-Kobayashi-Maskawa matrix
- ²⁵⁰ **CL** confidence level
- ²⁵¹ **CMS** Compact Muon Solenoid
- ²⁵² **CP** charge-parity symmetry
- ²⁵³ **CR** control region
- ²⁵⁴ **CSC** Cathode Strip Chambers
- ²⁵⁵ **CTP** Central Trigger Processor
- ²⁵⁶ **ECIDS** Electron Charge ID Selector
- ²⁵⁷ **EFT** effective field theory
- ²⁵⁸ **EM** electromagnetic
- ²⁵⁹ **EW** electroweak
- ²⁶⁰ **FASER** ForwArd Search ExpeRiment
- ²⁶¹ **FCal** forward calorimeter
- ²⁶² **FS** full detector simulation
- ²⁶³ **GNN** graph neural network
- ²⁶⁴ **GRL** Good Run List
- ²⁶⁵ **GSC** Global Sequential Calibration
- ²⁶⁶ **GSF** Gaussian-sum filter
- ²⁶⁷ **GUT** Grand Unified Theory
- ²⁶⁸ **HEC** hadronic endcap calorimeter
- ²⁶⁹ **HF** heavy-flavor
- ²⁷⁰ **HL-LHC** High-Luminosity Large Hadron Collider
- ²⁷¹ **HLT** High-Level Trigger
- ²⁷² **ID** Inner Detector

- ²⁷³ **IP** interaction point
- ²⁷⁴ **JER** jet energy resolution
- ²⁷⁵ **JES** jet energy scale
- ²⁷⁶ **JVT** Jet Vertex Tagger
- ²⁷⁷ **KATRIN** Karlsruhe Tritium Neutrino Experiment
- ²⁷⁸ **L1** Level 1
- ²⁷⁹ **LAr** liquid argon
- ²⁸⁰ **LF** light-flavor
- ²⁸¹ **LH** likelihood
- ²⁸² **LHC** Large Hadron Collider
- ²⁸³ **LHCb** Large Hadron Collider beauty
- ²⁸⁴ **LINAC** linear accelerator
- ²⁸⁵ **LLH** log-likelihood
- ²⁸⁶ **LO** leading order
- ²⁸⁷ **MC** Monte Carlo simulation
- ²⁸⁸ **ME** matrix element
- ²⁸⁹ **ML** multilepton
- ²⁹⁰ **MS** Muon Spectrometer
- ²⁹¹ **MDT** Monitored Drift Tubes
- ²⁹² **MET** missing transverse energy
- ²⁹³ **NF** normalization factor
- ²⁹⁴ **NNJvt** Neural Network-based Jet Vertex Tagger
- ²⁹⁵ **NLO** next-to-leading order
- ²⁹⁶ **NNLO** next-to-next-to-leading order
- ²⁹⁷ **NP** nuisance parameter
- ²⁹⁸ **OP** operating point (also working point)
- ²⁹⁹ **OS** opposite-sign

- ³⁰⁰ **PCBT** pseudo-continuous *b*-tagging
- ³⁰¹ **PDF** parton distribution function
- ³⁰² **POI** parameter of interest
- ³⁰³ **PS** parton shower
- ³⁰⁴ **PV** primary vertex
- ³⁰⁵ **QCD** quantum chromodynamics
- ³⁰⁶ **QED** quantum electrodynamics
- ³⁰⁷ **QFT** quantum field theory
- ³⁰⁸ **QmisID** charge mis-identification
- ³⁰⁹ **RPC** Resistive Plate Chamber
- ³¹⁰ **SCT** Semiconductor Tracker
- ³¹¹ **SF** scale factor
- ³¹² **SM** Standard Model
- ³¹³ **SR** signal region
- ³¹⁴ **SS** same-sign
- ³¹⁵ **SSB** spontaneous symmetry breaking
- ³¹⁶ **SS2L** same-sign dilepton
- ³¹⁷ **SSML** same-sign dilepton, or more than two leptons of any charges
- ³¹⁸ **TDAQ** Trigger and Data Acquisition
- ³¹⁹ **TGC** Thin-Gap Chamber
- ³²⁰ **TRT** Transition Radiation Tracker
- ³²¹ **VEV** vacuum expectation value
- ³²² **VR** validation region
- ³²³ **UE** underlying-event

³²⁴ Chapter 1. Introduction

³²⁵ The 20th century ushered in a revolutionary period for mankind's understanding of the
³²⁶ fundamental nature of matter and the forces that govern our universe with the development
³²⁷ of special relativity and quantum mechanics, which redefined our understanding of space,
³²⁸ time, energy and matter at the furthest extremes of scale from the vast reaches of the cosmos
³²⁹ to the tiniest constituents of matter. Building on these principles, Quantum Electrodynamics
³³⁰ (QED) [1–3] was developed as the first successful quantum field theory (QFT) describing
³³¹ electromagnetism. The discovery of beta decay [4] and its paradoxical behaviors within the
³³² framework of QED prompted the prediction of neutrinos and development of the theory of
³³³ weak interaction.

³³⁴ At around the same time, a spectrum of strongly interacting particles was discovered
³³⁵ [5] as particle accelerators probed deeper into atomic nuclei, leading to the formation of
³³⁶ the quark model in the 1960s and with it a hypothesized new binding force, the strong
³³⁷ force. However, the QFT framework remained incapable of describing the weak and strong
³³⁸ interactions until advancements in gauge theory and the quantization of non-Abelian gauge
³³⁹ via QFT resulted in the formation of Yang-Mills theory [6, 7]. This sparked a renaissance
³⁴⁰ in modern physics with the unification of electromagnetism and weak force in 1967 under
³⁴¹ the framework of electroweak (EW) [8] theory, as well as the development of Quantum
³⁴² Chromodynamics (QCD) [9, 10] to describe the strong force binding quarks.

³⁴³ At this point, the prediction of massless bosons within EW formalism remained a contra-
³⁴⁴ diction to the predicted massive W^\pm and Z bosons that mediate the weak force. This was
³⁴⁵ resolved by the introduction of EW spontaneous symmetry breaking and the Higgs mech-
³⁴⁶ anism in 1964 [11–13], which explained the generation of masses for both the EW bosons

347 and fermions. Together, these developments culminated in the Standard Model of parti-
348 cle physics SM [14], a comprehensive theory that described the electromagnetic, weak, and
349 strong interactions, classified all known fundamental particles and predicted mathematically
350 consistent but not yet observed particles. Following its inception, particles predicted by the
351 Standard Model were gradually observed experimentally, starting with the gluon in 1979
352 [15], then the W^\pm and Z bosons [16, 17], and finally the top quark in 1995 [18, 19]. The
353 final missing piece was confirmed as the Higgs boson was observed in 2012 independently
354 by the ATLAS [20] and CMS [21] detectors at the Large Hadron Collider, completing the
355 Standard Model after a 40-year search and cementing it as the most successful framework
356 so far describing fundamental constituents of matter and their governing forces.

357 Despite its successes, the Standard Model remains incomplete. Key unanswered questions
358 include the nature of dark matter [22], which makes up about 27% of the universes energy
359 content but has no explanation within the Standard Model; the origin of neutrino masses and
360 their oscillations [23]; the observed matter-antimatter asymmetry in the universe; possible
361 unification of the EW and strong interaction into a Grand Unified Theory (GUT); and the
362 hierarchy problem describing the large discrepancy in scales between forces and the apparent
363 lightness of the Higgs boson compared to values predicted from quantum corrections.

364 After the discovery of the Higgs boson, efforts have been underway to construct new
365 hypotheses and models in search of beyond the Standard Model (BSM) physics via different
366 avenues, one of which being direct searches at colliders for new resonances or particles not
367 predicted by the SM. In particular, the top quark possesses large mass and strong coupling to
368 the Higgs boson [24] which gives it a special role in many proposed BSM models as a possible
369 connection with strong coupling to new particles and heavy resonances. In addition, the
370 top quark has a clean decay signature with well-understood final states and is produced in

371 abundance at the LHC from pp collisions in the form of top pairs $t\bar{t}$ [25, 26]. This dissertation
372 presents a search for the production of a heavy resonance that couples preferentially to top
373 quark (top-philic) in association with a top pair ($t\bar{t}$) in the final state with either two leptons
374 of the same electric charge or at least three leptons (SSML). The search is performed in
375 proton-proton collisions at $\sqrt{s} = 13$ TeV with the ATLAS detector [27] via the four-top
376 ($t\bar{t}t\bar{t}$) production channel.

377 A similar search for top-philic heavy resonances was performed using a $t\bar{t}t\bar{t}$ final state
378 containing either one lepton or two opposite-sign leptons (1LOS) [28] with a much larger
379 branching ratio of 56% and larger irreducible background of SM processes. Despite the small
380 cross-section within the SM, the $t\bar{t}t\bar{t}$ SSML final state provides heightened sensitivity to BSM
381 physics and higher signal-to-background ratio than inclusive resonance searches (e.g. in dijet
382 or dilepton final states) due to the distinctive signal signature and suppression of large SM
383 background processes present in $t\bar{t}$ -associated production i.e. diboson (VV), $t\bar{t}$ production
384 with an additional boson ($t\bar{t}V/ttH+jets$) or with additional light leptons from heavy-flavor
385 decays ($t\bar{t} + HF$). The cross-section for $t\bar{t}t\bar{t}$ production can be enhanced by many proposed
386 BSM models including supersymmetric gluino pair-production [29, 30], scalar gluon pair-
387 production [31, 32], top-quark-compositeness models [33, 34], effective field theory (EFT)
388 operators [26, 35–38] and two-Higgs-doublet models (2HDM) [39–43]. Searching within this
389 channel is particularly motivated by the recent observed excess in the measurement of four-
390 top production in the SSML final state at the LHC by the ATLAS detector [44] with a
391 measured cross-section of 24^{+7}_{-6} fb, almost double the SM prediction of $13.4^{+1.0}_{-1.8}$ fb.

392 The search attempts to reconstruct the top-philic resonance directly to search for new
393 physics with minimal dependency on the model choice. In addition, a simplified color-
394 singlet vector boson model [45] is employed for model-dependent interpretations, including

395 setting exclusion limits on the production cross-section and model parameters. Data-driven
396 background estimation methods are implemented for $t\bar{t}W$ - one of the dominant irreducible
397 backgrounds in the analysis - and the charge misidentification background to rectify mis-
398 modeling related to jet multiplicity in simulated background that were not covered in the
399 previous 1LOS search [28]. These methods are employed similarly to that in previous SM
400 $t\bar{t}t\bar{t}$ analyses [44, 46].

401 This dissertation is organized as follows. Chapter 2 presents the formalism of the SM and
402 relevant BSM concepts. Chapter 3 provides an introduction to the LHC and ATLAS detector.
403 Chapter 4 describes the reconstruction and identification of physics object from detector
404 signals. Chapter 5 defines the data and simulated samples used in the analysis. Chapter 6
405 describes the analysis strategy, including object definition, analysis region description and
406 background estimation methods. Chapter 7 summarizes the uncertainties involved in the
407 analysis. Chapter 8 presents the statistical interpretation and analysis results. Finally,
408 Chapter 9 discusses a summary of the analysis and future outlook.

409 Chapter 2. Theoretical Overview

410 2.1 The Standard Model

411 The Standard Model of Physics (SM) [47] is currently the most successful formalism to
412 describe the physical world at a microscopic scale by providing descriptions for all currently
413 known elementary particles, along with three out of four fundamental forces (electromag-
414 netism, weak force, strong force) with the exception of gravity. The SM is however not
415 perfect, and there remains unanswered questions that require development and discovery
416 of new physics beyond the Standard Model (BSM). This chapter describes an overview of
417 important components within the SM and relevant BSM aspects for this analysis.

418 2.1.1 Elementary particles

419 Elementary particles in the SM can be classified into two groups: bosons consisting
420 of particles following Bose-Einstein statistics with integer spin, and fermions consisting of
421 particles following Fermi-Dirac statistics with half-integer spin. Fermions are the building
422 blocks of composite particles and consequently all known matter, and can be further classified
423 into quarks & leptons. Bosons act as force mediators for all fundamental forces described by
424 the SM, and can either be a scalar boson with spin 0 or vector gauge bosons with spin 1. For
425 each elementary particle, there also exists a corresponding antiparticle with identical mass
426 and opposite charge (electric or color). Figure 2.1 shows all known elementary particles in
427 the SM.

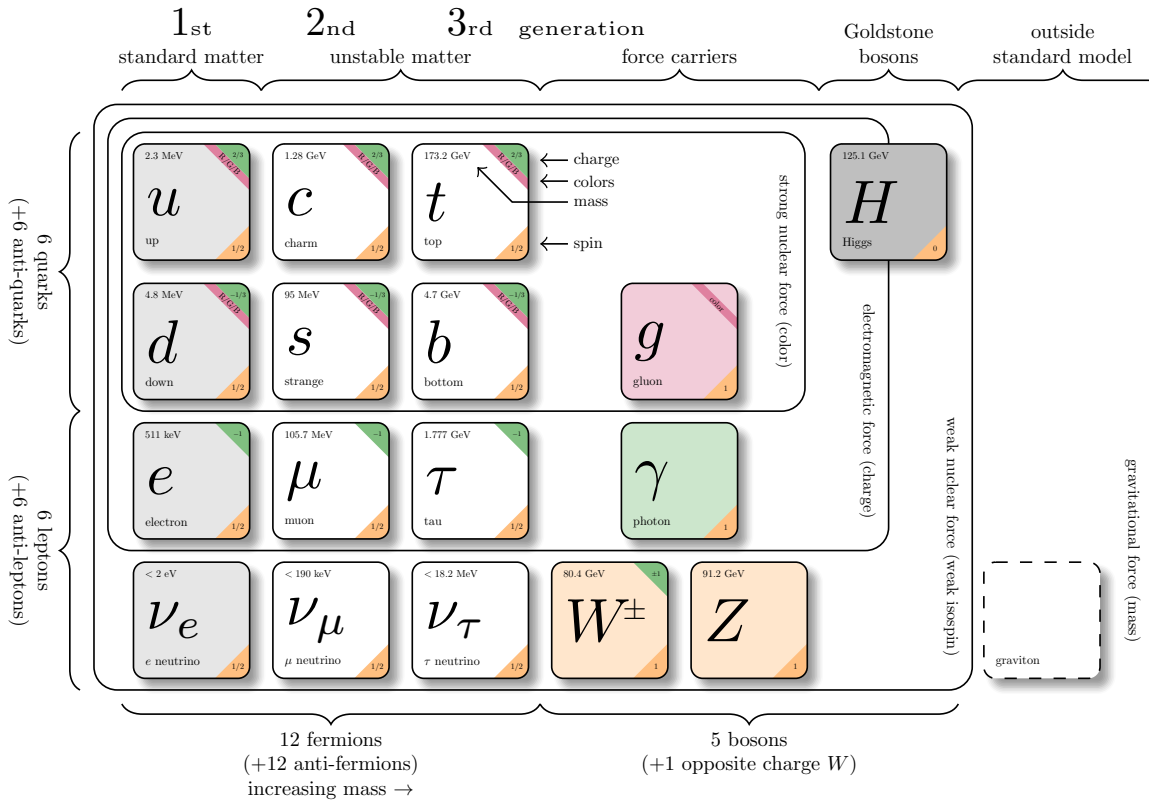


Figure 2.1: Particles within the SM and their properties [48].

428 Fermions

429 Fermions consist of quarks and leptons with six flavors each, grouped into three genera-
 430 tions of doublets. The six quark flavors are up (u), down (d), charm (c), strange (s), bottom
 431 (b) and top (t), arranged in increasing order of mass. The quark flavors form three doublets
 432 (u, d), (c, s) and (t, b), with each doublet containing one quark with electric charge of $+2/3$
 433 (u, s, t), and the other with charge of $-1/3$ (d, c, b). Each quark also possesses a property
 434 known as color charge, with possible values of red (R), green (G), blue (B) or their corre-
 435 sponding anticolor ($\bar{R}, \bar{G}, \bar{B}$). Color charge follows color confinement rules, which allows
 436 only configurations of quarks with total neutral color charge to exist in isolation. Neutral

437 charge configurations can be formed from either a set of three colors (R, G, B), a set of a
438 color and its anticolor, or any combination of the two. Consequently, quarks can only exist
439 in bound states called hadrons and no isolated quark can be found in a vacuum. Quarks are
440 the only elementary particles in the SM that can interact with all four fundamental forces.

441 The three leptons doublets consist of three charged leptons: electron (e), muon (μ), tau
442 (τ), and their respective neutrino flavors: electron neutrino (ν_e), muon neutrino (ν_μ), tau
443 neutrino (ν_τ). Charged leptons carry an electric charge of -1 , while their antiparticles carry
444 the opposite charge ($+1$) and their corresponding neutrino flavors carry no charge. Charged
445 leptons interact with all fundamental forces except the strong force, while neutrinos only
446 interact with the weak force and gravity.

447 Bosons

448 The SM classifies bosons into two types: one scalar boson with spin 0 known as the
449 Higgs (H) boson, and vector gauge bosons with spin 1 known as gluons (g), photon (γ),
450 W^\pm and Z bosons. Gluons and photon are massless, while the W^\pm , Z and H bosons are
451 massive. Each vector gauge boson serves as the mediator for a fundamental force described
452 by the SM. Gluons are massless particles mediating the strong interaction by carrying color
453 charges between quarks following quantum chromodynamics (QCD). Each gluon carries a
454 non-neutral color charge out of eight linearly independent color states in the gluon color
455 octet [49]. The photon ([citation](#)) is the massless and charge-neutral mediator particle for
456 the electromagnetic interaction following quantum electrodynamics (QED). The W^\pm and
457 Z bosons ([citation](#)) are massive mediator particles for the weak interaction, with the W^\pm
458 boson carrying an electric charge of ± 1 while the Z boson is charge neutral.

459 Other than the vector gauge boson, the only scalar boson in the SM is the massive and

460 charge neutral Higgs boson ([citation](#)). The Higgs boson does not mediate any fundamental
 461 force like vector bosons, but serve to provide the rest mass for all massive elementary particles
 462 in the SM through the Higgs mechanism described in section 2.1.2.3.

463 **Top quark**

464 As of now, the top quark (t) is the heaviest particle in the SM with mass of about 173 GeV
 465 [[50](#)], approaching the EW symmetry breaking scale. Its high mass gives the top quark the
 466 strongest Yukawa coupling to the Higgs boson ($y_t \approx 1$) [[24](#)] and exotic resonances in many
 467 proposed BSM models [[51–54](#)], making the top quark and its processes attractive vehicles
 468 with which to probe new physics.

469 Due to its mass, the top quark has a
 470 very short lifetime of 10^{-24} s [[22](#)] and de-
 471 cays before it can hadronize following color
 472 confinement. The top quark decays to a W
 473 boson and a b -quark with a branching ratio
 474 of almost 100%. The W boson can subse-
 475 quently decay to a quark-antiquark pair or
 476 to a lepton-neutrino pair (Figure 2.2), with
 477 branching ratios of approximately 68% and
 478 32% respectively. All lepton flavors have
 479 similar branching ratios during a leptonic W
 480 decay, assuming lepton universality.

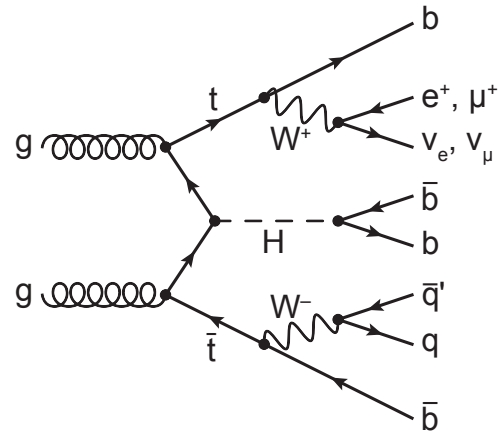


Figure 2.2: Feynman diagram for $t\bar{t}$ production and subsequent decay processes [[55](#)]. Top quark decays into a W -boson and b -quarks, and W -boson can decay to a $q\bar{q}$ or a $\ell\nu_\ell$ pair.

481 2.1.2 Mathematical formalism

482 The SM can be described within the formalism of quantum field theory (QFT) with the
483 Lagrangian [56]

$$\mathcal{L}_{\text{SM}} = \mathcal{L}_{\text{QCD}} + \underbrace{(\mathcal{L}_{\text{gauge}} + \mathcal{L}_{\text{fermion}} + \mathcal{L}_{\text{Higgs}} + \mathcal{L}_{\text{Yukawa}})}_{\mathcal{L}_{\text{EW}}} \quad (2.1)$$

484 where \mathcal{L}_{QCD} is the QCD term and \mathcal{L}_{EW} is the electroweak (EW) term of the Lagrangian.
485 Formalism of QFT within the SM treats particles as excitations [57] of their corresponding
486 quantum fields i.e. fermion field ψ , electroweak boson fields $W_{1,2,3}$ & B , gluon fields G_α and
487 Higgs field ϕ .

488 The foundation of modern QFT involves gauge theory. A quantum field has gauge sym-
489 metry if there exists a continuous gauge transformation that when applied to every point in
490 a field (local gauge transformation) leaves the field Lagrangian unchanged. The set of gauge
491 transformations of a gauge symmetry is the symmetry group of the field which comes with
492 a set of generators, each with a corresponding gauge field. Under QFT, the quanta of these
493 gauge fields are called gauge bosons.

494 The SM Lagrangian is gauge invariant under global Poincaré symmetry and local $SU(3)_C \times$
495 $SU(2)_L \times U(1)_Y$ gauge symmetry, with the $SU(3)_C$ symmetry group corresponding to the
496 strong interaction and $SU(2)_L \times U(1)_Y$ to the EW interaction. Global Poincaré symmetry
497 ensures that \mathcal{L}_{SM} satisfies translational symmetry, rotational symmetry and Lorentz boost
498 frame invariance [58]. These symmetries give rise to corresponding conservation laws, which
499 lead to conservation of momentum, angular momentum and energy in the SM as a result of
500 Noether's theorem [59].

501 **2.1.2.1 Quantum chromodynamics**

502 Quantum chromodynamics is a non-Abelian gauge theory i.e. Yang-Mills theory [6, 7]
 503 describing the strong interaction between quarks in the SM with the gauge group $SU(3)_C$,
 504 where C represents conservation of color charge under $SU(3)_C$ symmetry. According to
 505 QFT, quarks can be treated as excitations of the corresponding quark fields ψ . The free Dirac
 506 Lagrangian for the quark fields $\mathcal{L}_0 = \bar{\psi}(i\gamma^\mu\partial_\mu - m)\psi$ is invariant under global $SU(3)$ sym-
 507 metry, but not under local $SU(3)_C$ symmetry. To establish invariance under local $SU(3)_C$
 508 symmetry, the gauge covariant derivative D_μ is defined so that

$$D_\mu\psi = (\partial_\mu - ig_s G_\mu^a T_a)\psi, \quad (2.2)$$

509 where $g_s = \sqrt{4\pi\alpha_s}$ is the QCD coupling constant, $G_\mu^a(x)$ are the eight gluon fields, and
 510 T_a are generators of $SU(3)_C$, represented as $T_a = \lambda_a/2$ with λ_a being the eight Gell-Mann
 511 matrices [49]. Let the gluon field strength tensors $G_{\mu\nu}^a$ be

$$G_{\mu\nu}^a \equiv \partial_\mu G_\nu^a - \partial_\nu G_\mu^a - g_s f^{abc} G_\mu^b G_\nu^c, \quad (2.3)$$

512 where f^{abc} are the structure constants of $SU(3)_C$. The gauge invariant QCD Lagrangian
 513 can then be written as

$$\begin{aligned} \mathcal{L}_{\text{QCD}} &= \bar{\psi}(i\gamma^\mu D_\mu - m)\psi - \frac{1}{4}G_{\mu\nu}^a G_a^{\mu\nu} \\ &= \underbrace{-\frac{1}{4}G_{\mu\nu}^a G_a^{\mu\nu}}_{\text{gluon kinematics}} + \underbrace{\bar{\psi}(i\gamma^\mu\partial_\mu - m)\psi}_{\text{quark kinematics}} + \underbrace{\bar{\psi}^i(g_s\gamma^\mu(T_a)_{ij}G_\mu^a)\bar{\psi}^j}_{\text{quark-gluon interaction}} \end{aligned} \quad (2.4)$$

⁵¹⁴ where i, j are color indices with integer values from 1 to 3. Gluons are forced to be massless
⁵¹⁵ from the lack of a gluon mass term to maintain gauge invariance for the Lagrangian.

⁵¹⁶ **2.1.2.2 Electroweak theory**

⁵¹⁷ The electroweak interaction is the unified description of the weak interaction and electro-
⁵¹⁸ magnetism under the $SU(2)_L \times U(1)_Y$ symmetry group, where L represents the left-handed
⁵¹⁹ chirality of the weak interaction and Y represents the weak hypercharge quantum number.
⁵²⁰ Fermions can have either left-handed or right-handed chirality with the exception of neutr-
⁵²¹inos which can only have left-handed chirality in the SM, and can be divided into left-handed
⁵²² doublets and right-handed singlets

$$\psi_L = \begin{pmatrix} \nu_e \\ e_L \end{pmatrix}, \begin{pmatrix} \nu_\mu \\ \mu_L \end{pmatrix}, \begin{pmatrix} \nu_\tau \\ \tau_L \end{pmatrix}, \begin{pmatrix} u_L \\ d_L \end{pmatrix}, \begin{pmatrix} c_L \\ s_L \end{pmatrix}, \begin{pmatrix} t_L \\ b_L \end{pmatrix} \quad (2.5)$$

$$\psi_R = e_R, \mu_R, \tau_R, u_R, d_R, c_R, s_R, t_R, b_R.$$

⁵²³ where g' is the B_μ coupling constant and $B_\mu(x)$ is a vector gauge field that transforms under
⁵²⁴ $U(1)_Y$ as

$$B_\mu \rightarrow B_\mu + \frac{1}{g'} \partial_\mu \theta(x). \quad (2.6)$$

⁵²⁵ Right-handed fermion singlets are not affected by $SU(2)_L$ transformation, so the fermion
⁵²⁶ fields ψ transform under $SU(2)_L$ as

$$\psi_L \rightarrow e^{iI_3\vec{\theta}(x)\cdot\vec{\sigma}/2}\psi_L \quad (2.7)$$

$$\psi_R \rightarrow \psi_R.$$

⁵²⁷ where $\vec{\sigma}/2$ are generators of $SU(2)_L$ with $\vec{\sigma}$ being the Pauli matrices. In order to preserve
⁵²⁸ local symmetry, the gauge covariant derivative for $SU(2)_L$ and $U(1)_Y$ can be defined [60] so

⁵²⁹ that the gauge covariant derivative for $SU(2)_L \times U(1)_Y$ can be written as

$$\begin{aligned} D_\mu \psi_L &= \left(\partial_\mu - ig' \frac{Y_L}{2} B_\mu - ig \frac{\sigma_i}{2} W_\mu^i \right) \psi_L \\ D_\mu \psi_R &= \left(\partial_\mu - ig' \frac{Y_R}{2} B_\mu \right) \psi_R. \end{aligned} \quad (2.8)$$

⁵³⁰ where $B_\mu(x)$ is a vector gauge field associated with $U(1)_Y$ and $W_\mu^i(x)$ ($i = 1, 2, 3$) are three
⁵³¹ vector gauge fields associated with $SU(2)_L$. The B_μ and W_μ^i gauge fields transform under
⁵³² their corresponding symmetry groups $U(1)_Y$ and $SU(2)_L$ as

$$\begin{aligned} B_\mu &\rightarrow B_\mu + \frac{1}{g'} \partial_\mu \theta(x) \\ W_\mu^i &\rightarrow W_\mu^i + \frac{2}{g} \partial_\mu \theta_a(x) + \epsilon^{ijk} \theta_j(x) W_\mu^k, \end{aligned} \quad (2.9)$$

⁵³³ where g' is the B_μ gauge coupling constant, g is the W_μ^i gauge coupling constants and ϵ^{ijk}
⁵³⁴ is the $SU(2)_L$ structure constant. Similar to section 2.1.2.1, the kinetic term is added by
⁵³⁵ defining field strengths for the four gauge fields

$$\begin{aligned} B_{\mu\nu} &\equiv \partial_\mu B_\nu - \partial_\nu B_\mu \\ W_{\mu\nu}^i &\equiv \partial_\mu W_\nu^i - \partial_\nu W_\mu^i - g e^{ijk} W_\mu^j W_\nu^k. \end{aligned} \quad (2.10)$$

⁵³⁶ The local $SU(2)_L \times U(1)_Y$ invariant EW Lagrangian [60] is then

$$\begin{aligned} \mathcal{L}_{\text{EW}} &= i\bar{\psi}(\gamma^\mu D_\mu)\psi - \frac{1}{4}W_{\mu\nu}^i W_i^{\mu\nu} - \frac{1}{4}B_{\mu\nu} B^{\mu\nu} \\ &= \underbrace{i\bar{\psi}(\gamma^\mu \partial_\mu)\psi}_{\text{fermion kinematics}} - \underbrace{\bar{\psi}\left(\gamma^\mu g' \frac{Y}{2} B_\mu\right)\psi}_{\text{fermion-gauge boson interaction}} - \underbrace{\bar{\psi}_L\left(\gamma^\mu g \frac{\sigma_i}{2} W_\mu^i\right)\psi_L}_{\text{boson kinematics \& self-interaction}} - \underbrace{\frac{1}{4}W_{\mu\nu}^i W_i^{\mu\nu} - \frac{1}{4}B_{\mu\nu} B^{\mu\nu}}_{\text{boson kinematics \& self-interaction}}. \end{aligned} \quad (2.11)$$

537 Under ≈ 159.5 GeV, the EW symmetry $SU(2)_L \times U(1)_Y$ undergoes spontaneous symmetry
 538 breaking [61] into $U(1)_{\text{QED}}$ symmetry, which corresponds to a separation of the weak and
 539 electrodynamic forces. Electroweak spontaneous symmetry breaking replaces the four mass-
 540 less and similarly-behaved EW gauge bosons B_μ and W_μ^i with the EM boson γ and the weak
 541 bosons Z/W^\pm , as well as giving the Z and W^\pm bosons masses via the Higgs mechanism.
 542 This is due to a specific choice of gauge for the Higgs field leading to the reparameterization
 543 of the EW bosons B_μ and W_μ^i to $W^\pm/Z/\gamma$ using the relations

$$\begin{aligned}
 W_\mu^\pm &\equiv \frac{1}{\sqrt{2}} (W_\mu^1 \mp iW_\mu^2) \\
 \begin{pmatrix} A_\mu \\ Z_\mu \end{pmatrix} &\equiv \begin{pmatrix} \cos \theta_W & \sin \theta_W \\ -\sin \theta_W & \cos \theta_W \end{pmatrix} \begin{pmatrix} B_\mu \\ W_\mu^3 \end{pmatrix}
 \end{aligned} \tag{2.12}$$

544 where $\theta_W \equiv \cos^{-1} (g/\sqrt{g^2 + g'^2})$ is the weak mixing angle. The boson kinetic term can also
 545 be refactorized to extract cubic (three vertices) and quartic (four vertices) self-interactions
 546 among the gauge bosons [60]. The Lagrangian can then be rewritten as

$$\begin{aligned}
 \mathcal{L} = & \underbrace{eA_\mu \bar{\psi} (\gamma^\mu Q) \psi}_{\text{electromagnetism}} + \underbrace{\frac{e}{2 \sin \theta_W \cos \theta_W} \bar{\psi} \gamma^\mu (v_f - a_f \gamma_5) \psi Z_\mu}_{\text{neutral current interaction}} \\
 & + \underbrace{\frac{g}{2\sqrt{2}} \sum_{\psi_L} [\bar{f}_2 \gamma^\mu (1 - \gamma_5) f_1 W_\mu^+ + \bar{f}_1 \gamma^\mu (1 - \gamma_5) f_2 W_\mu^-]}_{\text{charged current interaction}} \\
 & + \underbrace{\mathcal{L}_{\text{kinetic}} + \mathcal{L}_{\text{cubic}} + \mathcal{L}_{\text{quartic}}}_{\text{boson self-interaction}}
 \end{aligned} \tag{2.13}$$

547 where $\gamma_5 = i\gamma^0\gamma^1\gamma^2\gamma^3$ is the chirality projection operator, $a_f = I_3$, $v_f = I_3(1 - 4|Q| \sin^2 \theta_W)$
 548 and f_1, f_2 are up and down type fermions of a left-handed doublet.

549 **2.1.2.3 Higgs mechanism**

550 So far, the EW bosons are massless since the mass terms $-m\bar{\psi}\psi$ for fermions and
 551 $-mA^\mu A_\mu$ for bosons are not invariant under the EW Lagrangian symmetries. The parti-
 552 cles must then acquire mass under another mechanism. The Brout-Engler-Higgs mechanism
 553 [11–13] was introduced in 1964 to rectify this issue and verified in 2012 with the discovery
 554 of the Higgs boson [20, 21].

555 The Higgs potential is expressed as

$$V(\phi^\dagger \phi) = \mu^2 \phi^\dagger \phi + \lambda (\phi^\dagger \phi)^2 \quad (2.14)$$

556 where μ^2 and $\lambda > 0$ are arbitrary parameters, and the $SU(2)_L$ doublet $\phi = \begin{pmatrix} \phi^+ \\ \phi^0 \end{pmatrix}$ is the Higgs
 557 field with complex scalar fields ϕ^+ and ϕ^0 carrying +1 and 0 electric charge respectively.

558 The Lagrangian for the scalar Higgs field is

$$\mathcal{L}_H = (\partial_\mu \phi)^\dagger (\partial^\mu \phi) - V(\phi^\dagger \phi). \quad (2.15)$$

559 Since the potential $V(\phi^\dagger \phi)$ is constrained by $\lambda > 0$, the ground state is solely controlled by
 560 μ . If $\mu^2 > 0$, the ground state energy is $\phi = 0$, and the EW bosons would remain massless.
 561 If $\mu^2 < 0$, the ground state is

$$|\phi|^2 = -\frac{\mu^2}{2\lambda} \equiv \frac{v^2}{\sqrt{2}}, \quad (2.16)$$

562 where v is defined as the vacuum expectation value (VEV). The standard ground state for
 563 the Higgs potential without loss of generality can be chosen as $\phi(0) = 1/\sqrt{2}(0)_v$.

564 Having $U(1)$ symmetry allows any $-e^{i\theta} \sqrt{\mu^2/\lambda}$ to be a ground state energy for the Higgs

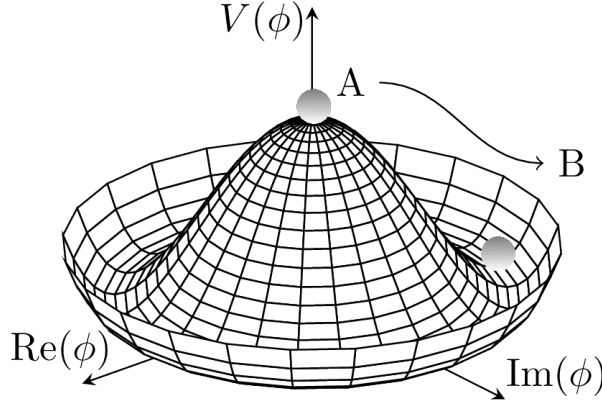


Figure 2.3: Illustration of a common representation of the Higgs potential [62]. Before SSB, the ground state $\phi(0)$ is located at A which is symmetric with respect to the potential. A perturbation to this state fixes the ground state energy $|\phi(0)|^2$ to a particular value at B, "spontaneously" breaking the symmetry and degeneracy in $|\phi(0)|^2$.

565 Lagrangian. This degeneracy results in spontaneous symmetry breaking of the $SU(2)_L \times$
 566 $U(1)_Y$ symmetry into $U(1)_{\text{EM}}$ symmetry when the Higgs field settles on a specific vacuum
 567 state as a result of a perturbation or excitation (Figure 2.3). The spontaneous symmetry
 568 breaking introduces three massless (Nambu-Goldstone [63]) vector gauge boson ξ and a
 569 massive scalar boson η , each corresponds to a generator of the gauge group. The vector field
 570 for ξ and η are real fields parameterized as $\xi \equiv \phi^+ \sqrt{2}$ and $\eta \equiv \phi^0 \sqrt{2} - v$ [64]. The Higgs
 571 field now becomes

$$\phi = \frac{v + \eta + i\xi}{\sqrt{2}} = \frac{1}{\sqrt{2}} e^{i\xi} \begin{pmatrix} 0 \\ v + \eta \end{pmatrix}. \quad (2.17)$$

572 Due to $U(1)_{\text{EM}}$ invariance, a unitary gauge with the transformation $\phi \rightarrow \exp(-i\xi \cdot) \frac{\sigma}{2v}$ can
 573 be chosen for the Higgs field to eliminate the massless bosons and incorporate them into the
 574 EM/weak bosons via Equation 2.12. This leaves the massive η which can now be observed as
 575 an excitation of the Higgs field from the standard ground state and must be the Higgs boson
 576 h . Using the EW covariant derivative from Equation 2.8, the Higgs Lagrangian around the

577 vacuum state becomes

$$\begin{aligned}\mathcal{L}_H &= (D_\mu \phi)^\dagger (D^\mu \phi) - \mu^2 \left(\frac{v+h}{\sqrt{2}} \right)^2 - \lambda \left(\frac{v+h}{\sqrt{2}} \right)^4 \\ &= (D_\mu \phi)^\dagger (D^\mu \phi) - \frac{1}{2} \mu^2 h^2 - \lambda v h^3 - \frac{\lambda}{4} h^4 - \dots\end{aligned}\tag{2.18}$$

578 The Higgs mass can be extracted from the quadratic term as $m_H = \sqrt{-2\mu^2}$. The kinetic

579 term in the Lagrangian can be written as

$$\begin{aligned}(D_\mu \phi)^\dagger (D^\mu \phi) &= \frac{1}{2} (\partial_\mu h)^2 + \frac{g^2}{8} (v+h)^2 \left| W_\mu^1 - i W_\mu^2 \right|^2 + \frac{1}{8} (v+h)^2 (g' W_\mu - g B_\mu) \\ &= \frac{1}{2} (\partial_\mu h)^2 + (v+h)^2 \left(\frac{g^2}{4} W_\mu^+ W^{-\mu} + \frac{1}{8} (g^2 + g'^2) Z_\mu^0 Z^{0\mu} \right).\end{aligned}\tag{2.19}$$

580 Masses for the EW bosons can be extracted from the quadratic terms

$$m_{W^\pm} = \frac{v}{2} g, \quad m_Z = \frac{v}{2} \sqrt{g^2 + g'^2}, \quad m_\gamma = 0.\tag{2.20}$$

581 However, the fermion mass term $-m\bar{\psi}\psi$ still breaks EW invariance after spontaneous symmetry breaking. Instead, fermions acquire mass by replacing the mass term with a gauge invariant Yukawa term in the EW Lagrangian representing fermions' interactions with the 583 Higgs field [64]

$$\begin{aligned}\mathcal{L}_{\text{Yukawa}} &= -c_f \frac{v+h}{\sqrt{2}} (\bar{\psi}_R \psi_L + \bar{\psi}_L \psi_R) \\ &= -\underbrace{\frac{c_f}{\sqrt{2}} v (\bar{\psi} \psi)}_{\text{fermion mass}} - \underbrace{\frac{c_f}{\sqrt{2}} (h \bar{\psi} \psi)}_{\text{fermion-Higgs interaction}},\end{aligned}\tag{2.21}$$

585 where c_f is the fermion-Higgs Yukawa coupling. The fermion mass is then $m_f = c_f v / \sqrt{2}$.

586 **2.2 Beyond the Standard Model**

587 **2.2.1 Top-philic vector resonance**

588 Many BSM models extend the SM by adding to the SM gauge group additional $U(1)'$
589 gauge symmetries [65, 66], each with an associated vector gauge boson nominally called Z' .
590 In the case of a BSM global symmetry group with rank larger than the SM gauge group, the
591 symmetry group can spontaneously break into $G_{\text{SM}} \times U(1)'^n$, where G_{SM} is the SM gauge
592 group $SU(3)_C \times SU(2)_L \times U(1)_Y$ and $U(1)'^n$ is any $n \geq 1$ number of $U(1)'$ symmetries. The
593 existence of additional vector bosons Z' would open up many avenues of new physics e.g.
594 extended Higgs sectors from $U(1)'$ symmetry breaking [67, 68], existence of flavor-changing
595 neutral current (FCNC) mediated by Z' [69], and possible exotic production from heavy Z'
596 decays [70].

597 Due to the top quark having the largest mass out of all known elementary particles in
598 the SM, many BSM models [38–43, 71, 72] predict ‘top-philic’ vector resonances that have
599 much stronger coupling to the top quark compared to other quarks. The analysis in this
600 dissertation attempts to reconstruct a top-philic Z' resonance directly to avoid dependency
601 on model choice. Previous model-independent BSM $t\bar{t}t\bar{t}$ search for top-philic resonances [28]
602 in the single-lepton final state and similar mass ranges set upper limits on observed (expected)
603 Z' production cross section between 21 (14) fb to 119 (86) fb depending on parameter choice.
604 This analysis is also motivated by the recent observation of SM $t\bar{t}t\bar{t}$ production in the same-
605 sign multilepton (SSML) channel by ATLAS [44] and CMS [73] at 6.1σ and 5.6σ discovery
606 significance respectively.

607 A simplified color-singlet vector particle model [45, 71] is employed to study model-

dependent interpretations. The interaction Lagrangian assumes only Z' to top coupling and has the form

$$\begin{aligned}\mathcal{L}_{Z'} &= \bar{t}\gamma_\mu (c_L P_L + c_R P_R) t Z'^\mu \\ &= c_t \bar{t}\gamma_\mu (\cos \theta P_L + \sin \theta P_R) t Z'^\mu,\end{aligned}\tag{2.22}$$

where $c_t = \sqrt{c_L^2 + c_R^2}$ is the Z' -top coupling strength, $P_{L/R} = (1 \mp \gamma_5)/2$ are the chirality projection operators, and $\theta = \tan^{-1}(c_R/c_L)$ is the chirality mixing angle. Expanding the Lagrangian results in

$$\mathcal{L}_{Z'} = \frac{1}{\sqrt{2}} \bar{t}\gamma_\mu \left[\sin \left(\theta + \frac{\pi}{4} \right) - \left(\sqrt{2} \cos \left(\theta + \frac{\pi}{4} \right) \right) \gamma_5 \right] t Z'^\mu,\tag{2.23}$$

which bears striking resemblance to the EW Lagrangian neutral current interaction term in Equation 2.13, showing the similarity between the Z' and the Z boson that acquires mass from $SU(2)_L \times U(1)_Y$ spontaneous symmetry breaking. Assuming the Z' mass $m_{Z'}$ is much larger than the top mass ($m_t^2/m_{Z'}^2 \approx 0$), the Z' decay width at leading-order (LO) can be approximated as

$$\Gamma(Z' \rightarrow t\bar{t}) \approx \frac{c_t^2 m_{Z'}}{8\pi}.\tag{2.24}$$

It can be observed that $\Gamma/m_{Z'} \approx c_t^2/8\pi \ll 1$ for $c_t \approx 1$, which suggests a very narrow and well-defined resonance peak. This validates the narrow-width approximation for the choice of $c_t = 1$ and supports efforts to directly reconstruct the resonance.

The main production channels for the aforementioned heavy topophilic color singlet Z' are at tree level and loop level, with the one-loop level being the dominant processes [45]. Loop level processes are dependent on the chirality angle θ , where $\theta = \pi/4$ suppresses all but gluon-initiated box sub-processes. To minimize model dependence, only the tree level

625 production was considered for this analysis by choosing $\theta = \pi/4$. Figure 2.4 illustrates
 626 several tree level Z' production processes.

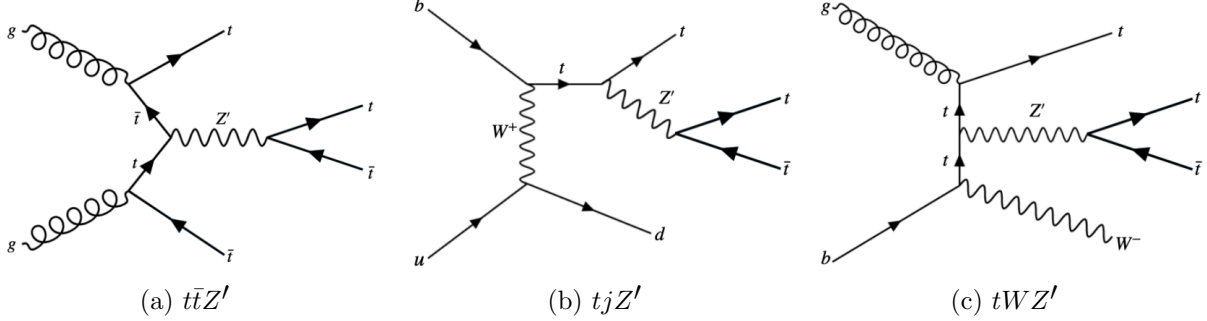


Figure 2.4: Feynman diagrams for tree level Z' production in association with (a) $t\bar{t}$, (b) tj (light quark) and (c) tW , decaying to final states containing (a) $t\bar{t}\bar{t}\bar{t}$ or (b)(c) $t\bar{t}t\bar{t}$ [45].

627 The single-top-associated channels tjZ' and tWZ' are suppressed by three-body phase
 628 space [45], resulting in smaller cross sections by a factor of two compared to the $t\bar{t}$ -associated
 629 process $t\bar{t}Z'$. Unlike tjZ' and tWZ' which are produced via EW and mixed QCD-EW
 630 interactions respectively, $t\bar{t}t\bar{t}$ production is governed by the strong interaction which can
 631 overpower phase space suppression. Additionally, $t\bar{t}t\bar{t}$ production is independent of θ while
 632 tjZ' and tWZ' are minimally suppressed under pure left-handed interactions ($\theta = 0$) and
 633 maximally suppressed under pure right-handed interactions ($\theta = \pi/2$).

634 2.2.2 BSM $t\bar{t}Z' \rightarrow t\bar{t}t\bar{t}$

635 This analysis uses the $t\bar{t}t\bar{t}$ final state signal signature to search for the existence of a heavy
 636 BSM resonance that couples strongly to the top quark. Cross section for $t\bar{t}t\bar{t}$ production
 637 can be enhanced by many possible BSM models, in particular production of heavy scalars
 638 and pseudoscalar bosons predicted in Type-II two-Higgs-doublet models (2HDM) [39–43] or
 639 possible production of a heavy neutral resonance boson $Z'(\rightarrow t\bar{t})$ in association with a $t\bar{t}$
 640 pair [74, 75]. The $t\bar{t}Z'$ production mode and consequently $t\bar{t}t\bar{t}$ signal signature can provide

- 641 a more sensitive channel for searches by avoiding contamination from the large SM $gg \rightarrow t\bar{t}$
 642 background in an inclusive $Z' \rightarrow t\bar{t}$ search.

643 2.2.3 Current exclusion limits

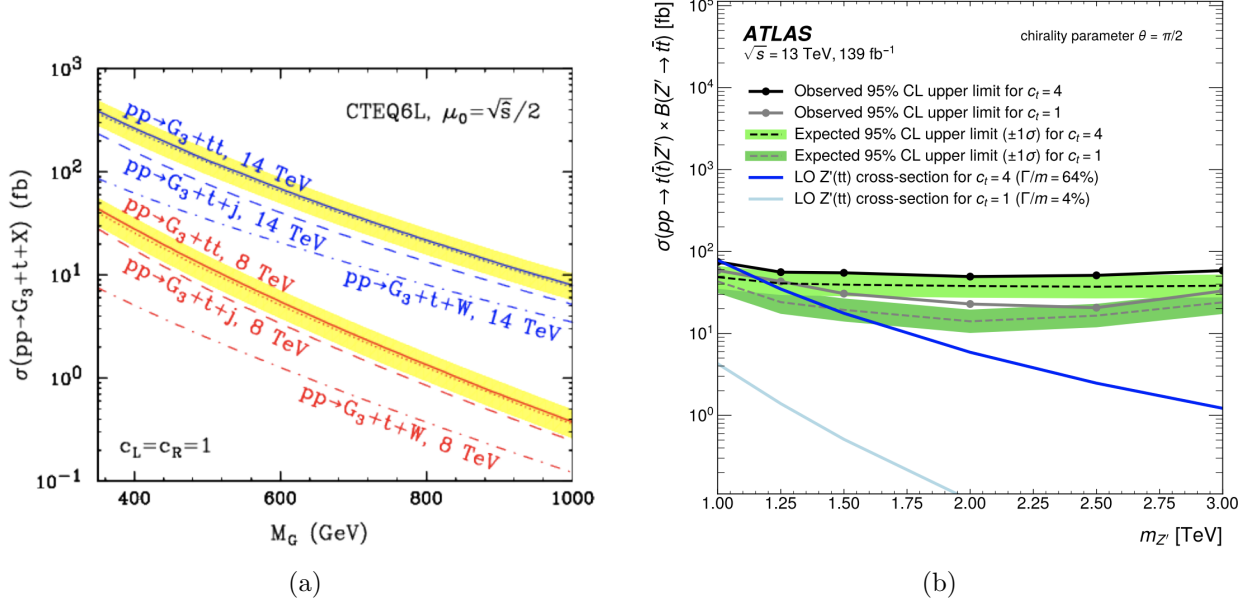
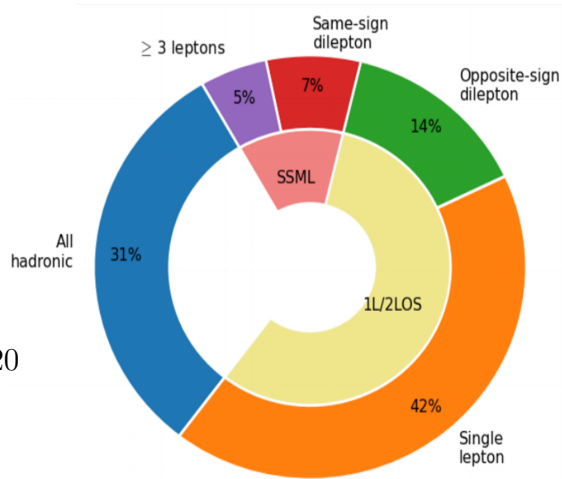


Figure 2.5: Tree level production cross-section. (a) G_3 is Z' . ttZ' solid, tjZ' dashed, tWZ' dot-dashed. Yellow bands = renormalization/factorization scale μ_0 variations of factor 2. Coupling $c_L = c_R = c_t/\sqrt{2}$ [45]. (b) ttZ' 1LOS search limits, theta=pi/2, green band = 68%, 139 fb^{-1} [28].

644 Decay modes

- 645 The different W boson decay modes
 646 shown in Figure 2.2 result in many differ-
 647 ent final states for $t\bar{t}Z'/t\bar{t}\bar{t}$ decay, which
 648 can each be classified into one of three chan-
 649 nels shown in Figure 2.6: all hadronic de-



650 cays; exactly one lepton or two opposite-sign
651 leptons (1LOS); exactly two same-sign lep-
652 tons or three or more leptons (SSML). The
653 branching ratio for each channel is shown
654 in Figure 2.6. The all hadronic and 1LOS
655 channels have much larger branching ratios
656 compared to SSML channel but suffer heavily from $gg \rightarrow t\bar{t}$ background contamination,
657 giving the SSML channel better sensitivity at the cost of lower statistics. This is also the
658 targeted channel for this analysis.

659 Chapter 3. LHC & ATLAS Experiment

660 3.1 The Large Hadron Collider

661 Predictions from theoretical models are evaluated against experimental data collected
662 from particle detectors. This chapter provides a detailed overview of the Large Hadron
663 Collider (LHC) and the ATLAS detector, one of the key experiments designed to study
664 high-energy collisions at the LHC.

665 3.1.1 Overview

666 The Large Hadron Collider [77] (LHC) is currently the world's largest particle collider
667 with a circumference of almost 27 km. Built by CERN on the border of Switzerland and
668 France, the LHC is designed as a particle collider for proton-proton (pp), sometimes heavy
669 ions i.e. lead-lead (PbPb) and proton-lead (pPb) beams at TeV-scale energies. Two beams
670 of particles are injected into the LHC in opposite directions and allowed to collide at the
671 center of four major experiments:

- 672 • **A Toroidal LHC ApparatuS** (ATLAS) [27] and **Compact Muon Solenoid** (CMS)
673 [78]: multi-purpose detectors, designed to target a variety of phenomena including SM,
674 BSM and heavy-ion physics.
- 675 • **Large Ion Collider Experiment** (ALICE) [79]: specialized detector to record ion
676 collisions and study heavy-ion physics.
- 677 • **Large Hadron Collider beauty** (LHCb) [80]: detector dedicated to study properties
678 of b -quarks and b -hadrons.

679 Aside from the four major experiments, the LHC also houses smaller experiments e.g.
 680 AWAKE [81], FASER [82], KATRIN [83], that either share an interaction point with one of
 681 the above experiments or make use of particle beams pre-LHC injection.

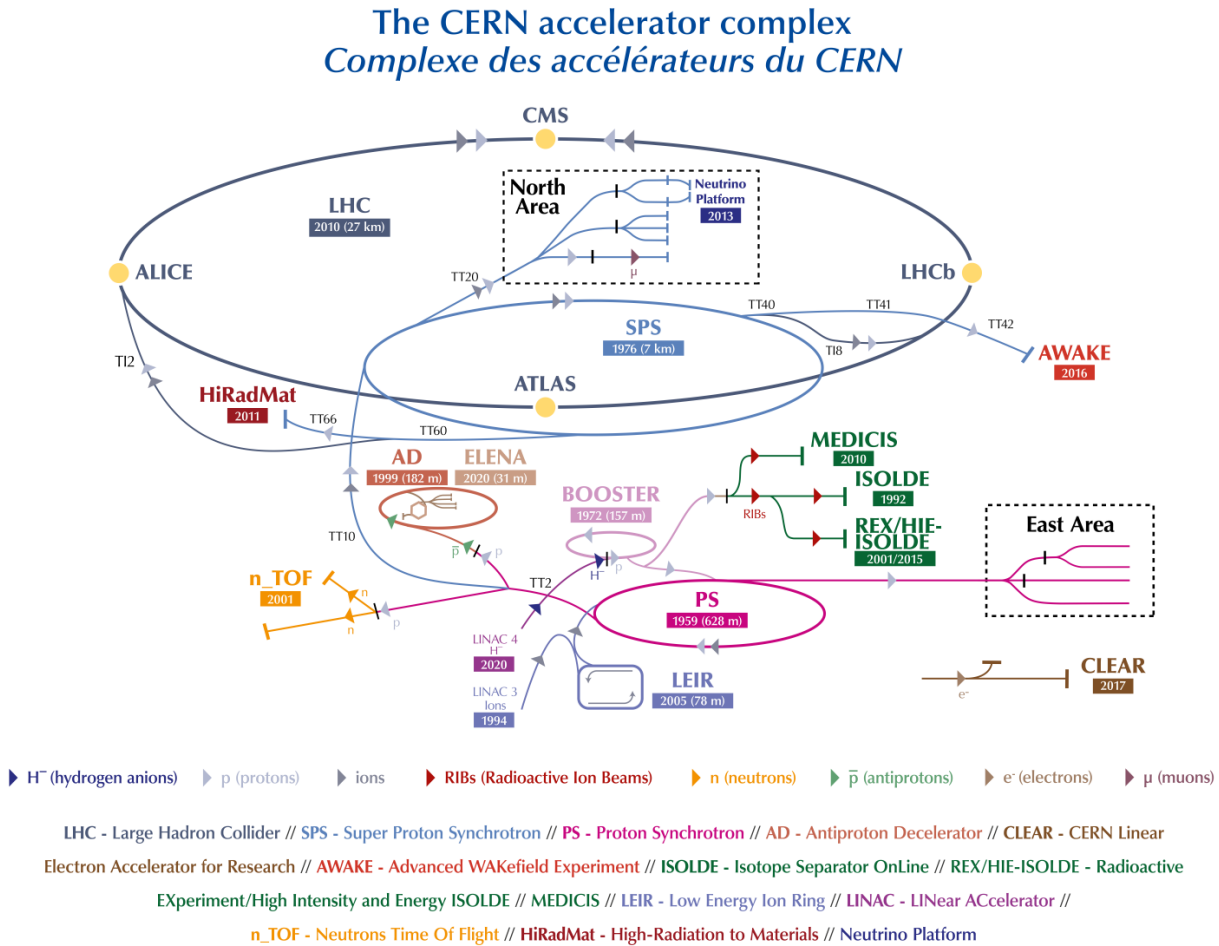


Figure 3.1: The full CERN accelerator complex as of 2022 [84].

682 The majority of the LHC operational time is dedicated to studying pp collisions of up to
 683 ~ 13 TeV center-of-mass energy, denoted as \sqrt{s} . Reaching collision energy requires a sequence
 684 of accelerators within the CERN accelerator complex, shown in Figure 3.1. Proton produc-
 685 tion starts at LINAC 4, where hydrogen atoms are accelerated to 160 MeV then stripped
 686 of electrons. The leftover proton beams are injected into the Proton Synchrotron Booster

687 (PSB) and accelerated to 2 GeV before being transferred into the Proton Synchrotron (PS).
 688 Here, the beams are ramped up to 26 GeV then injected into the Super Proton Synchrotron
 689 (SPS) to further raise the energy threshold to 450 GeV. The beams are finally injected into
 690 the LHC in opposite directions, continuously increasing in energy up to 6.5 TeV per beam,
 691 reaching the 13 TeV center-of-mass energy threshold necessary for collision during Run 2.
 692 As of the start of Run 3 in 2022, proton beams can now be ramped up to 6.8 TeV per beam
 693 for a total of $\sqrt{s} = 13.6$ TeV.

694 3.1.2 LHC operations

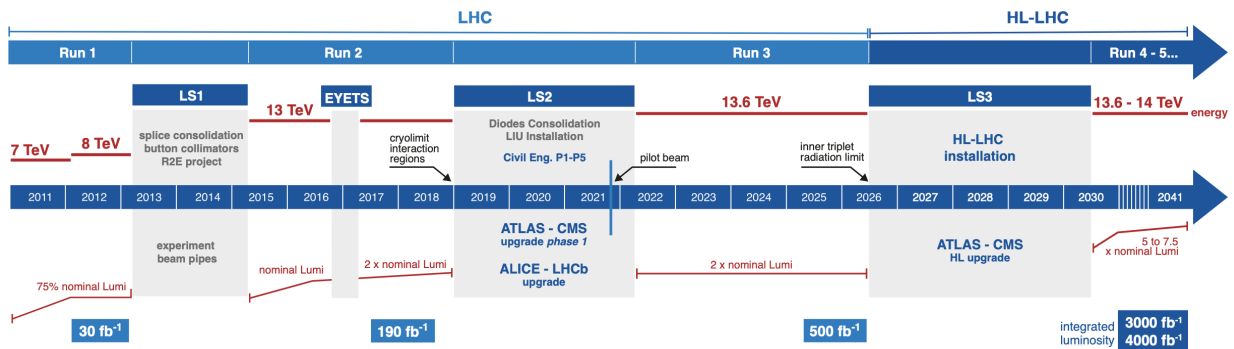


Figure 3.2: Current and future timeline of LHC operations with corresponding center-of-mass energies and projected integrated luminosities. [85].

695 Operations at the LHC are defined in periods of data-taking and shut-down known as
 696 runs and long shutdowns respectively; the first period (Run 1) started with first collisions
 697 at the LHC in 2010 at $\sqrt{s} = 7$ TeV [86]. Upgrades are usually carried out for detectors and
 698 accelerators during long shutdowns, raising the maximum energy threshold in preparation
 699 for the next run. An overview of the LHC runtime and corresponding center-of-mass energies
 700 are summarized in Figure 3.2. During Run 2 from 2015-2018, the ATLAS detector recorded
 701 a total of 1.1×10^{16} pp collisions at $\sqrt{s} = 13$ TeV, which corresponds to an integrated

702 luminosity of $140 \pm 0.83\% \text{ fb}^{-1}$ that passed data quality control and are usable for analyses
703 [87]. This is also the data set used for the analysis in this dissertation.

704 3.1.3 Physics at the LHC

705 The majority of physics studied at the LHC focus primarily on QCD proton-proton hard
706 scattering processes and the resulting products. Hard scattering processes involve large
707 momentum transfer compared to the proton mass e.g. top pair production ($gg \rightarrow t\bar{t}$) and
708 Higgs production ($gg \rightarrow H$), and can be predicted using perturbative QCD [88]. Hard
709 processes probe distance scales much lower than the proton radius and can be considered
710 collisions between the constituent quarks and gluons i.e. partons. Soft processes involve
711 lower momentum transfer between partons and are dominated by less well-understood non-
712 perturbative QCD effects. The hard interaction between two partons are represented by a
713 parton distribution function (PDF) $f_i(x, Q^2)$, which describes the probability of interacting
714 with a constituent parton i that carries a fraction x of the external hadron's momentum
715 when probed at a momentum scale of Q^2 [89]. Other partons within the hadron that did
716 not participate in the collision can still interact via lower momentum underlying-events
717 (UE). The probability of a particular interaction occurring is defined as its cross-section
718 $\sigma[b]$. Figure 3.3 gives an overview of SM processes produced within the LHC and their
719 cross-sections.

720 3.2 The ATLAS detector

721 One of the four main experiments at the LHC is ATLAS [27], designed as a multi-purpose
722 detector for the role of studying high-energy physics in pp and heavy-ion collisions. ATLAS

Standard Model Production Cross Section Measurements

Status: October 2023

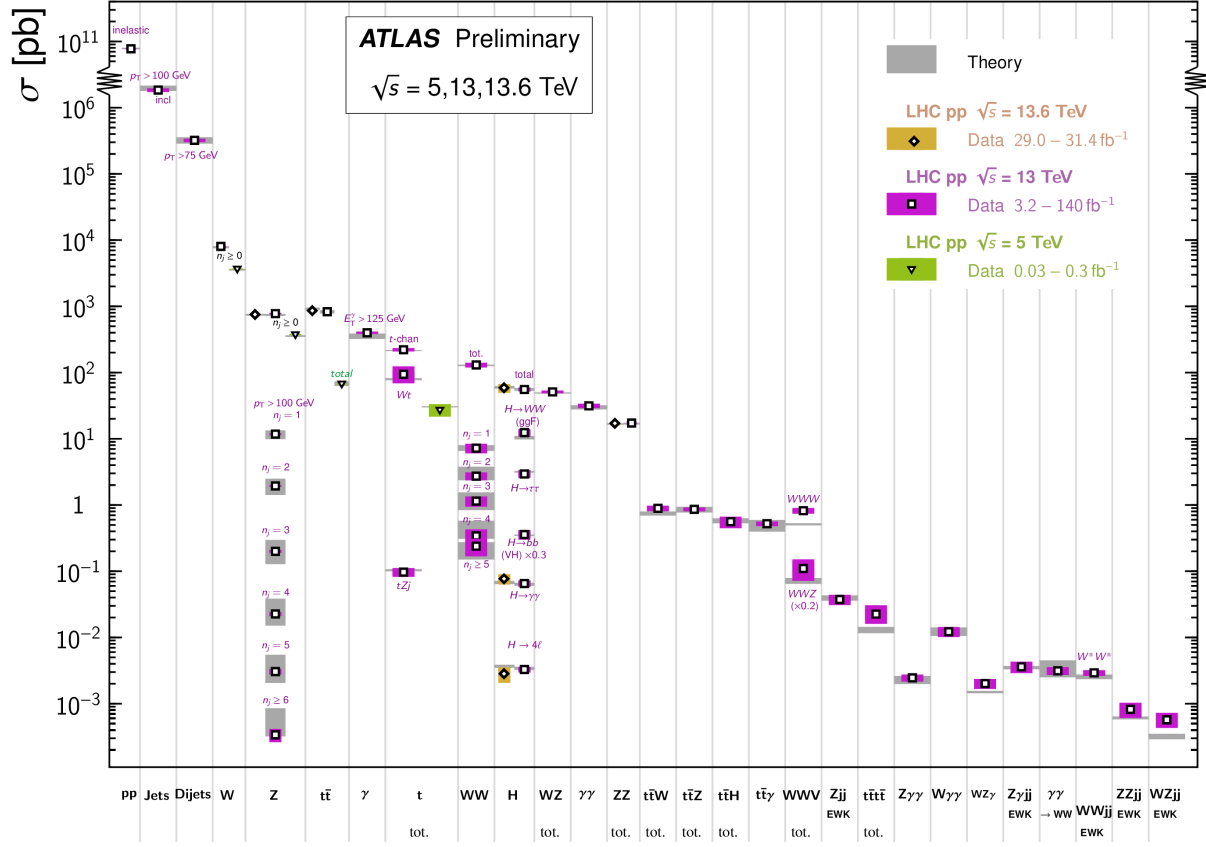


Figure 3.3: Summary of predicted and measured cross-section for SM processes at the LHC at different center-of-mass energies [90].

723 is a detector with symmetric cylindrical geometry with dimensions of 44 m in length and 25
 724 m in diameter, covering a solid angle of almost 4π around the collision point. The detector is
 725 built concentrically around the beamline with the collision point at the center to maximally
 726 capture signals produced by interactions. Figure 3.4 shows a slice of the ATLAS detector.
 727 From the inside out, the main ATLAS subdetector system consists of the inner detector
 728 (ID), calorimeter systems (electromagnetic and hadronic) and the muon spectrometer (MS).
 729 The ATLAS detector uses a right-handed coordinate system [27] designed to align with
 730 the geometry of a collision interaction, with the origin set at the interaction point, the z -axis

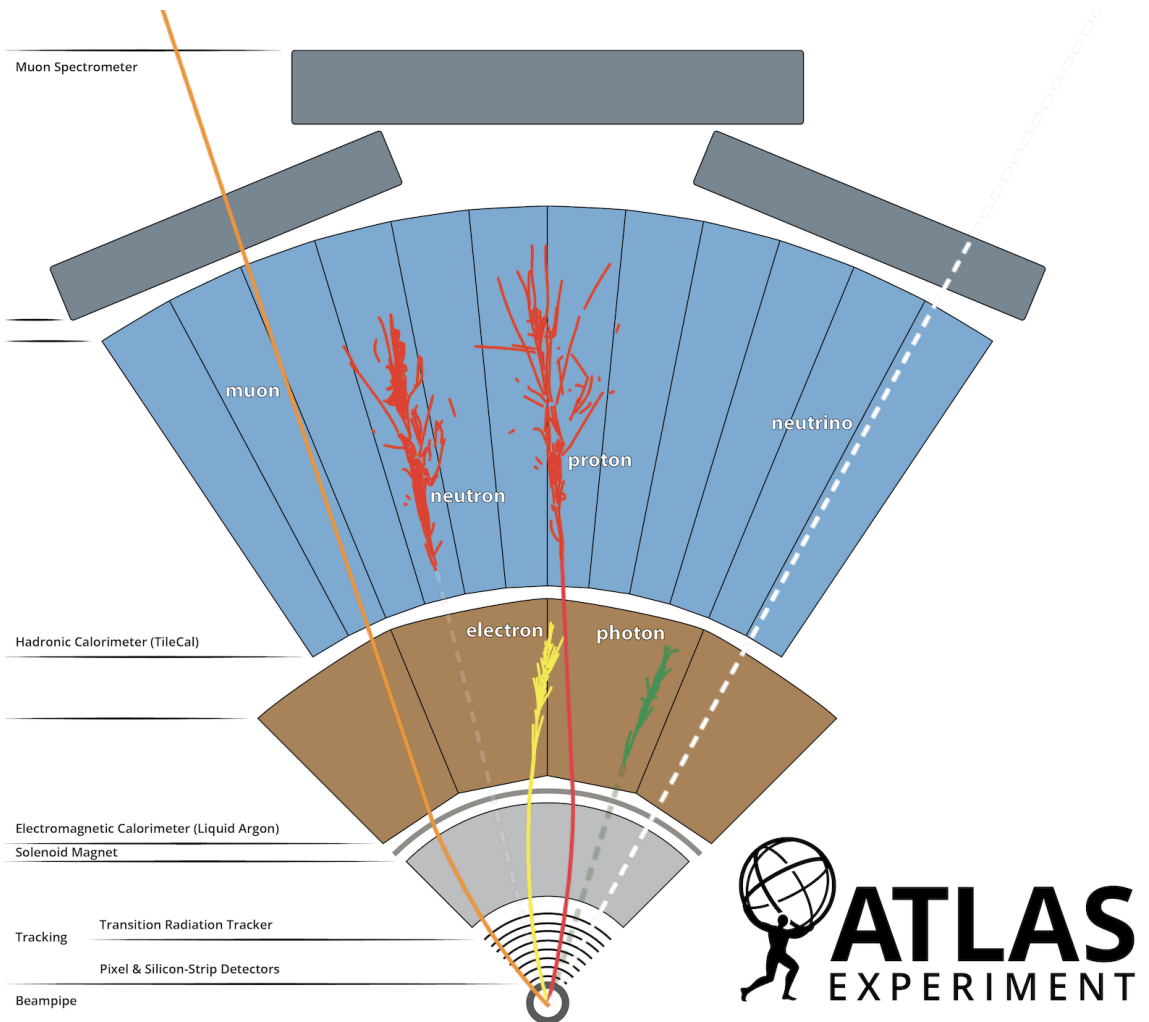


Figure 3.4: A cross section slice of the ATLAS detector showing different subsystems along with visualization of different types of particles traveling through the detector [91].

731 following (either of) the beamline and the x -axis pointing towards the center of the LHC
 732 ring. In cylindrical coordinates, the polar angle θ is measured from the beam axis, and
 733 the azimuthal angle ϕ is measured along the transverse plane (xy -plane) starting at the x -
 734 axis. Additional observables are defined for physics purposes: the pseudorapidity defined as
 735 $\eta = -\ln \tan(\theta/2)$; angular distance within the detector defined as $\Delta R = \sqrt{\Delta\eta^2 + \Delta\phi^2}$; and
 736 transverse momentum p_T (transverse energy E_T) defined as the component of the particle's
 737 momentum (energy) projected onto the transverse plane.

738 3.2.1 Inner detector

739 The innermost part of ATLAS is the inner detector (ID) [27], constructed primarily for
740 the purpose of measuring and reconstructing charged tracks within the $|\eta| < 2.5$ region with
741 high momentum resolution ($\sigma_{p_T}/p_T = 0.05\% \pm 1\%$). Figure 3.5 shows the composition of
742 the ID with three subsystems, the innermost being the pixel detector, then Semiconductor
743 Tracker (SCT), and the Transition Radiation Tracker (TRT) on the outermost layer; all of
744 which are surrounded by a solenoid magnet providing a magnetic field of 2 T.

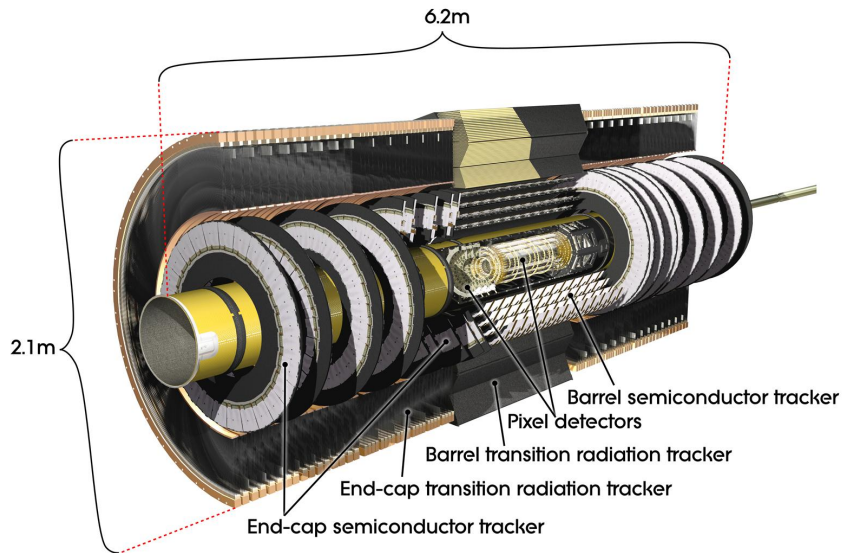


Figure 3.5: Cutaway illustration of the inner detector along with its subsystems [92].

745 Pixel detector

746 The pixel detector subsystem [27] consists of 250 μm silicon semiconductor pixel layers
747 with about 80.4 million readout channels, reaching a spatial resolution of 10 μm in the
748 $R - \phi$ (transverse) plane and 115 μm in the z -direction for charged tracks. Charged particles
749 passing through the pixel detector ionize the silicon layers and produce electron-hole pairs;

750 the electrons drift towards the detector's electrode under an applied electric field and the
751 resulting electric signals are collected in read-out regions. The pixel detector is used primarily
752 for impact parameter measurement, pile-up suppression, vertex finding and seeding for track
753 reconstruction.

754 Semiconductor Tracker

755 The Semiconductor Tracker (SCT) [27] functions similarly to the pixel detector, using
756 silicon semiconductor microstrips totaling about 6.3 million read-out channels, reaching a
757 per layer resolution of 17 μm in the $R\text{-}\phi$ plane and 580 μm in the z -direction [27]. The
758 SCT plays an important role in precise p_{T} measurement of charged particles as well as track
759 reconstruction.

760 Transition Radiation Tracker

761 The outermost layer of the ID, the Transition Radiation Tracker (TRT) [27], consists of
762 layers of 4 mm diameter straw tubes filled with a xenon-based gas mixture and a 30 μm
763 gold-plated wire in the center. The TRT contains a total of about 351 thousand readout
764 channels with a resolution of 130 μm for each straw tube in the $R\text{-}\phi$ plane, and provides
765 extended track measurement, particularly estimation of track curvature under the solenoidal
766 magnetic field. Importantly, the TRT also serves to identify electrons through absorption of
767 emitted transition-radiation within the Xe-based gas mixture.

768 3.2.2 Calorimeter systems

769 Surrounding the ID is the ATLAS calorimeter system [27] with electromagnetic (EM) and
770 hadronic calorimeters, covering a range of $|\eta| < 4.9$. The calorimeters are sampling calorime-

771 ters with alternating absorbing layers to stop incoming particles and active layers to collect
 772 read-out signals from energy deposits. Incoming particles passing through the calorimeters
 773 interact with the absorbing layers, producing EM or hadronic showers of secondary particles.
 774 The particle showers deposit energy in the corresponding layer of the calorimeters, which
 775 are collected and aggregated to identify and reconstruct the original particle's energy and
 776 direction. Figure 3.6 shows a schematic overview of the ATLAS calorimeter system.

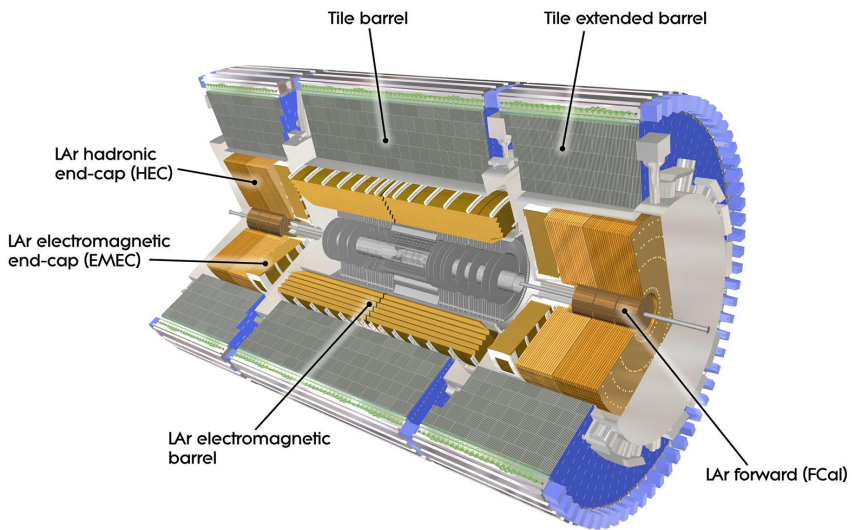


Figure 3.6: Cutaway illustration of the calorimeter system including the EM, hadronic and LAr forward calorimeters [93].

777 Electromagnetic calorimeter

778 The EM calorimeter [27] covers the innermost part of the calorimeter system, with lead
 779 (Pb) absorbing layers and liquid argon (LAr) active layers to capture the majority of electrons
 780 and photons exiting the ID. The EM calorimeter is divided into regions depending on η
 781 coverage: a barrel region ($|\eta| < 1.475$), two endcap regions ($1.375 < |\eta| < 3.2$) and a
 782 transition region ($1.372 < |\eta| < 1.52$). The endcap calorimeters are further divided into an

783 outer wheel region ($1.372 < |\eta| < 2.5$) and an inner wheel region ($2.5 < |\eta| < 3.2$) in order
784 to provide precise coverage within the same η range as the ID. Overlap between the barrel
785 and endcap regions compensates for the lower material density in the transition region.

786 **Hadronic calorimeter**

787 The hadronic calorimeter [27] covers up to $|\eta| < 4.9$ and is comprised of three parts: the
788 tile calorimeter with a barrel region ($|\eta| < 1.0$) and extended barrel regions ($0.8 < |\eta| < 1.7$);
789 the hadronic endcap calorimeter (HEC) covering $1.5 < |\eta| < 3.2$; and the forward calorimeter
790 (FCal) covering $3.2 < |\eta| < 4.9$. The tile calorimeter covers the EM calorimeter barrel region
791 and uses steel as material for the absorbing layers with scintillating tiles for the active layers.
792 Signals captured by scintillating tiles are read out from both sides using photomultiplier
793 tubes. The HEC calorimeter covers the endcap regions of the EM calorimeter and uses a
794 copper-LAr calorimeter layer scheme. The FCal is located close to the beamline providing
795 coverage for particles traveling close to parallel with the beam axis. The subdetector contains
796 three modules: one with copper absorbing layers optimized for EM measurements, and two
797 with tungsten absorbing layers targeting hadronic cascades. All modules in the FCal use
798 LAr as the active layer.

799 **3.2.3 Muon spectrometer**

800 Generally, the only particles that penetrate past the calorimeter layer are muons and
801 neutrinos. The muon spectrometer (MS) [27] is situated on the outermost of the ATLAS
802 detector and aims to track and measure muons within $|\eta| < 2.7$. The MS utilizes an array of
803 toroid magnets to provide a magnetic field perpendicular to the muon trajectory, bending
804 the track in order to measure its curvature. The magnetic field is powered by a large barrel

805 toroid ($|\eta| < 1.4$) with strength of 0.5 T and two endcap toroid magnets ($1.6 < |\eta| < 2.7$) of
806 1 T. Both types contribute to the magnetic field in the transition region ($1.4 < |\eta| < 1.6$).

807 To measure the muon itself, four types of large gas-filled chambers known as muon cham-
808 bers [27] are designed and constructed for two main goals: triggering on potential muon
809 candidates entering the MS and tracking their trajectories through the detector with high
810 precision. The tracking system include Monitored Drift Tubes (MDTs), which record muon
811 track information over the entire MS η range ($|\eta| < 2.7$). The MDTs are built with multi-
812 ple layers of drift tubes and filled with a mixture of 93% Ar and 7% CO₂. Muons passing
813 through drift tubes in the MDT ionize the gas within each tube; signals are then recorded
814 as freed electrons drift to read-out channels under an applied electric field. In the forward
815 region ($2.0 < |\eta| < 2.7$), Cathode Strip Chambers (CSCs) are included along with MDTs.
816 The CSCs are multiwire proportional chambers built with higher granularity and shorter
817 drift time than the MDTs to handle tracking in an environment with high background rates
818 .

819 The MS trigger system includes Resistive Plate Chambers (RPCs) [27], which provide
820 triggering in the barrel region ($|\eta| < 1.05$) using parallel electrode plates made of resistive
821 materials with a gas mixture inbetween. High voltage is applied to the plates, accelerat-
822 ing the electrons freed from ionized gas and creating a fast avalanche of charge, which is
823 collected on external read-out strips almost instantaneously. Triggering and coarse position
824 measurements in the endcap region ($1.05 < |\eta| < 2.5$) is handled by Thin-Gap Chambers
825 (TGCs). Similar to CSCs, TGCs are multiwire proportional chambers with a small wire gap
826 ("thin-gap") and high applied voltage across the gap, resulting in fast response time giving
827 TGCs the capabilities to identify muon candidates in real time.

828 **3.2.4 Trigger & data acquisition**

829 The LHC produces a colossal amount of collision data at a bunch crossing rate of 40 MHz
830 with bunch spacing of 25 ns. The ATLAS Trigger and Data Acquisition (TDAQ) system [94]
831 synchronously identifies and records interesting events for in-depth analysis. The ATLAS
832 trigger system in Run 2 consists of two steps: Level-1 (L1) trigger and High-Level Trigger
833 (HLT). Events failing any step in the trigger chain are permanently lost.

834 The L1 trigger hardware is divided into L1 calorimeter triggers (L1Calo) and L1 muon
835 triggers (L1Muon) [94]. L1Calo trigger uses information from ATLAS calorimeter system
836 to quickly identify signs of high p_T objects e.g. EM clusters, jets and missing transverse
837 energy E_T^{miss} (section 4.4). Similarly, L1Muon uses information from the RPCs and TGCs
838 of the MS to make quick decisions on potentially interesting muon candidates. Outputs
839 from L1Calo and L1Muon are fed into the L1 topological trigger (L1Topo) for additional
840 filtering based on event topology and multi-object correlation, allowing for more selective
841 and physics-motivated triggering. Decisions from all three types of L1 triggers are provided
842 as inputs for the Central Trigger Processor (CTP) for a final Level-1 Accept (L1A) decision.

843 The entire L1 trigger chain results in a 2.5 μs latency and reduces the event rate to 100 kHz.

844 Events passing L1 triggers are sent to HLTs before being saved to offline storage at
845 CERN data centers. HLTs are software-based triggers used for more complex and specific
846 selections on physics objects required by targeted analysis goals, in turn requiring more
847 computing power with longer latency. After HLT selections, the event rate is reduced to 1
848 kHz on average [94]. Overall, the full trigger chain reduces the event rate for ATLAS by
849 approximately a factor of 4×10^4 .

850 Chapter 4. Particle Reconstruction & Identifi- 851 fication

852 Activity within the ATLAS detector is recorded as raw electronic signals, which can
853 be utilized by ATLAS reconstruction software to derive physics objects for analysis. This
854 chapter describes the reconstruction and identification of basic objects (e.g. interaction
855 vertices, tracks, topological clusters of energy deposits) and subsequently of complex physics
856 objects i.e. particles and particle signatures.

857 4.1 Primary reconstruction

858 4.1.1 Tracks

859 Charged particles traveling through the ATLAS detector deposit energy in different layers
860 of the ID and MS. The ID track reconstruction software consists of two algorithm chains:
861 inside-out and outside-in track reconstruction [95–97].

862 The inside-out algorithm is primarily used for the reconstruction of primary particles
863 i.e. particles directly produced from pp collisions or decay products of short-lived particles.

864 The process starts by forming space points from seeded hits in the silicon detectors within
865 the pixel & SCT detectors. Hits further away from the interaction vertex are added to
866 the track candidate using a combinatorial Kalman filter [98] pattern recognition algorithm.

867 Track candidates are then fitted with a χ^2 filter [99] and loosely matched to a fixed-sized
868 EM cluster. Successfully matched track candidates are re-fitted with a Gaussian-sum filter
869 (GSF) [100], followed by a track scoring strategy to resolve fake tracks & hit ambiguity

870 between different tracks [101]. The track candidate is then extended to the TRT to form
871 final tracks satisfying $p_T > 400$ MeV. The outside-in algorithm handles secondary tracks
872 mainly produced from long-lives particles or decays of primary particles by back-tracking
873 from TRT segments, which are then extended inward to match silicon hits in the pixel and
874 SCT detectors to form track reconstruction objects.

875 4.1.2 Vertices

876 Vertices represent the point of interaction or decay for particles within the ATLAS de-
877 tector. Primary vertices (PVs) are defined as the point of collision for hard-scattering pp
878 interactions, while secondary or displaced vertices result from particle decays occurring at a
879 distance from its production point.

880 Reconstruction of PVs is crucial to accurately profile the kinematic information of an
881 event and form a basis for subsequent reconstruction procedures. Primary vertex recon-
882 struction occurs in two stages: vertex finding and vertex fitting [102]. The vertex finding
883 algorithm uses the spatial coordinates of reconstructed tracks to form the seed for a vertex
884 candidate. An adaptive vertex fitting algorithm [103] then iteratively evaluates track-vertex
885 compatibility to estimate a new best vertex position. Less compatible tracks are down-
886 weighted in each subsequent iteration, and incompatible tracks are removed and can be
887 used for another vertex seed; the process is repeated until no further PV can be found.
888 All reconstructed vertices without at least two matched tracks are considered invalid and
889 discarded.

890 Secondary vertex reconstruction uses the Secondary Vertex Finder (SVF) algorithm [104]
891 which is primarily designed to reconstruct b - and c -hadrons for flavor tagging purposes. The
892 SVF aims to reconstruct one secondary vertex per jet and only considers tracks that are

893 matched to a two-track vertex and contained within a p_T -dependent cone around the jet
894 axis. The tracks are then used to reconstruct a secondary vertex candidate using an iterative
895 process similar to the PV vertex fitting procedure.

896 **Pile-up**

897 At high luminosities, multiple interactions can be associated with one bunch crossing,
898 resulting in many PVs. The effect is called pile-up [105], and usually result from soft QCD
899 interactions. Pile-up can be categorized into two types: in-time pile-up, stemming from
900 additional pp collisions in the same bunch crossing that is not the hard-scatter process; out-
901 of-time pile-up, resulting from leftover energy deposits in the calorimeters from other bunch
902 crossings.

903 **4.1.3 Topological clusters**

904 Topological clusters (topo-clusters) [106] consist of clusters of spatially related calorimeter
905 cell signals. Topo-clusters are primarily used to reconstruct hadron- and jet-related objects
906 in an effort to extract signal while minimizing electronic effects and physical fluctuations, and
907 also allow for recovery of energy lost through bremsstrahlung or photon conversions. Cells
908 with signal-to-noise ratio $\zeta_{\text{cell}}^{\text{EM}}$ passing a primary seed threshold are seeded into a dynamic
909 topological cell clustering algorithm as part of a proto-cluster. Neighboring cells satisfying a
910 cluster growth threshold are collected into the proto-cluster. If a cell is matched to two proto-
911 clusters, the clusters are merged. Two or more local signal maxima in a cluster satisfying
912 $E_{\text{cell}}^{\text{EM}} > 500 \text{ MeV}$ suggest the presence of multiple particles in close proximity, and the cluster
913 is split accordingly to maintain good resolution of the energy flow. The process continues
914 iteratively until all cells with $\zeta_{\text{cell}}^{\text{EM}}$ above a principal cell filter level have been matched to a

915 cluster.

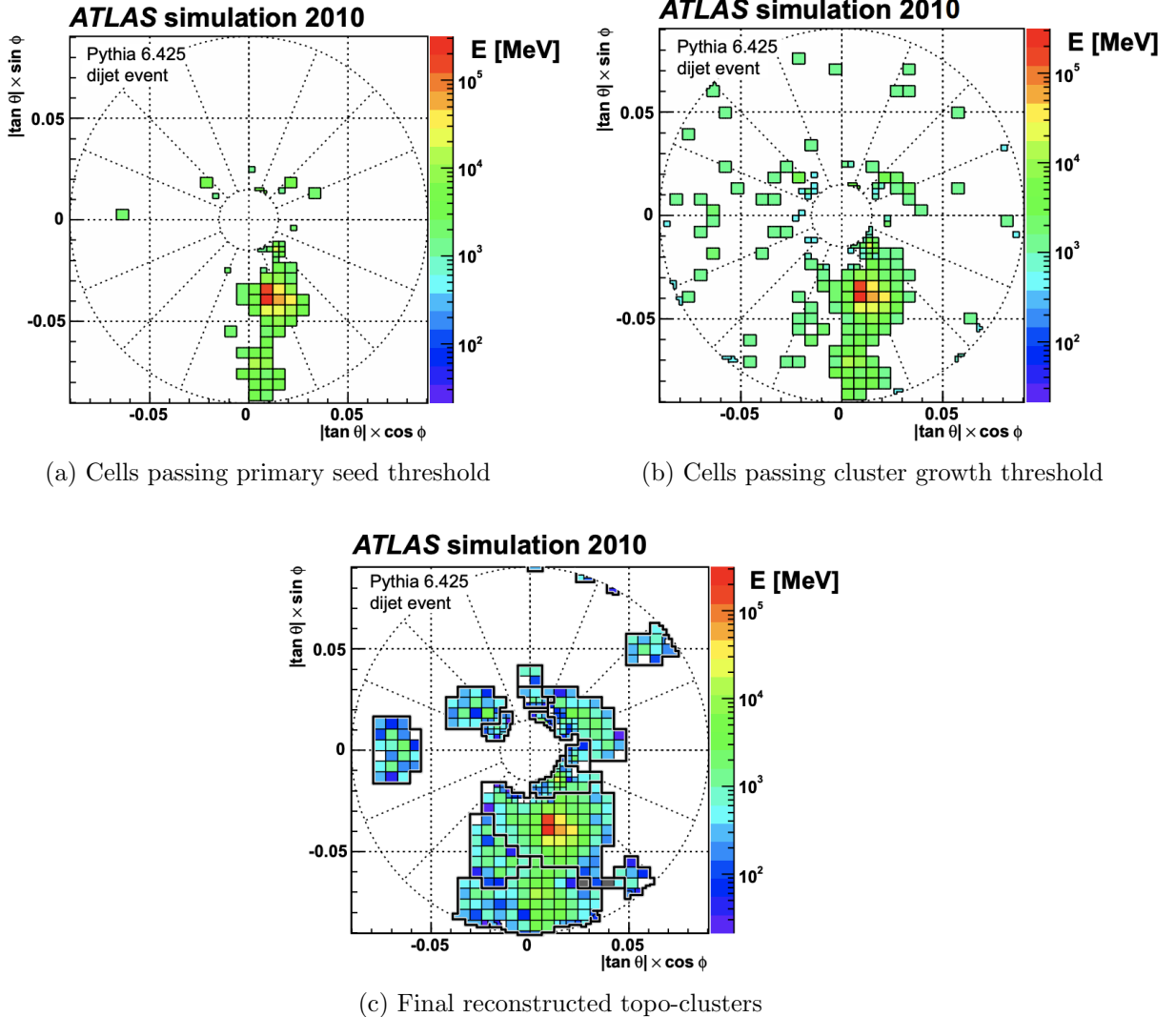


Figure 4.1: Stages of topo-cluster formation corresponding to each threshold. In (a), proto-clusters are seeded from cells with adequate signal significance $\zeta_{\text{cell}}^{\text{EM}}$. The clusters are further merged and split in (b) following a predefined cluster growth threshold. The process stops in (c) when all sufficiently significant signal hits have been matched to a cluster [106].

916 4.2 Jets

917 Quarks, gluons and other hadrons with non-neutral color charge cannot be observed
 918 individually due to QCD color confinement, which forces a non-color-neutral hadron to

almost immediately undergo hadronization, producing a collimated cone of color-neutral hadrons defined as a jet. Jet signals can be used to reconstruct and indirectly observe the quarks or gluons from which the jet originated in the original hard-scattering process.

4.2.1 Jet reconstruction

The ATLAS jet reconstruction pipeline is largely carried out using a particle flow (PFlow) algorithm combined with an anti- k_t jet clustering algorithm. The PFlow algorithm [107] utilizes topo-clusters along with information from both the calorimeter systems and the ID in order to make use of the tracker system’s advantages in low-energy momentum resolution and angular resolution. First, the energy from charged particles is removed from the calorimeter topo-clusters; then, it is replaced by particle objects created using the remaining energy in the calorimeter and tracks matched to topo-clusters. The ensemble of ”particle flow objects” and corresponding matched tracks are used as inputs for the iterative anti- k_t algorithm [108].

The main components of the anti- k_t algorithm involve the distance d_{ij} between two jet candidates i and j , and the distance d_{iB} between the harder jet candidate of the two (defined as i) and the beamline B . If $d_{ij} < d_{iB}$, then the two jet candidates are combined and returned to the pool of candidates; otherwise, jet candidate i is considered a jet and removed from the pool. The distance d_{ij} is inversely proportional to a predefined radius parameter ΔR in order to control reconstruction quality for small- R and large- R jets. This analysis uses $\Delta R = 0.4$ to better handle heavily collimated small- R jets resulting from parton showers.

The anti- k_t jets so far have only been reconstructed at the EM level and need to be calibrated to match the energy scale of jets reconstructed at particle level. This is done via a MC-based jet energy scale (JES) calibration sequence, along with further calibrations

942 to account for pile-up effects and energy leakage. The full JES calibration sequence is
 943 shown in Figure 4.2. All calibrations except origin correction are applied to the jet's four-
 944 momentum i.e. jet p_T , energy and mass. Afterwards, a jet energy resolution (JER) [109]
 945 calibration step is carried out in a similar manner to JES to match the resolution of jets in
 946 dijet events. To further suppress pile-up effects, a neural-network based jet vertex tagger
 947 (NNJvt) discriminant was developed based on the previous jet vertex tagger (JVT) algorithm
 948 [105] and applied to low- p_T reconstructed jets.

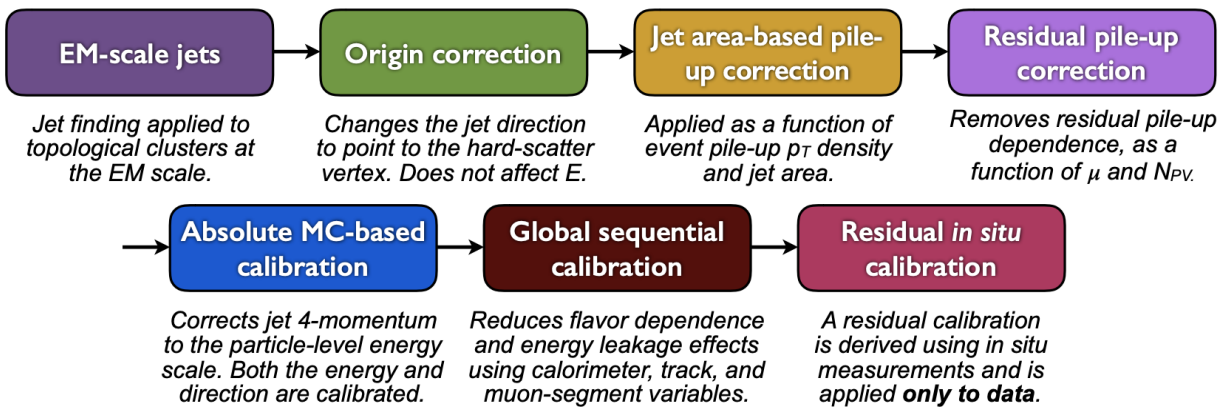


Figure 4.2: Jet energy scale calibration sequence for EM-scale jets [110].

949 4.2.2 Flavor tagging

950 Identifying and classifying hadronic jets are important tasks for ATLAS physics, for
 951 example analyses involving Higgs decays $H \rightarrow b\bar{b}$ or top quarks. Flavor tagging or b -tagging
 952 is the process of identifying jets containing b -hadrons, c -hadrons, light-hadrons (uds -hadrons)
 953 or jets from hadronically decaying τ leptons. Distinguishing b -jets is possible due to their
 954 characteristically long lifetime ($\tau \approx 1.5$ ps), displaced secondary decay vertex and high decay
 955 multiplicity.

956 Usage of b -tagging in this analysis is done via five operating points (OPs), corresponding

957 to 65%, 70%, 77%, 85% and 90% b -jet tagging efficiency ε_b in simulated $t\bar{t}$ events, in order
958 from the tightest to loosest discriminant cut point. The OPs are defined by placing selections
959 on the tagger output to provide a predefined ε_b level; the selection cuts act as a variable
960 trade-off between b -tagging efficiency and b -jet purity i.e. c - or light-jet rejection. For this
961 analysis, a jet is considered b -tagged if it passes the 85% OP. The b -tagged jet is then
962 assigned a pseudo-continuous b -tagging (PCBT) score, which quantifies a jet's ability to
963 satisfy different OPs. The score can take integer values between 1 and 6, where a score of 6
964 is assigned to jets passing all OP thresholds; a score of 2 for jets that pass only the tightest
965 OP (90%); and a score of 1 for jets that pass no OP. A value of -1 is also defined for any jet
966 that does not satisfy b -tagging criteria. Since the targeted $t\bar{t}t\bar{t}$ final states contain at least
967 four b -hadrons from top and W decays, a b -tagging OP of 85% is used to maintain high
968 purity during b -tagged jet selections in the signal region.

969 **GN2 b -tagging algorithm**

970 For this analysis, b -jets are identified and tagged with the GN2v01 b -tagger [111]. The
971 GN2 algorithm uses a Transformer-based model [112] modified to incorporate domain knowl-
972 edge and additional auxiliary physics objectives: grouping tracks with a common vertex and
973 predicting the underlying physics process for a track. The network structure is shown in
974 Figure 4.3. The GN2 b -tagger form the input vector by concatenating 2 jet variables and
975 19 track reconstruction variables (for up to 40 tracks), normalized to zero mean and unit
976 variance. The output consists of a track-pairing output layer of size 2, a track origin clas-
977 sification layer of 7 categories, and a jet classification layer of size 4 for the probability of
978 each jet being a b -, c -, light- or τ -jet respectively. For b -tagging purpose, a discriminant is

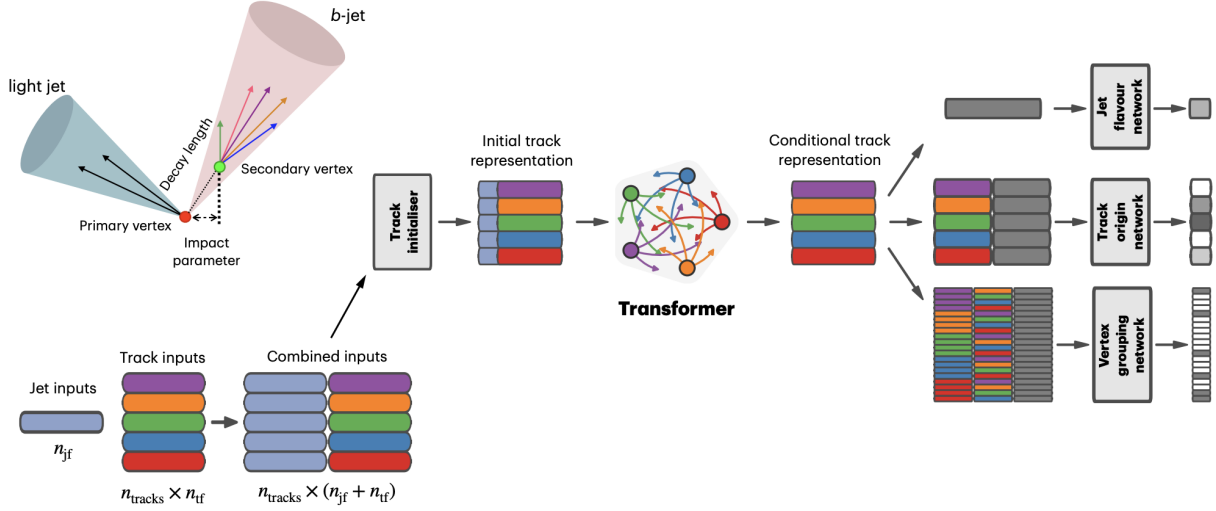


Figure 4.3: Overview of the GN2 architecture. The number of jet and track features are represented by n_{jf} and n_{tf} respectively. The global jet representation and track embeddings output by the Transformer encoder are used as inputs for three task-specific networks [111].

979 defined using these four outputs

$$D_b = \ln \left(\frac{p_b}{f_c p_c + f_\tau p_\tau + (1 - f_c - f_\tau)p_{\text{light}}} \right) \quad (4.1)$$

980 where p_x is the probability of the jet being an x -jet as predicted by GN2, and f_c , f_τ are
981 tunable free parameters controlling balance between c - and light-jet rejection.

982 Simulated SM $t\bar{t}$ and BSM Z' events from pp collisions were used as training and eval-
983 uation samples. In order to minimize bias, both b - and light-jet samples are re-sampled
984 to match c -jet distributions. Figure 4.4 shows the performance of GN2 compared to the
985 previous convolutional neural network-based standard b -tagging algorithm DL1d, in terms
986 of c -, light- and τ -jet rejection as a function of b -tagging efficiency. The network gives a
987 factor of 1.5-4 improvement in experimental applications compared to DL1d [111], without
988 dependence on the choice of MC event generator or inputs from low-level flavor tagging

989 algorithm.

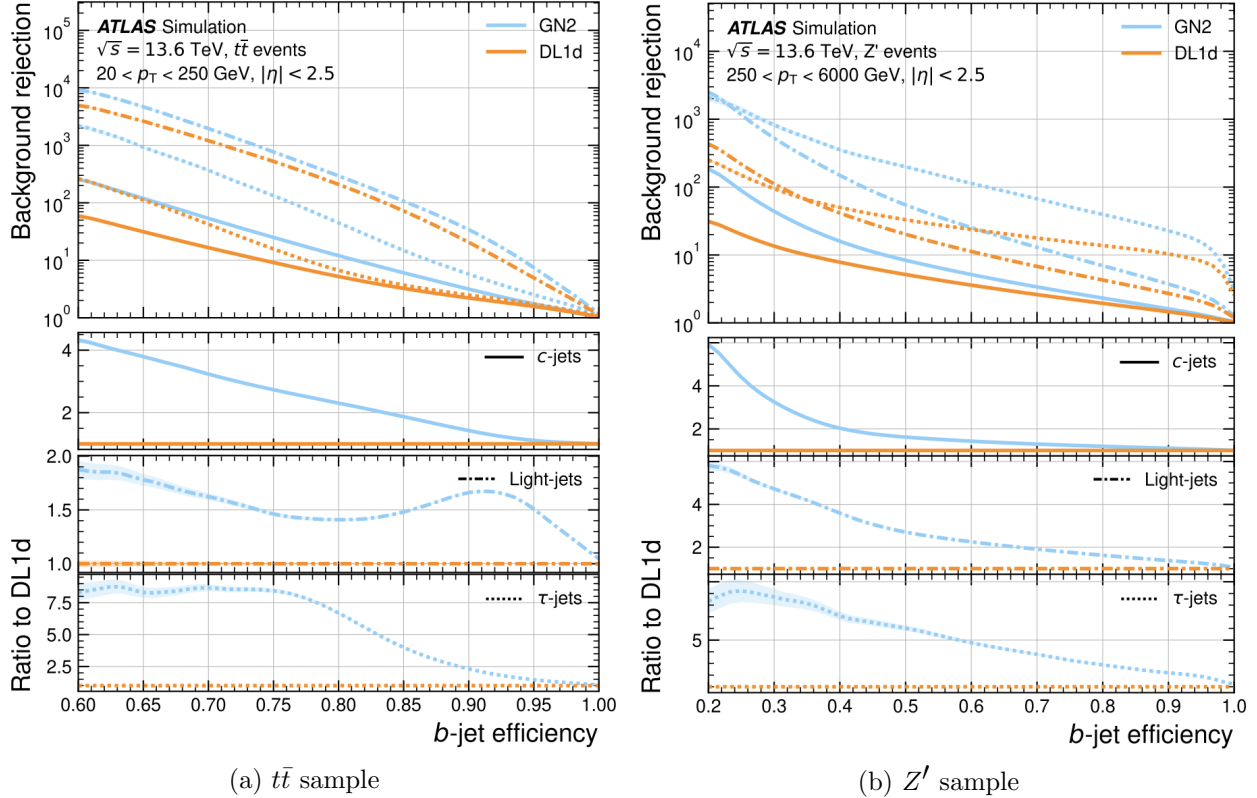


Figure 4.4: The c -, light- and τ -jet rejection rate as a function of b -tagging efficiency for GN2 and DL1d using (a) jets in the $t\bar{t}$ sample, and (b) jets in the Z' sample. The performance ratios of GN2 to DL1d are shown in the bottom panels [111].

990 Efficiency calibration

991 Due to imperfect description of detector response and physics modeling effects in simu-
 992 lation, the b -tagging efficiency predicted by MC simulation $\varepsilon_b^{\text{sim}}$ requires a correction factor
 993 to match the efficiency measured in collision data $\varepsilon_b^{\text{data}}$. The correction scale factors (SFs)
 994 are defined as $\text{SF} = \varepsilon_b^{\text{data}} / \varepsilon_b^{\text{sim}}$ and are determined by data-to-MC calibration using samples
 995 enriched in dileptonic $t\bar{t}$ decays [113]. The resulting SFs are applied to MC simulated jets
 996 individually.

997 4.3 Leptons

998 Lepton reconstruction in ATLAS involves electron and muon reconstruction since tau
999 decays quickly, and depending on decay mode can be reconstructed using either jets or light
1000 leptons. From here on out within this dissertation, leptons will be used exclusively to refer to
1001 electrons and muons. Leptons can be classified into two categories: prompt leptons resulting
1002 from heavy particle decays and non-prompt leptons resulting from detector or reconstruction
1003 effects, or from heavy-flavor hadron decays.

1004 4.3.1 Electrons

1005 Electrons leave energy signature in the detector by interacting with the detector materials
1006 and losing energy in the form of bremsstrahlung photons. A bremsstrahlung photon can
1007 produce an electron-positron pair which can itself deposit signals in the detector, creating a
1008 cascade of particles that can leave multiple of either tracks in the ID or EM showers in the
1009 calorimeters, all of which are considered part of the same EM topo-cluster. Electron signal
1010 signature has three characteristic components: localized energy deposits in the calorimeters,
1011 multiple tracks in the ID and compatibility between the above tracks and energy clusters in
1012 the $\eta \times \phi$ plane [114]. Electron reconstruction in ATLAS follows these steps accordingly.

1013 Seed-cluster reconstruction and track reconstruction are performed sequentially in ac-
1014 cordance with the iterative topo-clustering algorithm and track reconstruction method de-
1015 scribed in section 4.1. The seed-cluster and GSF-refitted track candidate not associated
1016 with a conversion vertex are matched to form an electron candidate. The cluster energy is
1017 then calibrated using multivariate techniques on data and simulation to match the original
1018 electron energy.

1019 **Electron identification**

1020 Additional LH-based identification selections using ID and EM calorimeter information
1021 are implemented to further improve the purity of reconstructed electrons in the $|\eta| < 2.47$ re-
1022 gion of the detector [114]. The electron LH function is built with the signal being prompt elec-
1023 trons and background being objects with similar signature to prompt electrons i.e. hadronic
1024 jet deposits, photon conversions or heavy-flavor hadron decays. Three identification OPs
1025 are defined for physics analyses: *Loose*, *Medium* and *Tight*, optimized for 9 bins in $|\eta|$ and
1026 12 bins in E_T with each OP corresponding to a fixed efficiency requirement for each bin.
1027 For typical EW processes, the target efficiencies for *Loose*, *Medium* and *Tight* start at 93%,
1028 88% and 80% respectively and increase with E_T . Similar to b -tagging OPs, the electron
1029 identification OPs represent a trade-off in signal efficiency and background rejection. The
1030 electron efficiency are estimated using tag-and-probe method on samples of $J/\Psi \rightarrow ee$ and
1031 $Z \rightarrow ee$ [114].

1032 **Electron isolation**

1033 A characteristic distinction between prompt electrons and electrons from background
1034 processes is the relative lack of activity in both the ID and calorimeters within an $\Delta\eta \times \Delta\phi$
1035 area surrounding the reconstruction candidate. Calorimeter-based and track-based electron
1036 isolation variables [114] are defined to quantify the amount of activity around the electron
1037 candidate using topo-clusters and reconstructed tracks respectively.

1038 Calorimeter-based isolation variables $E_T^{\text{cone}XX}$ are computed by first summing the energy
1039 of topo-clusters with barycenters falling within a cone of radius $\Delta R = \sqrt{(\Delta\eta)^2 + (\Delta\phi)^2} =$
1040 $XX/100$ around the direction of the electron candidate. The final isolation variables are

1041 obtained by subtracting from the sum the energy belonging to the candidate electron at the
 1042 core of the cone, then applying corrections for pile-up effects and energy leakage outside of
 1043 the core. Similar to calorimeter-based variables, track-based isolation variables $p_T^{\text{varcone}XX}$
 1044 are calculated by summing all track p_T within a cone of radius ΔR around the electron
 1045 candidate, minus the candidate's contribution. The cone radius is variable as a function of
 1046 p_T and is described as

$$\Delta R \equiv \min \left(\frac{10}{p_T}, \Delta R_{\max} \right), \quad (4.2)$$

1047 where p_T is expressed in GeV and ΔR_{\max} is the maximum cone size, defined to account for
 1048 closer proximity of decay products to the electron in high-momentum heavy particle decays.
 1049 Four isolation operating points are implemented to satisfy specific needs by physics analyses:
 1050 *Loose*, *Tight*, *HighPtCaloOnly* and *Gradient* [114].

1051 Electron charge misidentification

1052 Charge misidentification is a crucial irreducible background, particularly for analyses
 1053 with electron charge selection criteria. Electron charge is determined by the curvature of
 1054 the associated reconstructed track, and misidentification of charge can occur via either an
 1055 incorrect curvature measurement or an incorrectly matched track. Inaccurate measurement
 1056 is more likely for high energy electrons due to the small curvature in track trajectories at
 1057 high p_T , while track matching error usually results from bremsstrahlung pair-production
 1058 generating secondary tracks in close proximity [114]. Suppression of this background is
 1059 assisted via a boosted decision tree discriminant named the Electron Charge ID Selector
 1060 (ECIDS) [115]. The addition of ECIDS removed 90% of electrons with incorrect charge while

1061 selecting 98% of electrons with correct charge from electrons in $Z \rightarrow ee$ events satisfying
1062 *Medium/Tight* identification and *Tight* isolation criteria.

1063 **4.3.2 Muons**

1064 Muons act as minimum-ionizing particles, leaving tracks in the MS or characteristics
1065 energy deposits in the calorimeter and can be reconstructed globally using information from
1066 the ID, MS and calorimeters. Five reconstruction strategies corresponding to five muon
1067 types [116] are utilized in ATLAS:

- 1068 • Combined (CB): the primary ATLAS muon reconstruction method. Combined muons
1069 are first reconstructed using MS tracks then extrapolated to include ID tracks (outside-in strategy). A global combined track fit is performed on both MS and ID tracks.
- 1071 • Inside-out combined (IO): complementary to CB reconstruction. IO muon tracks are
1072 extrapolated from ID to MS, then fitted with MS hits and calorimeter energy loss in a
1073 combined track fit.
- 1074 • MS extrapolated (ME): ME muons are defined as muons with a MS track that cannot
1075 be matched to an ID track using CB reconstruction. ME muons allow extension of
1076 muon reconstruction acceptance to regions not covered by the ID ($2.5 < |\eta| < 2.7$)
- 1077 • Segment-tagged (ST): ST muons are defined as a successfully matched ID track that
1078 satisfies tight angular matching criteria to at least one reconstructed MDT or CSC
1079 segment when extrapolated to the MS. MS reconstruction is used primarily when
1080 muons only crossed one layer of MS chambers.
- 1081 • Calorimeter-tagged (CT): CT muons are defined as an ID track that can be matched to

1082 energy deposits consistent with those of a minimum-ionizing particle when extrapolated
1083 through the calorimeter. CT reconstruction extends acceptance range to regions in the
1084 MS with sparse instrumentation ($|\eta| < 0.1$) with a higher p_T threshold of 5 GeV,
1085 compared to the 2 GeV threshold used by other muon reconstruction algorithms due
1086 to large background contamination at the low p_T range of $15 < p_T < 100$ GeV [117].

1087 Muon identification

1088 Reconstructed muons are further filtered by identification criteria to select for high-
1089 quality prompt muons. Requirements include number of hits in the MS and ID, track fit
1090 properties and compatibility between measurements of the two systems. Three standard OPs
1091 (*Loose*, *Medium*, *Tight*) are defined to better match the needs of different physics analyses
1092 concerning prompt muon p_T resolution, identification efficiency and non-prompt muon rejec-
1093 tion. The default identification OP for ATLAS physics is *Medium* which provides efficiency
1094 and purity suitable for a wide range of analyses while minimizing systematic uncertainties
1095 [116].

1096 Muon isolation

1097 Muons from heavy particle decays are often produced in an isolated manner compared to
1098 muons from semileptonic decays, and is therefore an important tool for background rejection
1099 in many physics analyses. Muon isolation strategies are similar to that of electron in section
1100 4.3.1, with track-based and calorimeter-based isolation variables. Seven isolation OPs are
1101 defined using either or both types of isolation variables [116].

1102 4.4 Missing transverse momentum

1103 Collisions at the LHC happen along the z -axis of the ATLAS coordination system between
1104 two particle beam of equal center-of-mass energy. By conservation of momentum, the sum of
1105 transverse momenta of outgoing particles should be zero. A discrepancy between measured
1106 momentum and zero would then suggest the presence of undetectable particles, which would
1107 consist of either SM neutrinos or some unknown BSM particles, making missing transverse
1108 momentum (E_T^{miss}) an important observable to reconstruct.

1109 Reconstructing E_T^{miss} utilizes information from fully reconstructed leptons, photons, jets
1110 and other matched track-vertex objects not associated with a prompt object (soft signals),
1111 defined with respect to the $x(y)$ -axis as

$$E_{x(y)}^{\text{miss}} = - \sum_{i \in \{\text{hard objects}\}} p_{x(y),i} - \sum_{j \in \{\text{soft signals}\}} p_{x(y),j}, \quad (4.3)$$

1112 where $p_{x(y)}$ is the $x(y)$ -component of p_T for each particle [118]. The following observables
1113 can then be defined:

$$\begin{aligned} \mathbf{E}_T^{\text{miss}} &= (E_x^{\text{miss}}, E_y^{\text{miss}}), \\ E_T^{\text{miss}} &= |\mathbf{E}_T^{\text{miss}}| = \sqrt{(E_x^{\text{miss}})^2 + (E_y^{\text{miss}})^2}, \\ \phi^{\text{miss}} &= \tan^{-1}(E_y^{\text{miss}}/E_x^{\text{miss}}), \end{aligned} \quad (4.4)$$

1114 where E_T^{miss} represents the magnitude of the missing transverse energy vector $\mathbf{E}_T^{\text{miss}}$, and
1115 ϕ^{miss} its direction in the transverse plane. The vectorial sum $\mathbf{E}_T^{\text{miss}}$ can be broken down into

$$\mathbf{E}_T^{\text{miss}} = - \underbrace{\sum_{\text{selected electrons}} \mathbf{p}_T^e - \sum_{\text{selected muons}} \mathbf{p}_T^\mu - \sum_{\text{accepted photons}} \mathbf{p}_T^\gamma - \sum_{\text{accepted } \tau\text{-leptons}} \mathbf{p}_T^\tau}_{\text{hard term}} - \underbrace{\sum_{\text{accepted jets}} \mathbf{p}_T^{\text{jet}} - \sum_{\text{unused tracks}} \mathbf{p}_T^{\text{track}}}_{\text{soft term}}. \quad (4.5)$$

1116 Two OPs are defined for E_T^{miss} , *Loose* and *Tight*, with selections on jet p_T and JVT criteria
1117 [119]. The *Tight* OP is used in this analysis; *Tight* reduces pile-up dependence of E_T^{miss}
1118 by removing the phase space region containing more pile-up than hard-scatter jets, at the
1119 expense of resolution and scale at low pile-up,

1120 4.5 Overlap removal

1121 Since different objects are reconstructed independently, it is possible for the same de-
1122 tector signals to be used to reconstruct multiple objects. An overlap removal strategy is
1123 implemented to resolve ambiguities; the overlap removal process for this analysis applies
1124 selections in Table 4.1 sequentially, from top to bottom.

Table 4.1: Overlap removal process for this analysis, applied sequentially from top to bottom.

Remove	Keep	Matching criteria
Electron	Electron	Shared ID track, $p_{T,1}^e < p_{T,2}^e$
Muon	Electron	Shared ID track, CT muon
Electron	Muon	Shared ID track
Jet	Electron	$\Delta R < 0.2$
Electron	Jet	$\Delta R < 0.4$
Jet	Muon	($\Delta R < 0.2$ or ghost-associated) & $N_{\text{track}} < 3$
Muon	Jet	$\Delta R < \min(0.4, 0.04 + 10\text{GeV}/p_T^\mu)$

1125 Chapter 5. Data & Simulated Samples

1126 5.1 Data samples

1127 Data samples used in this analysis were collected by the ATLAS detector during Run
1128 2 data-taking campaign between 2015-2018. The samples contain pp collisions at center-of-
1129 mass energy of $\sqrt{s} = 13$ TeV with 25 ns bunch-spacing, which corresponds to an integrated
1130 luminosity of 140 fb^{-1} with an uncertainty of 0.83% [87]. The HLT trigger strategy is similar
1131 to that of previous $t\bar{t}t\bar{t}$ observation analysis [44] and include single lepton and dilepton
1132 triggers. Calibration for di-muon and electron-muon triggers were not ready for the samples
1133 used in this analysis, and are therefore not included. Events are also required to contain at
1134 least one lepton matched to the corresponding object firing the trigger. Triggers used are
1135 summarized in Table 5.1.

1136 5.2 Monte Carlo samples

1137 Monte Carlo simulated samples are used to estimate signal acceptance before unblinding,
1138 profile the physics background for the analysis and to study object optimizations. Simulated
1139 samples for this analysis use are generated from ATLAS generalized MC20a/d/e samples for
1140 Run 2, using full detector simulation (FS) and fast simulation (AF3) to simulate detector
1141 response. MC samples used and simulation processes are summarized in Table 5.2

Table 5.1: Summary of all HLT triggers used in this analysis. Events are required to pass at least one trigger.

Trigger	Data period			
	2015	2016	2017	2018
Single electron triggers				
HLT_e24_lhmedium_L1EM20VH	✓	-	-	-
HLT_e60_lhmedium	✓	-	-	-
HLT_e120_lhloose	✓	-	-	-
HLT_e26_lhtight_nod0_ivarloose	-	✓	✓	✓
HLT_e60_lhmedium_nod0	-	✓	✓	✓
HLT_e140_lhloose_nod0	-	✓	✓	✓
Di-electron triggers				
HLT_2e12_lhloose_L12EM10VH	✓	-	-	-
HLT_2e17_lhvloose_nod0	-	✓	-	-
HLT_2e24_lhvloose_nod0	-	-	✓	✓
HLT_2e17_lhvloose_nod0_L12EM15VHI	-	-	-	✓
Single muon trigger				
HLT_mu20_iloose_L1MU15	✓	-	-	-
HLT_mu40	✓	-	-	-
HLT_mu26_ivarmedium	-	✓	✓	✓
HLT_mu50	-	✓	✓	✓

¹¹⁴² 5.2.1 $t\bar{t}Z'$ signal samples

¹¹⁴³ Signal $t\bar{t}Z'$ samples were generated based on the simplified topophilic resonance model in
¹¹⁴⁴ section 2.2.1 where a color singlet vector resonance couples strongly to only top and antitop.
¹¹⁴⁵ Six Z' mass points were utilized for the generation of the signal sample: 1000, 1250, 1500,
¹¹⁴⁶ 2000, 2500 and 3000 GeV. The top- Z' coupling c_t is chosen to be 1 for a narrow resonance
¹¹⁴⁷ peak, and the chirality angle θ is chosen to be $\pi/4$ to suppress loop production of Z' . The
¹¹⁴⁸ samples were then generated with MADGRAPH5_AMC@NLO v.3.5.0 [120] at LO with the
¹¹⁴⁹ NNPDF3.1LO [121] PDF set interfaced with PYTHIA8 [122] using A14 tune and NNPDF2.3lo
¹¹⁵⁰ PDF set for parton showering and hadronization. The resonance width is calculated to be

Table 5.2: Summary of all Monte-Carlo samples used in this analysis. V refers to an EW ($W^\pm/Z/\gamma^*$) or Higgs boson. Matrix element (ME) order refers to the order in QCD of the perturbative calculation. Tune refers to the underlying-event tune of the parton shower (PS) generator.

Process	ME Generator	ME Order	ME PDF	PS	Tune	Sim.
Signals						
$t\bar{t}Z'$	MADGRAPH5_AMC@NLO LO		NNPDF3.1LO	PYTHIA8	A14	FS
$t\bar{t}\bar{t}$ and $t\bar{t}t$						
$t\bar{t}\bar{t}$	MADGRAPH5_AMC@NLO NLO		NNPDF3.0nlo	PYTHIA8	A14	AF3
	MADGRAPH5_AMC@NLO NLO		MMHT2014 LO	HERWIG7	H7-UE-MMHT	AF3
	SHERPA	NLO	NNPDF3.0nnlo	HERWIG7	SHERPA	FS
$t\bar{t}t$	MADGRAPH5_AMC@NLO LO		NNPDF2.3lo	PYTHIA8	A14	AF3
$t\bar{t}V$						
$t\bar{t}H$	POWHEGBOX v2	NLO	NNPDF3.0nlo	PYTHIA8	A14	FS
	POWHEGBOX v2	NLO	NNPDF3.0nlo	HERWIG7	H7.2-Default	FS
$t\bar{t}(Z/\gamma^*)$	MADGRAPH5_AMC@NLO NLO		NNPDF3.0nlo	PYTHIA8	A14	FS
	SHERPA	NLO	NNPDF3.0nnlo	SHERPA	SHERPA	FS
$t\bar{t}W$	SHERPA	NLO	NNPDF3.0nnlo	SHERPA	SHERPA	FS
	SHERPA	LO	NNPDF3.0nnlo	SHERPA	SHERPA	FS
$t\bar{t}$ and Single-Top						
$t\bar{t}$	POWHEGBOX v2	NLO	NNPDF3.0nlo	PYTHIA8	A14	FS
tW	POWHEGBOX v2	NLO	NNPDF3.0nlo	PYTHIA8	A14	FS
$t(q)b$	POWHEGBOX v2	NLO	NNPDF3.0nlo (s)	PYTHIA8	A14	FS
			NNPDF3.0nlo 4f (t)			FS
tWZ	MADGRAPH5_AMC@NLO NLO		NNPDF3.0nlo	PYTHIA8	A14	FS
tZ	MADGRAPH5_AMC@NLO LO		NNPDF3.0nlo 4f	PYTHIA8	A14	FS
$t\bar{t}VV$						
$t\bar{t}WW$	MADGRAPH5_AMC@NLO LO		NNPDF3.0nlo	PYTHIA8	A14	FS
$t\bar{t}WZ$	MADGRAPH	LO	NNPDF3.0nlo	PYTHIA8	A14	AF3
$t\bar{t}HH$	MADGRAPH	LO	NNPDF3.0nlo	PYTHIA8	A14	AF3
$t\bar{t}WH$	MADGRAPH	LO	NNPDF3.0nlo	PYTHIA8	A14	AF3
$t\bar{t}ZZ$	MADGRAPH	LO	NNPDF3.0nlo	PYTHIA8	A14	AF3
$V(VV)+\text{jets}$ and VH						
$V+\text{jets}$	SHERPA	NLO	NNPDF3.0nnlo	SHERPA	SHERPA	FS
$VV+\text{jets}$	SHERPA	NLO	NNPDF3.0nnlo	SHERPA	SHERPA	FS
		LO ($gg \rightarrow VV$)				FS
$VVV+\text{jets}$	SHERPA	NLO	NNPDF3.0nnlo	SHERPA	SHERPA	FS
VH	POWHEGBOX v2	NLO	NNPDF3.0aznlo	PYTHIA8	A14	FS

₁₁₅₁ 4% for $c_t = 1$.

₁₁₅₂ 5.2.2 Background samples

₁₁₅₃ SM $t\bar{t}t\bar{t}$ background

₁₁₅₄ The nominal SM $t\bar{t}t\bar{t}$ sample was generated with MADGRAPH5_AMC@NLO [120] at
₁₁₅₅ NLO in QCD with the NNPDF3.0nlo [121] PDF set and interfaced with PYTHIA8.230 [122]
₁₁₅₆ using A14 tune [123]. Decays for top quarks are simulated at LO with MADSPIN [124,
₁₁₅₇ 125] to preserve spin information, while decays for b - and c -hadrons are simulated with
₁₁₅₈ EVTGEN v1.6.0 [126]. The renormalization and factorization scales μ_R and μ_F are set
₁₁₅₉ to $\sqrt{m^2 + p_T^2}/4$, which represents the sum of transverse mass of all particles generated
₁₁₆₀ from the ME calculation [127]. The ATLAS detector response was simulated with AF3.
₁₁₆₁ Additional auxiliary $t\bar{t}t\bar{t}$ samples are also generated to evaluate the impact of generator and
₁₁₆₂ PS uncertainties as shown in 5.2.

₁₁₆₃ $t\bar{t}W$ background

₁₁₆₄ Nominal $t\bar{t}W$ sample was generated using SHERPA v2.2.10 [128] at NLO in QCD with
₁₁₆₅ the NNPDF3.0nnlo [121] PDF with up to one extra parton at NLO and two at LO, which
₁₁₆₆ are matched and merged with SHERPA PS based on Catani-Seymour dipole factorization
₁₁₆₇ [129] using the MEPS@NLO prescription [130–133] and a merging scale of 30 GeV. Higher-
₁₁₆₈ order ME corrections are provided in QCD by the OpenLoops 2 library [134–136] and in
₁₁₆₉ EW from $\mathcal{O}(\alpha^3) + \mathcal{O}(\alpha_S^2\alpha^2)$ (LO3 & NLO2) via two sets of internal event weights. An
₁₁₇₀ alternative sample with only EW corrections at LO from $\mathcal{O}(\alpha_S\alpha^3)$ (NLO3) diagrams were
₁₁₇₁ also simulated with the same settings.

₁₁₇₂ **$t\bar{t}(Z/\gamma^*)$ background**

₁₁₇₃ Nominal $t\bar{t}(Z/\gamma^*)$ samples were generated separately for different ranges of dilepton in-
₁₁₇₄ variant mass $m_{\ell\ell}$ to account for on-shell and off-shell Z/γ^* production. Sample for $m_{\ell\ell}$
₁₁₇₅ between 1 and 5 GeV was produced using MADGRAPH5_AMC@NLO [120] at NLO with
₁₁₇₆ the NNPDF3.0nlo [121] PDF set, interfaced with PYTHIA8.230 [122] using A14 tune [123] and
₁₁₇₇ NNPDF2.3l0 PDF set. Sample for $m_{\ell\ell} < 5$ GeV was produced with SHERPA v2.2.10 [128]
₁₁₇₈ at NLO using NNPDF3.0nnlo PDF set. To account for generator uncertainty, an alternative
₁₁₇₉ $m_{\ell\ell} > 5$ GeV sample was generated with identical settings to the low $m_{\ell\ell}$ sample. The
₁₁₈₀ ATLAS detector response was simulated with full detector simulation (FS).

1181 Chapter 6. Analysis Strategy

1182 6.1 Event selection

1183 Events for the analysis first are preselected following a list of criteria to optimize for event
1184 quality and background rejection. The following criteria are applied sequentially from top
1185 to bottom along with cleaning and veto cuts

1186 1. **Good Run List (GRL)**: data events must be part of a predefined list of suitable
1187 runs and luminosity blocks [[137](#)].

1188 2. **Primary vertex**: events must have at least one reconstructed vertex matched to 2 or
1189 more associated tracks with $p_T > 500$ MeV.

1190 3. **Trigger**: events must be selected by at least one trigger in Table 5.1.

1191 4. **Kinematic selection**: events must have exactly two *Tight* leptons with the same
1192 electric charge, or at least three *Tight* leptons of any charge. The leading lepton must
1193 have $p_T > 28$ GeV, and all leptons must satisfy $p_T > 15$ GeV.

1194 Events are separated into two channels based on the number of leptons: same-sign di-
1195 lepton (SS2L) for events with exactly two leptons of the same charge, or multilepton (ML)
1196 for events with three or more leptons. The channels are further separated into regions defined
1197 in section 6.2 to prepare for analysis.

1198 Additional selections are applied based on the lepton flavors present. In the SS2L channel,
1199 if both leptons are electrons, the invariant mass m_{ll} must satisfy $m_{ll} < 81$ GeV and $m_{ll} > 101$
1200 GeV to suppress background involving Z -bosons. In the ML channel, the same criteria must
1201 be satisfied for every opposite-sign same-flavor pair of leptons in an event.

₁₂₀₂ **6.1.1 Object definition**

₁₂₀₃ Table 6.1 shows the selections used in this analysis. Each selection comes with associated
₁₂₀₄ calibration scale factors (SFs) to account for discrepancies between data and MC simulation,
₁₂₀₅ and are applied multiplicatively to MC event weights.

Table 6.1: Summary of object selection criteria used in this analysis. ℓ_0 refers to the leading lepton in the event.

Selection	Electrons	Muons	Jets
p_T [GeV]	> 15 $p_T(\ell_0) > 28$	> 15	> 20
$ \eta $	$1.52 \leq \eta < 2.47$ < 1.37	< 2.5	< 2.5
Identification	<i>TightLH</i> pass ECIDS ($ee/e\mu$)	<i>Medium</i>	NNJvt <i>FixedEffPt</i> ($p_T < 60$, $ \eta < 2.4$)
Isolation	<i>Tight_VarRad</i>	<i>PflowTight_VarRad</i>	
Track-vertex assoc.			
$ d_0^{\text{BL}}(\sigma) $	< 5	< 3	
$ \Delta z_0^{\text{BL}} \sin \theta $ [mm]	< 0.5	< 0.5	

₁₂₀₆ **6.1.2 Event categorization**

₁₂₀₇ Simulated events are categorized using truth information of leptons (e/μ) and their orig-
₁₂₀₈ inating MC particle (mother-particle). Each lepton can be classified as either prompt or
₁₂₀₉ non-prompt, with non-prompt leptons further categorized for background estimation pur-
₁₂₁₀ poses. If an event contains only prompt leptons, the event is classified as its correspond-
₁₂₁₁ ing process. If the event contains one non-prompt lepton, the event is classified as the corre-
₁₂₁₂ sponding type of the non-prompt lepton. If the event contains more than one non-prompt
₁₂₁₃ lepton, the event is classified as other.

- ₁₂₁₄ • **Prompt:** if the lepton originates from $W/Z/H$ boson decays, or from a mother-
- ₁₂₁₅ particle created by a final state photon.
- ₁₂₁₆ • **Non-prompt:**
- ₁₂₁₇ – **Charge-flip (e only):** if the reconstructed charge of the lepton differs from that
 - ₁₂₁₈ of the first mother-particle.
 - ₁₂₁₉ – **Material conversion (e only):** if the lepton originated from a photon conversion
 - ₁₂₂₀ and the mother-particle is an isolated prompt photon, non-isolated final state
 - ₁₂₂₁ photon, or heavy boson.
 - ₁₂₂₂ – **γ^* -conversion (e only):** if the lepton originated from a photon conversion and
 - ₁₂₂₃ the mother-particle is a background electron.
 - ₁₂₂₄ – **Heavy flavor decay:** if the lepton originated from a b - or c -hadron.
 - ₁₂₂₅ – **Fake:** if the lepton originated from a light- or s -hadron, or if the truth type of
 - ₁₂₂₆ the lepton is hadron.
 - ₁₂₂₇ – **Other:** any lepton that does not belong to one of the above categories.

₁₂₂₈ 6.2 Analysis regions

₁₂₂₉ Events are selected and categorized into analysis regions belonging to one of two types:

₁₂₃₀ control regions (CRs) enriched in background events, and signal regions (SRs) enriched in

₁₂₃₁ signal events. This allows for the examination and control of backgrounds and systematic

₁₂₃₂ uncertainties, as well as study of signal sensitivities. The signal is then extracted from

₁₂₃₃ the SRs with a profile LH fit using all regions. The full selection criteria for each region are

¹²³⁴ summarized in Table 6.2. The background compositions in different CRs and SR sub-regions
¹²³⁵ are shown in Figure 6.1.

Table 6.2: Definitions of signal, control and validation regions (VR) used in this analysis. N_{jets} and N_b refers to the number of jets and number of b -tagged jets respectively. ℓ_1 refers to the leading lepton, ℓ_2 refers to the subleading lepton and so on. H_T refers to the p_T scalar sum of all leptons and jets in the event. $m_{\ell\ell}$ refers to the dilepton invariant mass, which must not coincide with the Z -boson mass range of 81-101 GeV for SS2L+3L events.

Region	Channel	N_{jets}	N_b	Other selections	Fitted variable
CR Low m_{γ^*}	SS $e\ell$	[4, 6)	≥ 1	ℓ_1/ℓ_2 is from virtual photon decay $\ell_1 + \ell_2$ not from material conversion	event yield
CR Mat. Conv.	SS $e\ell$	[4, 6)	≥ 1	ℓ_1/ℓ_2 is from material conversion $\ell_1 + \ell_2$ not conversion candidates	event yield
CR HF μ	$\ell\mu\mu$	≥ 1	1	$100 < H_T < 300$ GeV $E_T^{\text{miss}} > 35$ GeV total charge = ± 1	$p_T(\ell_3)$
CR HF e	$e\ell\ell$	≥ 1	1	$\ell_1 + \ell_2$ not conversion candidates $100 < H_T < 275$ GeV $E_T^{\text{miss}} > 35$ GeV total charge = ± 1	$p_T(\ell_3)$
CR $t\bar{t}W^+$	SS $\ell\mu$	≥ 4	≥ 2	$ \eta(e) < 1.5$ for $N_b = 2$: $H_T < 500$ GeV or $N_{\text{jets}} < 6$ for $N_b \geq 3$: $H_T < 500$ GeV total charge > 0	N_{jets}
CR $t\bar{t}W^-$	SS $\ell\mu$	≥ 4	≥ 2	$ \eta(e) < 1.5$ for $N_b = 2$: $H_T < 500$ GeV or $N_{\text{jets}} < 6$ for $N_b \geq 3$: $H_T < 500$ GeV total charge < 0	N_{jets}
CR 1b(+)	SS2L+3L	≥ 4	1	$\ell_1 + \ell_2$ not from material conversion $H_T > 500$ GeV total charge > 0	N_{jets}
CR 1b(-)	SS2L+3L	≥ 4	1	$\ell_1 + \ell_2$ not from material conversion $H_T > 500$ GeV total charge < 0	N_{jets}
VR $t\bar{t}Z$	3L $\ell^\pm\ell^\mp$	≥ 4	≥ 2	$m_{\ell\ell} \in [81, 101]$ GeV	$N_{\text{jets}}, m_{\ell\ell}$
VR $t\bar{t}W +1b$	SS2L+3L			CR $t\bar{t}W^\pm$ CR 1b(\pm)	N_{jets}
VR $t\bar{t}W +1b+SR$	SS2L+3L			CR $t\bar{t}W^\pm$ CR 1b(\pm) SR	N_{jets}
SR	SS2L+3L	≥ 6	≥ 2	$H_T > 500$ GeV $m_{\ell\ell} \notin [81, 101]$ GeV	H_T

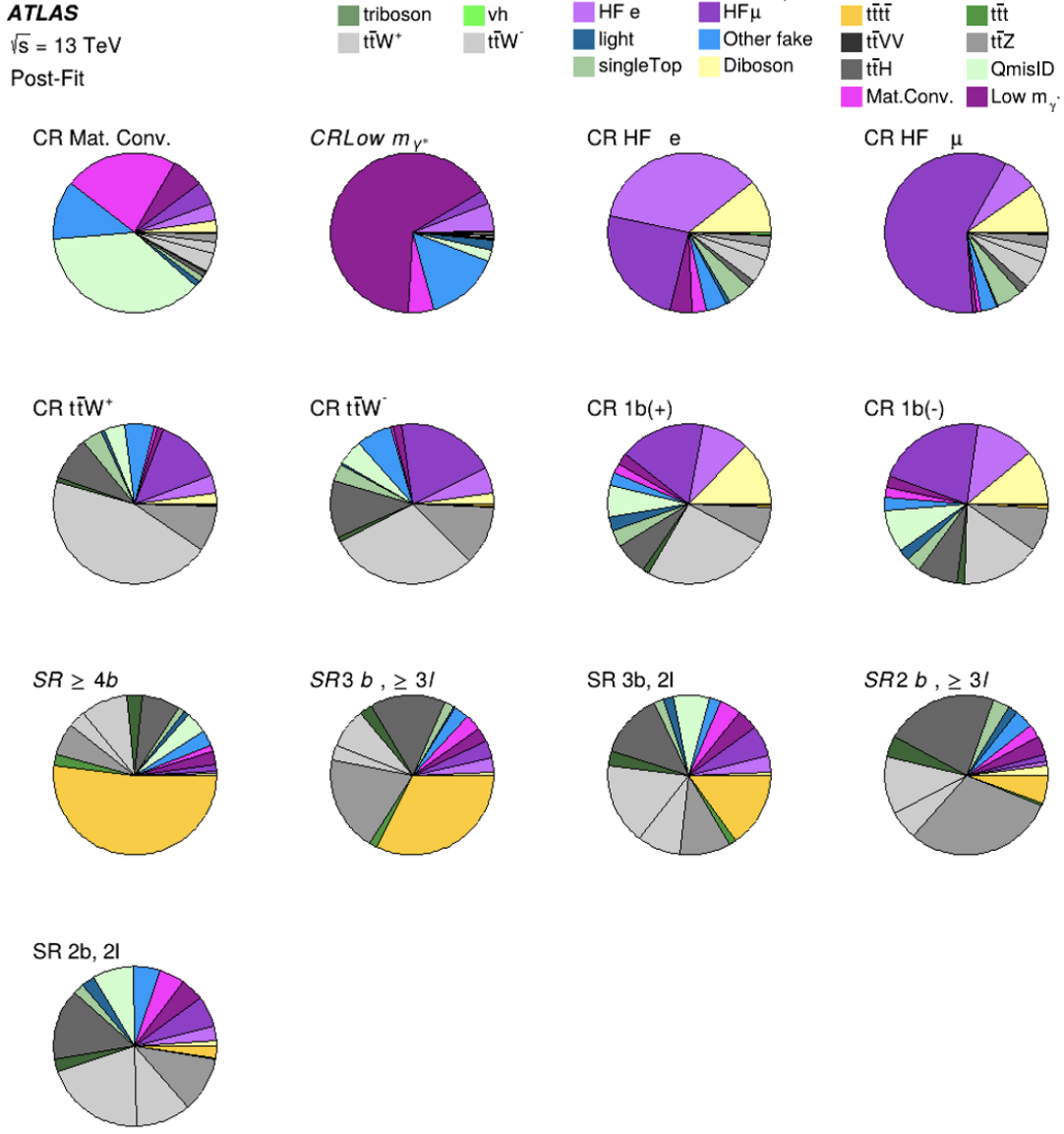


Figure 6.1: Post-fit background composition in each analysis region and sub-region. The fit was performed using ideal pseudo-datasets (Asimov data) in the SR.

¹²³⁶ 6.2.1 Signal regions

¹²³⁷ All events selected for the SR must satisfy the following criteria:

- ¹²³⁸ • Contains 6 or more jets, with at least 2 jets b -tagged at the 85% OP.
- ¹²³⁹ • Scalar sum of the transverse momenta of all leptons and jets $H_T > 500 \text{ GeV}$.

- 1240 • Dilepton invariant mass $m_{\ell\ell}$ does not coincide with the Z -boson mass range of $81 - 101$

1241 GeV

1242 The SR is further divided into sub-regions by the number of b -tagged jets and leptons

1243 present to study signal behavior and sensitivity with respect to the selection variables.

Table 6.3: Definitions of SR sub-regions. Events are sorted into different sub-regions based on the number of b -tagged jets and leptons present.

Sub-region	Selection criteria	
	b -jets	leptons
SR 2b2l	$N_b = 2$	$N_l = 2$
SR 2b3l4l	$N_b = 2$	$N_l \geq 3$
SR 3b2l	$N_b = 3$	$N_l = 2$
SR 3b3l4l	$N_b = 3$	$N_l \geq 3$
SR 4b	$N_b \geq 4$	

1244 **Signal extraction**

1245 Signal extraction in the SR is performed via a binned profile likelihood (LH) fit as de-

1246 scribed in section 8.1 using H_T as the discriminant observable. The discriminant observable

1247 for a LH fit serves as the set of observed data upon which the LH function is constructed.

1248 Ideally, the chosen observable shows significant separation between the functional forms of

1249 the signal and background distributions, allowing for effective separation of the two. Fig-

1250 ure 6.2 shows several pre-fit kinematic distributions in the inclusive SR. From empirical

1251 optimization studies, H_T possesses good discriminating power compared to other observ-

1252 ables constructed using event-level information.

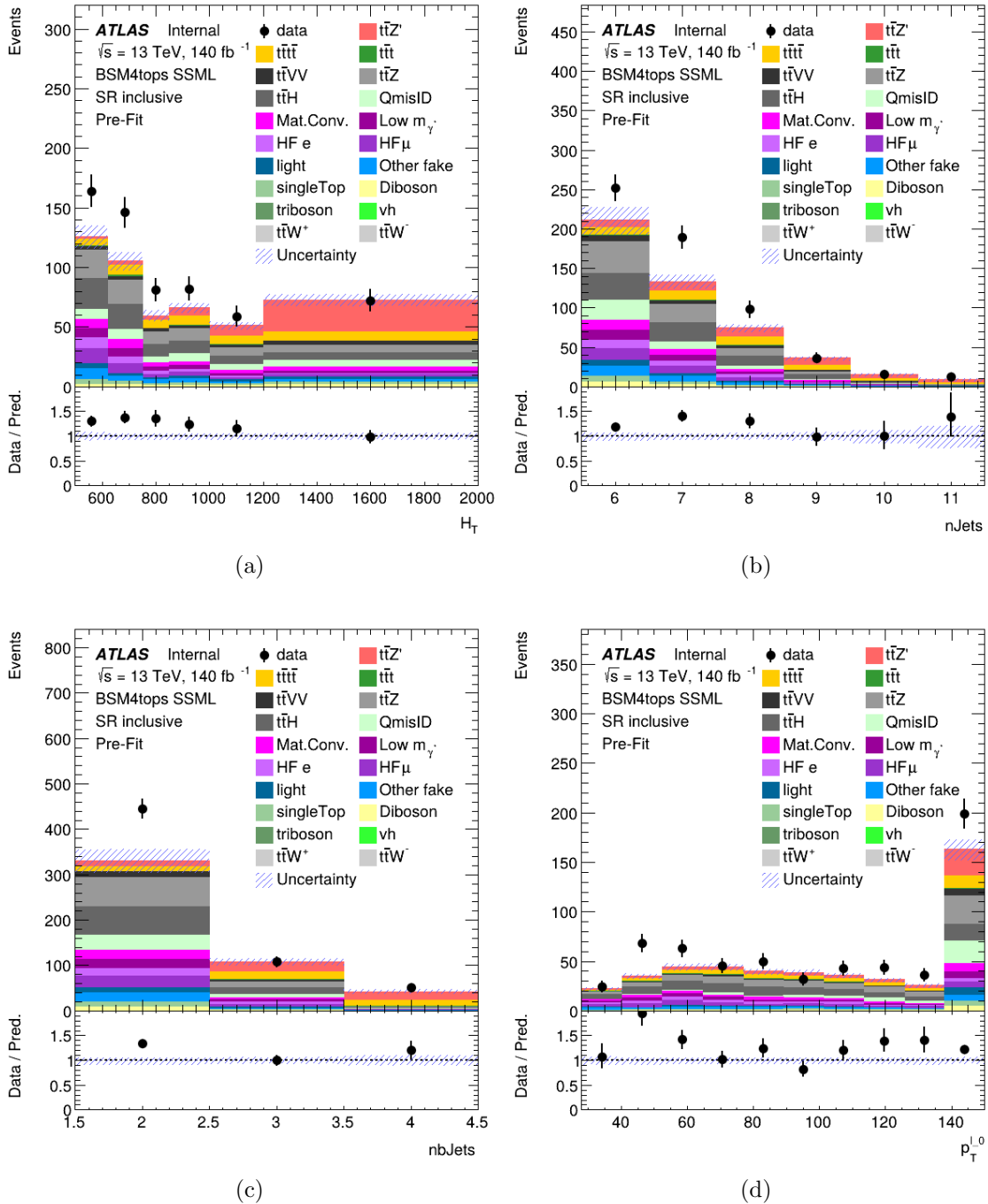


Figure 6.2: Pre-fit kinematic distributions and event compositions for several observables in the inclusive SR. The shaded band represents the uncertainty in the total distribution. The first and last bins of each distribution contain underflow and overflow events respectively.

1253 **6.2.2 Control regions**

1254 Control regions are defined for each background to be enriched in the targeted process, in
1255 order to maximize the background's purity and minimize contamination from other sources
1256 within the region. This helps to constrain and reduce correlation between background nor-
1257 malization factors in the final fit. Fit variables and selection criteria are determined via
1258 optimization studies performed on CRs that aimed to achieve the largest discriminating
1259 power possible between the target background and other event types.

1260 **$t\bar{t}W$ background CRs**

1261 Theoretical modeling for $t\bar{t}W$ +jets background in the phase space of this analysis suffers
1262 from large uncertainties, especially at high jet multiplicities [138]. A data-driven method was
1263 employed in a similar manner to the SM $t\bar{t}t\bar{t}$ observation analysis [44] to mitigate this effect,
1264 and are described in further details in section 6.3.3. The method necessitates the definition
1265 of two groups of dedicated CRs to estimate the flavor composition and normalization of $t\bar{t}W$
1266 +jets background: CR $t\bar{t}W$ +jets to constrain flavor composition, and CR 1b to constrain
1267 the jet multiplicity spectrum. These are further split into CR $t\bar{t}W^\pm$ and CR 1b(\pm) due to
1268 the pronounced asymmetry in $t\bar{t}W$ production from pp collisions, with $t\bar{t}W^+$ being produced
1269 at approximately twice the rate of $t\bar{t}W^-$ [139].

1270 Events in CR $t\bar{t}W^\pm$ are required to contain at least two b -tagged jets similar to the SR
1271 to determine the $t\bar{t}W$ normalization within an SR-related phase space. Orthogonality with
1272 SR is ensured by requiring $H_T < 500$ GeV or $N_{\text{jets}} < 6$ when $N_b = 2$, and $H_T < 500$
1273 GeV when $N_b \geq 3$. Events in CR 1b(\pm) are required to have $H_T > 500$ GeV and at least
1274 four jets to encompass events with high N_{jets} , which can be used to determine the $t\bar{t}W$ jet

₁₂₇₅ multiplicity spectrum for fitting $a_{0,1}$. The selection criteria also include exactly one b -tagged
₁₂₇₆ jet to maintain orthogonality with the SR.

₁₂₇₇ **Fake/non-prompt background CRs**

₁₂₇₈ Selection for fake/non-prompt CRs are determined using the `DFCommonAddAmbiguity`
₁₂₇₉ (`DFCAA`) variable for reconstructed leptons.

Table 6.4: List of possible assigned values for `DFCAA`.

DFCAA	Description
-1	No 2nd track found
0	2nd track found, no conversion found
1	Virtual photon conversion candidate
2	Material conversion candidate

₁₂₈₀ Four CRs are defined for the three main types of fake/non-prompt backgrounds in the
₁₂₈₁ analysis - virtual photon (γ^*) conversion, photon conversion in detector material (Mat.
₁₂₈₂ Conv.) and heavy flavor decays (HF). The full selection criteria for fake/non-prompt CRs
₁₂₈₃ are shown in Table 6.2.

- ₁₂₈₄ • **Low m_γ^* :** events with an e^+e^- pair produced from a virtual photon.

₁₂₈₅ Events are selected if there are two same-sign leptons with at least one electron recon-
₁₂₈₆ structed as an internal conversion candidate, and neither reconstructed as a material
₁₂₈₇ conversion candidate.

- ₁₂₈₈ • **Mat. Conv.:** events with an electron originating from photon conversion within the
₁₂₈₉ detector material.

₁₂₉₀ Events are selected if there are two same-sign leptons with at least one electron recon-
₁₂₉₁ structed as a material conversion candidate.

- 1292 • **HF** $e(\mu)$: events with a reconstructed non-prompt lepton from semi-leptonic decays of
1293 b - and c -hadrons (heavy flavor decays).

1294 Events are selected if there are three leptons with at least two electrons (muons), with
1295 no lepton reconstructed as a conversion candidate.

1296 6.3 Background estimation

1297 Background in this analysis consist of SM processes that can result in a signal signature
1298 similar to a $t\bar{t}t\bar{t}$ SSML final state and can be divided into two types, reducible and irre-
1299 ducible. Reducible background consists of processes that do not result in a SSML final state
1300 physically, but are reconstructed as such due to detector and reconstruction effects. Three
1301 main types of reducible background are considered: charge misidentification (QmisID) and
1302 fake/non-prompt leptons. Fake/non-prompt lepton backgrounds are estimated using tem-
1303 plate fitting method, where MC simulations are normalized to their theoretical SM cross
1304 section via floating normalization factors (NFs) constrained by the corresponding CRs. Lep-
1305 ton charge misidentification background contaminates the SR with opposite-sign events, and
1306 are estimated using a data-driven method described in section 6.3.2 along with ECIDS de-
1307 scribed in section 4.3.1.

1308 Irreducible background consists of SM processes that result in SSML final states physi-
1309 cally with all leptons being prompt. The dominating background in the SR are SM $t\bar{t}t\bar{t}$, $t\bar{t}W$,
1310 $t\bar{t}Z$, and $t\bar{t}H$ production with smaller contributions from VV , VVV , VH and rarer processes
1311 like $t\bar{t}VV$, tWZ , tZq and $t\bar{t}t$. Most irreducible backgrounds are estimated using template
1312 fitting method, with the exception of $t\bar{t}W$ + jets background. The $t\bar{t}W$ + jets bacground is
1313 instead given four dedicated CRs, and estimated using a data-driven method with a fitted

₁₃₁₄ function parameterized in N_{jets} . All CRs and SR are included in the final profile LH fit to
₁₃₁₅ data.

₁₃₁₆ 6.3.1 Template fitting for fake/non-prompt estimation

₁₃₁₇ Template fitting method is a semi-data-driven approach [138] that estimates fake/non-
₁₃₁₈ prompt background distributions by fitting the MC kinematic profile of background processes
₁₃₁₉ arising from fake/non-prompt leptons to data. Each of the four main sources of fake/non-
₁₃₂₀ prompt leptons is assigned a free-floating NF constrained by a CR enriched with the corre-
₁₃₂₁ sponding background resulting in four $\text{NF}_{\text{HF } e}$, $\text{NF}_{\text{HF } \mu}$, $\text{NF}_{\text{Mat. Conv.}}$ and $\text{NF}_{\text{Low } m_{\gamma^*}}$. The
₁₃₂₂ NFs are fitted simultaneously with the signal.

₁₃₂₃ 6.3.2 Charge misidentification data-driven estimation

₁₃₂₄ The ee and $e\mu$ channels in the SS2L region are contaminated with opposite-sign (OS)
₁₃₂₅ dilepton events with one misidentified charge. Charge misidentification (QmisID) largely
₁₃₂₆ affects electrons due to muons' precise curvature information using ID and MS measurements
₁₃₂₇ and low bremsstrahlung rate. The charge flip rates are significant at higher p_T and varies
₁₃₂₈ with $|\eta|$ which is proportional to the amount of detector material the electron interacted
₁₃₂₉ with.

₁₃₃₀ The charge flip probability ϵ is estimated in this analysis with a data-driven method
₁₃₃₁ [140] using a sample of $Z \rightarrow e^+e^-$ events with additional constraints on the invariant mass
₁₃₃₂ m_{ee} to be within 10 GeV of the Z -boson mass. The Z -boson mass window is defined to
₁₃₃₃ be within 4σ to include most events within the peak, and is determined by fitting the m_{ee}
₁₃₃₄ spectrum of the two leading electrons to a Breit-Wigner function, resulting in a range of

1335 [65.57, 113.49] for SS events and [71.81, 109.89] for OS events. Background contamination
 1336 near the peak is assumed to be uniform and subtracted using a sideband method. Since the
 1337 Z -boson decay products consist of a pair of opposite-sign electrons, all same-sign electron
 1338 pairs are considered affected by charge misidentification.

1339 Let N_{ij}^{SS} be the number of events with SS electrons with the leading electron in the
 1340 i^{th} 2D bin in $(p_T, |\eta|)$ and the sub-leading electron in the j^{th} bin. Assuming the QmisID
 1341 probabilities of electrons in an event are uncorrelated, N_{ij}^{SS} can be estimated as

$$N_{ij}^{\text{SS}} = N_{ij}^{\text{tot}} [\epsilon_i(1 - \epsilon_j) + \epsilon_j(1 - \epsilon_i)], \quad (6.1)$$

1342 where N_{ij}^{tot} is the total number of events in the i^{th} and j^{th} bin regardless of charge, and
 1343 $\epsilon_{i(j)}$ is the QmisID rate in the $i^{\text{th}}(j^{\text{th}})$ bin. Assuming N_{ij}^{SS} follows a Poisson distribution
 1344 around the expectation value \bar{N}_{ij}^{SS} , the $(i, n)^{\text{th}}$ rate ϵ can be estimated by minimizing a
 1345 negative-LLH function parameterized in p_T and $|\eta|$,

$$\begin{aligned} -\ln(\mathcal{L}(\epsilon | N_{\text{SS}})) &= -\ln \prod_{ij} \frac{(N_{ij}^{\text{tot}})^{N_{ij}^{\text{SS}}} \cdot e^{N_{ij}^{\text{tot}}}}{N_{ij}^{\text{SS}}!} \\ &= -\sum_{ij} \left[N_{ij}^{\text{SS}} \ln(N_{ij}^{\text{tot}}(\epsilon_i(1 - \epsilon_j) + \epsilon_j(1 - \epsilon_i))) - N_{ij}^{\text{tot}}(\epsilon_i(1 - \epsilon_j) + \epsilon_j(1 - \epsilon_i)) \right]. \end{aligned} \quad (6.2)$$

1346 The QmisID rates are then calculated separately for SR and CRs with different electron
 1347 definitions i.e. CR Low m_{γ^*} , CR Mat. Conv., CR $t\bar{t}W^\pm$, using events from data after
 1348 applying region-specific lepton selections and ECIDS. The events are required to satisfy
 1349 SS2L kinematic selections but contains OS electrons. The following weight is applied to OS

1350 events to correct for misidentified SS events within the region,

$$w = \frac{\epsilon_i + \epsilon_j - 2\epsilon_i\epsilon_j}{1 - \epsilon_i - \epsilon_j + 2\epsilon_i\epsilon_j}. \quad (6.3)$$

1351 The QmisID rates calculated for SR and CR $t\bar{t}W$ are shown in Figure 6.3

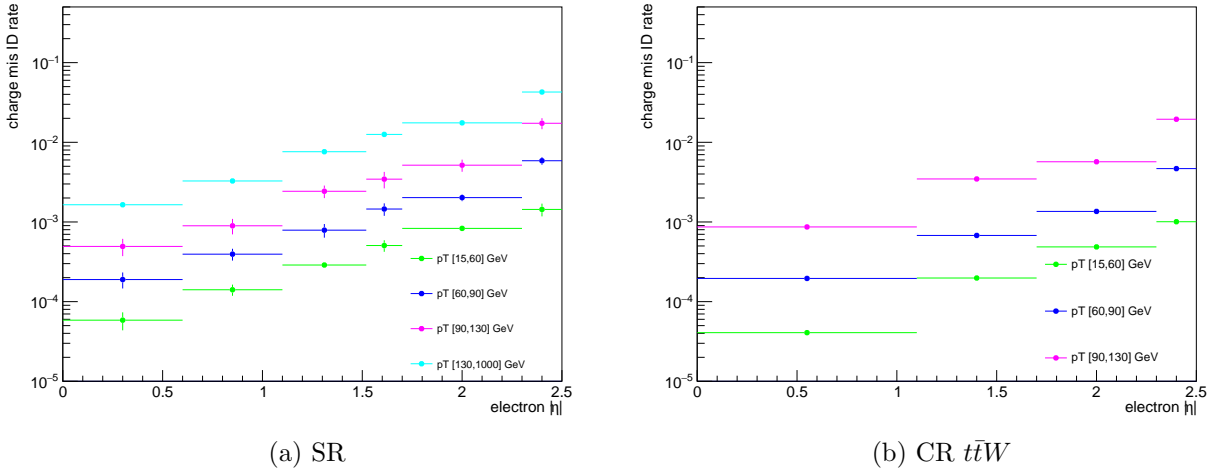


Figure 6.3: Charge flip rate calculated for SR and CR $t\bar{t}W$ in bins of $|\eta|$ and p_T .

1352 The QmisID rates obtained after applying w contain a dependency on jet multiplicity
 1353 and are underestimated at higher N_{jets} . This dependency affect the SR which require events
 1354 with ≥ 6 jets, and is corrected by applying a correction factor $SF_{i,n} = \epsilon_{i,n}/\epsilon_{i,N}$ where N is
 1355 the inclusive bin containing all N_{jets} and $\epsilon_{i,n}$ is the QmisID rate obtained from Equation 6.2
 1356 in the $(i, n)^{\text{th}}$ 2D bin in (p_T, N_{jets}) . Jet multiplicity and consequently the obtained SFs are
 1357 assumed to be independent of $|\eta|$.

1358 6.3.3 $t\bar{t}W$ background data-driven estimation

1359 Previously, the $t\bar{t}W$ background in $t\bar{t}t\bar{t}$ final state analysis was handled by assigning large
 1360 ad-hoc systematic uncertainties to $t\bar{t}W$ events with 7 or more jets [46]. A semi-data-driven

₁₃₆₁ method [141] was shown to be effective in the SM $t\bar{t}t\bar{t}$ observation analysis [44] by improving
₁₃₆₂ $t\bar{t}W$ modeling, especially in the showering step and switching $t\bar{t}W$ systematic uncertainties
₁₃₆₃ from predominantly modeling to statistical.

₁₃₆₄ The data-driven method applies correction factors obtained from a fitted function pa-
₁₃₆₅ rameterized in N_{jets} to $t\bar{t}W$ MC kinematic distributions. The QCD scaling patterns [142] can
₁₃₆₆ be represented by ratio of successive exclusive jet cross-sections

$$R_{(n+1)/n} = \frac{\sigma_{n+1}}{\sigma_n} = e^{-b} + \frac{\bar{n}}{n+1} = a_0 + \frac{a_1}{1+(j-4)}, \quad (6.4)$$

₁₃₆₇ where $a_{0(1)}$ and b are constants, n is the number of jets in addition to the hard process, j
₁₃₆₈ is the inclusive number of jets, and \bar{n} is the expectation value for the Poisson distribution
₁₃₆₉ of exclusive jet cross-section at jet multiplicity n . The $t\bar{t}W$ ME for SS2L events gives 4 jets
₁₃₇₀ in the hard process, so n is defined starting from the 5th jets and the inclusive number of
₁₃₇₁ jets $j = n + 4$. The two terms in Equation 6.4 correspond to staircase and Poisson scaling
₁₃₇₂ in cross section between successive jet multiplicities and are sensitive to high and low jet
₁₃₇₃ multiplicity events respectively [142]. The scaling pattern can then be reparameterized in
₁₃₇₄ a_0 and a_1 to obtain the $t\bar{t}W$ yield at $j' \equiv j + 1$ jets

$$\text{Yield}_{t\bar{t}W(j')} = \text{Yield}_{t\bar{t}W(N_{\text{jets}}=4)} \times \prod_{j=4}^{j'-1} \left(a_0 + \frac{a_1}{1+(j-4)} \right) \quad (6.5)$$

₁₃₇₅ with $j \geq 4$. The $t\bar{t}W$ yield in the 4-jet bin can be represented by a NF applied to $t\bar{t}W$ MC
₁₃₇₆ simulation

$$\text{Yield}_{t\bar{t}W(N_{\text{jets}}=4)} = \text{NF}_{t\bar{t}W(N_{\text{jets}}=4)} \times \text{MC}_{t\bar{t}W(N_{\text{jets}}=4)}. \quad (6.6)$$

₁₃₇₇ To account for the asymmetry in $t\bar{t}W^+$ and $t\bar{t}W^-$ cross-sections, $\text{NF}_{t\bar{t}W(N_{\text{jets}}=4)}$ is further

1378 split into $\text{NF}_{t\bar{t}W^\pm(N_{\text{jets}}=4)}$ assuming the scaling is the same for both processes. Both NFs

1379 are left free-floating to constrain $t\bar{t}W$ yields in the 4-jet bin within CR 1b(+) and CR 1b(-).

1380 The final N_{jets} -parameterized function can then be represented by $\text{NF}_{t\bar{t}W(j')}$ as

$$\text{NF}_{t\bar{t}W(j')} = \left(\text{NF}_{t\bar{t}W^+(N_{\text{jets}}=4)} + \text{NF}_{t\bar{t}W^-(N_{\text{jets}}=4)} \right) \times \prod_{j=4}^{j'-1} \left(a_0 + \frac{a_1}{1+(j-4)} \right). \quad (6.7)$$

1381 The normalization is calculated and applied separately for each sub-sample of $t\bar{t}W^+$ and

1382 $t\bar{t}W^-$ in a N_{jets} bin for $4 \leq N_{\text{jets}} < 10$. Due to small contributions in the CRs, events

1383 with $N_{\text{jets}} < 4$ and $N_{\text{jets}} \geq 10$ are not normalized with this scheme. Instead, $N_{\text{jets}} < 4$

1384 events are fitted by propagating the normalization in the 4-jet bin without additional shape

1385 correction. The correction factor for $t\bar{t}W$ events with $N_{\text{jets}} \geq 10$ is obtained by summing

1386 up the overflow from $N_{\text{jets}} = 10$ to $N_{\text{jets}} = 12$, described as $\sum_{j'=10}^{12} \prod_{j=4}^{j'-1} \left(a_0 + \frac{a_1}{1+(j-4)} \right)$.

1387 Events with $N_{\text{jets}} \geq 13$ are negligible and are not included in the sum.

1388 The four regions, CR $t\bar{t}W^\pm$ and CR 1b(\pm), are constructed to fit $\text{NF}_{t\bar{t}W^\pm(N_{\text{jets}}=4)}$ and

1389 the scaling parameters $a_{0(1)}$, as well as validating the parameterization. Assuming the N_{jets}

1390 distribution of $t\bar{t}W$ is similar across bins of N_b -jets, a fitted N_{jets} distribution in CR 1b(\pm)

1391 can be used to describe the $t\bar{t}W$ parameterization at higher N_{jets} .

1392 Chapter 7. Systematic Uncertainties

1393 Physics analysis inherently incurs uncertainties in the form of statistical and systematic
1394 uncertainties, depending on the source. Statistical uncertainties occur in this analysis from
1395 sample size of collected data and simulated MC samples, and from the maximizing of the
1396 LH function. Systematic uncertainties depend on identifiable sources in the analysis i.e.
1397 from detector and reconstruction effects (experimental uncertainties) or theoretical modeling
1398 (theoretical uncertainties). Systematic uncertainties are represented as nuisance parameters
1399 (NP_x) in the profile LH fit. During the fit, systematic uncertainties with negligible impact
1400 on the final results can be pruned to simplify the statistical model and reduce computational
1401 complexity. This section outlines all uncertainties considered in this analysis.

1402 7.1 Experimental uncertainties

1403 7.1.1 Luminosity & pile-up reweighting

1404 The uncertainty on the integrated luminosity of the 2015-2018 Run 2 data set is 0.83%
1405 [87], obtained by the LUCID-2 detector [143] for the primary luminosity measurements and
1406 complemented by the ID and calorimeters. Pile-up was modeled in MC and calibrated
1407 to data through pile-up reweighting, resulting in a set of calibration SFs and associated
1408 uncertainties.

1409 7.1.2 Leptons

1410 In general, calibrating MC simulations to match performance in data incurs uncertainties
1411 associated obtaining the MC-to-data calibration SFs, which are in turn propagated to observ-

Table 7.1: Summary of the experimental systematic uncertainties considered in this analysis.

Systematic uncertainty	Components
Event	
Luminosity	1
Pile-up reweighting	1
Electrons	
Trigger efficiency	1
Reconstruction efficiency	1
Identification efficiency	1
Isolation efficiency	1
Energy scale	1
Energy resolution	1
Charge identification (ECIDS) efficiency	1
Muons	
Trigger efficiency	2
Track-to-vertex association efficiency	2
Reconstruction/identification efficiency	2
Low- p_T (< 15 GeV) reconstruction/identification efficiency	2
Isolation efficiency	2
Charge-independent momentum scale	1
Charge-dependent momentum scale	4
Energy resolution (CB)	1
Energy resolution (ID & MS)	2
Jets	
JES effective NP	15
JES η intercalibration	3
JES flavor composition	2
JES flavor response	1
JES pile-up	4
JES punch-through (FS/AF3)	2
JES non-closure	1
JES high- p_T single particle	1
JES b -jet response	1
JER effective NP	12
JER data/MC (FS/AF3)	2
JVT efficiency	1
GN2v01 b -tagging efficiency	85
GN2v01 c -tagging efficiency	56
GN2v01 light-tagging efficiency	42
E_T^{miss} track-based soft terms	
Transversal resolution	1
Longitudinal resolution	1
Longitudinal energy scale	1

ables in the analysis. The data-to-MC calibration of trigger, reconstruction, identification and isolation efficiencies for electrons and muons incur associated uncertainties, with separate systematic and statistical components for those related to muons. Similarly, electron energy scale, muon momentum scale and resolution are also subjected to calibration uncertainties estimated by re-simulating the events while varying the energy/momentun scale and resolution. Electron has an additional uncertainty related to ECIDS efficiency. Muon has additional uncertainties for charge-independent and charge-dependent momentum scale, as well as detector-specific track resolution. Systematic uncertainties for electron reconstruction, identification, isolation, ECIDS efficiencies and muon ID/MS energy resolution were not ready for the sample version used in this analysis, and are therefore not included.

7.1.3 Jets

Experimental uncertainties for jets are dominated by flavor tagging-related uncertainties, with subleading contributions from uncertainties related to JES [110], JER [109] and JVT [144] calibrations.

Jet energy scale

Uncertainties associated with JES are determined using data from LHC collisions along with MC simulated samples [110], decomposed into uncorrelated components:

- **Effective NPs:** 15 total p_T -dependent uncertainty components measured in situ, grouped based on their origin (2 detector-related, 4 modeling-related, 3 mixed, 6 statistical-related)
- **η intercalibration:** 6 total components (1 modeling-related, 4 non-closure and 1

1433 statistical-related) associated with the correction of the forward jets' ($0.8 \leq |\eta| < 4.5$)
1434 energy scale to that of the central jets ($|\eta| < 0.8$).

1435 • **Flavor composition & response:** 2 components for relative quark-gluon flavor com-
1436 positions in background and signal samples, and 2 components for responses to gluon-
1437 initiated versus quark-initiated jets.

1438 • **Pile-up subtraction:** 4 components, 2 for μ (`OffsetMu`) and N_{PV} (`OffsetNPV`) mod-
1439 eling, 1 for residual p_{T} -dependency (`PtTerm`) and 1 for topology dependence on the
1440 per-event p_{T} density modeling (`RhoTopology`).

1441 • **Punch-through effect treatment:** 2 terms for GSC punch-through jet response
1442 deviation between data and MC, one for each detector response simulation method
1443 (AF3 and FS).

1444 • **Non-closure:** 1 term applied to AF3 sample to account for the difference between
1445 AF3 and FS simulation.

1446 • **High- p_{T} single-particle response:** 1 term for the response to high- p_{T} jets from
1447 single-particle and test-beam measurements.

1448 • **b -jets response:** 1 term for the difference between b -jets and light-jets response.

1449 **Jet energy resolution**

1450 Measurements of JER were performed in bins of p_{T} and η , separately in data using in-
1451 situ techniques and in MC simulation using dijet events [109]. This analysis uses the full
1452 correlation JER uncertainty scheme provided for Run 2 analysis with 14 total components:

₁₄₅₃ 12 for effective NPs and 2 for difference between data and MC, separately for AF3 and FS

₁₄₅₄ [109].

₁₄₅₅ **Jet vertex tagging**

₁₄₅₆ The uncertainty associated with JVT is obtained by varying the JVT efficiency SFs

₁₄₅₇ within their uncertainty range [144]. This uncertainty accounts for remaining contamination

₁₄₅₈ from pile-up jets after applying pile-up suppression and MC generator choice.

₁₄₅₉ **Flavor tagging**

₁₄₆₀ Calibration SFs for b -tagging efficiencies and c -/light-jets mistagging rates are derived as

₁₄₆₁ a function of p_T for b -, c -, light-jets and PCBT score. The full set of flavor tagging-related

₁₄₆₂ uncertainties was reduced in dimensions by diagonalizing the uncertainty covariance matrix

₁₄₆₃ via eigendecomposition [113], resulting in a compact set of orthogonal NPs for this analysis:

₁₄₆₄ 85 for b -jets, 56 for c -jets and 42 for light-jets.

₁₄₆₅ **7.1.4 Missing transverse energy**

₁₄₆₆ Uncertainties on E_T^{miss} arise from possible mis-calibration of the soft-track component

₁₄₆₇ and are estimated using data-to-MC comparison of the p_T scale and resolution between

₁₄₆₈ the hard and soft E_T^{miss} components [118]. These uncertainties are represented by three

₁₄₆₉ independent terms: 1 for scale uncertainty and 2 for resolution uncertainty of the parallel

₁₄₇₀ and perpendicular components.

¹⁴⁷¹ 7.2 Modeling uncertainties

¹⁴⁷² 7.2.1 Signal and irreducible background uncertainties

¹⁴⁷³ The signal and background samples used are modeled using MC simulation. Most uncer-
¹⁴⁷⁴ tainties on simulation parameters (e.g. generator choice, PS model) are estimated by varying
¹⁴⁷⁵ the relevant parameters and comparing them with the nominal sample. Uncertainties in-
¹⁴⁷⁶ volving PDF in particular for most processes in the analysis are set to a flat 1% uncertainty.
¹⁴⁷⁷ Cross-section uncertainties were considered for all irreducible background except $t\bar{t}W$, which
¹⁴⁷⁸ is normalized in dedicated CRs following section 6.3.3. Extra uncertainties for the produc-
¹⁴⁷⁹ tion of four or more b -jets (additional b -jets) in association with $t\bar{t}X$ and HF jets were also
¹⁴⁸⁰ considered due to a lack of theoretical predictions or dedicated measurements, rendering
¹⁴⁸¹ MC modeling challenging. Uncertainties from missing higher-order QCD corrections in MC
¹⁴⁸² simulation are estimated by varying the renormalization scale μ_R and factorization scale μ_F
¹⁴⁸³ within seven different combinations

$$(\mu_R, \mu_F) = \{(0.5, 0.5), (0.5, 1), (1, 0.5), (1, 1), (1, 2), (2, 1), (2, 2)\}.$$

¹⁴⁸⁴ Process-specific uncertainty treatments are detailed below.

¹⁴⁸⁵ SM $t\bar{t}t\bar{t}$ background

¹⁴⁸⁶ The generator uncertainty for the SM $t\bar{t}t\bar{t}$ background was evaluated between a nominal
¹⁴⁸⁷ sample of MADGRAPH5_AMC@NLO and SHERPA. The parton shower uncertainty was
¹⁴⁸⁸ evaluated between PYTHIA8 and HERWIG. The cross-section uncertainty was estimated to

1489 be 20% computed from a prediction at NLO in QCD+EW [127].

1490 $t\bar{t}t$ background

1491 The cross-section uncertainty for $t\bar{t}t$ was estimated to be 30% computed from a prediction
1492 at NLO in QCD+EW [127]. Events with additional b -jets also incur a 50% uncertainty.

1493 $t\bar{t}W$, $t\bar{t}Z$, $t\bar{t}H$ backgrounds

1494 For $t\bar{t}W$, $t\bar{t}Z$ and $t\bar{t}H$ backgrounds, an uncertainty of 50% is assigned to events with one
1495 additional truth b -jets that did not originate from a top quark decay, and an added 50%
1496 uncertainty is assigned to events with two or more [145] additional b -jets. The generator
1497 uncertainty was estimated for $t\bar{t}Z$ using a MADGRAPH5_AMC@NLO nominal sample and
1498 a SHERPA sample, and for $t\bar{t}H$ using POWHEGBOX samples interfaced with PYTHIA8 (nom-
1499 inal) and HERWIG7. Cross-section uncertainties of 12% and 10% were applied to $t\bar{t}Z$ and
1500 $t\bar{t}H$ respectively [146]. No $t\bar{t}W$ cross-section or PDF uncertainty was considered since the
1501 normalizations and jet multiplicity spectrum for $t\bar{t}W$ are estimated using the data-driven
1502 method described in section 6.3.3.

1503 Other backgrounds

1504 Other backgrounds include processes with small overall contribution in the SR. The
1505 cross-section uncertainty for tZ and tWH is considered to be 30% [147, 148]. A conservative
1506 cross-section uncertainty of 50% is applied to $t\bar{t}VV$, VVV and VH . For VV , the cross-
1507 section uncertainty is dependent on jet multiplicity and is considered to be 20%/50%/60%
1508 for events with $\leq 3/4 \geq 5$ jets [149]. For VV , $t\bar{t}VV$, VVV and VH events with additional
1509 truth b -jets, an uncertainty of 50% is applied.

1510 7.2.2 Reducible background uncertainties

1511 Reducible backgrounds consist of $t\bar{t}/V + \text{HF}$ jets and single top events. Reducible back-
1512 ground has small contamination within the SR, thus uncertainties related to reducible back-
1513 ground have minor impact. Treatment for reducible background in this analysis largely
1514 follows Ref. [44], except for QmisID.

1515 Charge misidentification

1516 Uncertainties on the QmisID background originate from the charge flip rates obtained
1517 using the data-driven method described in section 6.3.2. Four sources of uncertainty were
1518 considered: statistical uncertainty from the maximum LLH estimation using Equation 6.2;
1519 uncertainty from choice of the Z -mass window and sidebands; non-closure uncertainty de-
1520 fined as the relative difference between the number of SS and OS events; and statistical
1521 uncertainty from the N_{jets} dependency correction SFs. The combined uncertainties from
1522 all four sources are calculated separately for each region involved in section 6.3.2, and are
1523 treated as correlated across all regions. Figure 7.1 shows the uncertainty calculated for SR.

1524 Internal (low γ^*) and material conversion

1525 The normalization for internal and material conversion backgrounds are free parameters
1526 in the fit, as a result the only uncertainties evaluated are from the shape of the distributions
1527 used in the template fit method (see section 6.3.1). The uncertainties on internal (material)
1528 conversion are estimated based on the difference between data and MC prediction in a region
1529 enriched in $Z + \gamma \rightarrow \mu^+\mu^- + e^+e^-$ events.

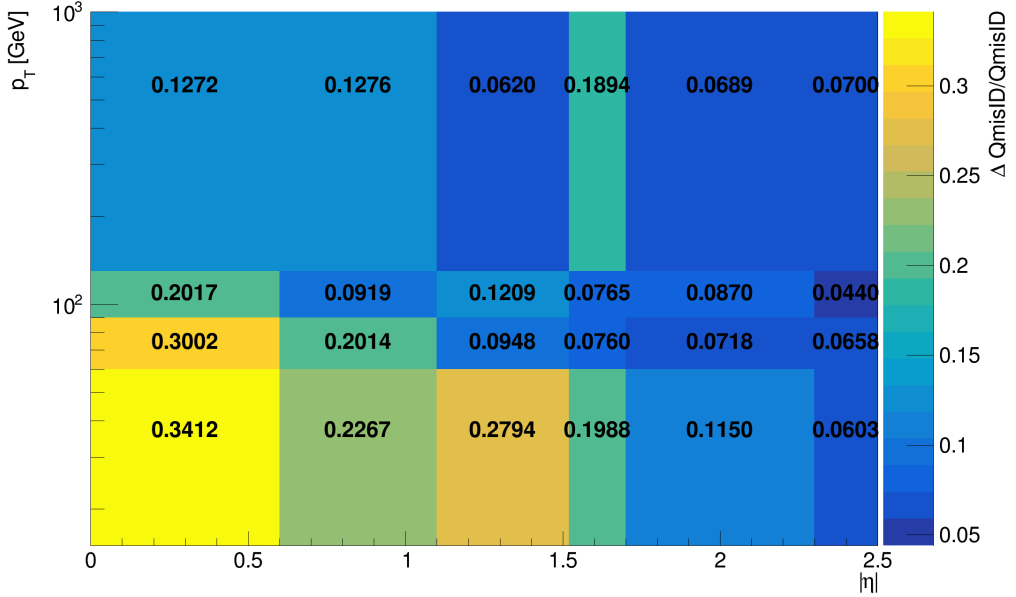


Figure 7.1: Combined QmisID uncertainty rate for SR in bins of $|\eta|$ and p_T .

1530 Heavy-flavor non-prompt lepton

1531 Similar to the conversion backgrounds, the uncertainties on non-prompt HF decays come
1532 from the shape of the distributions, and are estimated by comparing data and MC prediction
1533 between all regions in the analysis on a per bin basis. The events used are required to
1534 contain at least one *Loose* reconstructed lepton used in the region selection criteria detailed
1535 in Table 6.2 to maintain orthogonality with the SR.

1536 Light-flavor decays and other fake/non-prompt backgrounds

1537 A conservative normalization uncertainty of 100% is assigned for light-flavor non-prompt
1538 lepton background [138], and an ad-hoc normalization uncertainty of 30% is applied to all
1539 other fake and non-prompt backgrounds. The shape uncertainties for these backgrounds are
1540 negligible.

₁₅₄₁ **Chapter 8. Results**

₁₅₄₂ **8.1 Statistical interpretation**

₁₅₄₃ This section provides an overview of the statistical methods needed to interpret the
₁₅₄₄ collected and simulated data to estimate unknown physics parameters and determine com-
₁₅₄₅ patibility between data and the analysis hypothesis. For the BSM resonance search, the null
₁₅₄₆ hypothesis H_0 assumes only SM background contributions and none from any new BSM
₁₅₄₇ resonance in the data.

₁₅₄₈ **8.1.1 Profile likelihood fit**

₁₅₄₉ Given a set of observed data points $\mathbf{x} = [x_1, x_2, \dots]$ and unknown parameters $\boldsymbol{\theta} =$
₁₅₅₀ $[\theta_1, \theta_2, \dots, \theta_n]$, the maximum likelihood method aims to find an estimate $\hat{\boldsymbol{\theta}}$ that maximizes
₁₅₅₁ the joint probability function $f(\mathbf{x}, \boldsymbol{\theta})$, or in other words the set of parameters that gives the
₁₅₅₂ highest probability of observing the collected data points for a particular model. The func-
₁₅₅₃ tion to be maximized for this purpose is the log-likelihood (LLH) function $\ln \mathcal{L}(\mathbf{x}, \boldsymbol{\theta})$ where
₁₅₅₄ $\mathcal{L}(\mathbf{x}, \boldsymbol{\theta}) \equiv \prod_i f(x_i, \boldsymbol{\theta})$ is defined as the likelihood (LH) function. The LLH is maximized
₁₅₅₅ when $\partial/\partial\theta_i (\ln \mathcal{L}) = 0$ for each parameter θ_i .

₁₅₅₆ For an usual binned physics analysis, the above variables for the LH function \mathcal{L} can
₁₅₅₇ be expressed as nuisance parameters (NP) $\boldsymbol{\theta}$ and number of events for a model $N_i(\mu)$ for
₁₅₅₈ the i^{th} bin, where μ is the targeted parameter of interest (POI). In this analysis, N_i is
₁₅₅₉ assumed to follow a Poisson distribution and depends on the following quantities: the signal
₁₅₆₀ strength μ defined as the ratio of observed to expected cross sections $\sigma_{\text{obs}}/\sigma_{\text{exp}}$; nuisance
₁₅₆₁ parameters $\boldsymbol{\theta}$ which represents the effects of systematic uncertainties, implemented in the

1562 LH function as Gaussian constraints; and normalization factors (NFs) $\boldsymbol{\lambda}$ that control the
 1563 normalization of background components that do not have a well-known cross section. The
 1564 Poisson probability of observing exactly N_i events for an expected number of event n_i is

$$\mathcal{P}(N_i|n_i(\mu, \boldsymbol{\lambda})) = \frac{n_i^{N_i} e^{-n_i}}{N_i!}. \quad (8.1)$$

1565 The expected Poisson event number in a bin i can be parameterized as

$$n_i = \mu s_i(\boldsymbol{\theta}) + \sum_j \lambda_j b_{ij}(\boldsymbol{\theta}), \quad (8.2)$$

1566 where s_i is the number of signal events in bin i of every region, and b_{ij} is the number of
 1567 events for a certain background source index j in bin i . The LH function in this analysis
 1568 can be written as

$$\mathcal{L}(\mathbf{N}|\mu, \boldsymbol{\theta}, \boldsymbol{\lambda}) = \left(\prod_i \mathcal{P}(N_i|n_i) \right) \cdot \prod_k \mathcal{G}(\theta_k), \quad (8.3)$$

1569 where $\mathcal{G}(\theta_k)$ is the Gaussian constraint for a NP k . The signal significance μ and NFs $\boldsymbol{\lambda}$ are
 1570 left unconstrained and are fitted simultaneously in the profile LH fit. Define the profile LH
 1571 ratio [150] as

$$\lambda(\mu) = \frac{\mathcal{L}(\mu, \hat{\boldsymbol{\theta}}_\mu, \hat{\boldsymbol{\lambda}}_\mu)}{\mathcal{L}(\hat{\mu}, \hat{\boldsymbol{\theta}}, \hat{\boldsymbol{\lambda}})}, \quad (8.4)$$

1572 where $\hat{\mu}$, $\hat{\boldsymbol{\theta}}$ and $\hat{\boldsymbol{\lambda}}$ are parameter values that optimally maximizes the LH function, and $\hat{\boldsymbol{\theta}}_\mu$,
 1573 $\hat{\boldsymbol{\lambda}}_\mu$ are NP and NF values respectively that maximize the LH function for a given signal
 1574 strength μ . Using Neyman-Pearson lemma [151], the optimal test statistic for hypothesis
 1575 testing is

$$q_\mu \equiv -2 \ln \lambda(\mu), \quad (8.5)$$

1576 where $q_\mu = 0$ or $\lambda(\mu) = 1$ corresponds to perfect agreement between the optimal parameter
 1577 $\hat{\mu}$ obtained from data and the hypothesized value μ . From Wilks' theorem [152], the test
 1578 statistic q_μ approaches a χ^2 distribution and can be evaluated as $q_\mu = (\mu - \hat{\mu})^2 / \sigma_\mu^2$.

1579 When evaluating against the background-only hypothesis ($\mu = 0$), it can be assumed
 1580 that the number of events observed under the signal hypothesis is higher than that of the
 1581 background-only hypothesis, or $\mu \geq 0$ according to Equation 8.2. This leads to a corre-
 1582 sponding lower bound on the test statistic

$$q_0 = \begin{cases} -2 \ln \lambda(0), & \text{if } \hat{\mu} \geq 0, \\ 0, & \text{if } \hat{\mu} < 0. \end{cases} \quad (8.6)$$

1583 ***p*-value**

1584 To quantify the incompatibility between the observed data and the background-only hy-
 1585 pothesis, the *p*-value is defined as $p = P(q_\mu \geq q_{\mu, \text{obs}} | H_0)$ or in other words, the probability
 1586 of observing data with a test statistic q_μ under the null hypothesis H_0 that is less compat-
 1587 ible with H_0 than the actual observed data with test statistic $q_{\mu, \text{obs}}$. The *p*-value can be
 1588 expressed in terms of q_μ as

$$p_\mu = \int_{q_{\mu, \text{obs}}}^{\infty} f(q_\mu | \mu) dq_\mu, \quad (8.7)$$

1589 where $f(q_\mu | \mu) dq_\mu$ is the conditional probability density function of q_μ given μ .

1590 In some cases, it is more convenient to evaluate compatibility using the *Z*-value, defined
 1591 as the number of standard deviations between the observed data and the mean in a Gaussian

1592 distribution. The p -value can be converted to Z -value via the relation

$$Z = \Phi^{-1}(1 - p), \quad (8.8)$$

1593 where Φ is the quantile of the standard Gaussian. Rejecting the signal hypothesis usually
1594 requires a 95% confidence level (CL) which corresponds to a p -value of 0.05 or a Z -value of
1595 1.64, while rejecting the background-only hypothesis generally requires a Z -value of 5 or a
1596 p -value of 2.84×10^{-7} .

1597 8.1.2 Exclusion limit

1598 If the signal hypothesis is rejected, the exclusion upper limits can still be computed at
1599 a certain CL (usually 95%) to establish the maximum value of μ that is not excluded by
1600 the observed data. The exclusion limits are calculated based on the CL_s method [153, 154]
1601 under which the test statistic is defined as $q_\mu = -2 \ln \frac{\mathcal{L}_{s+b}}{\mathcal{L}_b}$ with \mathcal{L}_{s+b} being the LH function
1602 for the signal and background hypothesis ($\mu > 0$) and \mathcal{L}_b being the LH function for the
1603 background-only hypothesis ($\mu = 0$). The p -value for both hypotheses can then be expressed
1604 as

$$\begin{aligned} p_{s+b} &= P(q \geq q_{\text{obs}} | s + b) = \int_{q_{\text{obs}}}^{\infty} f(q | s + b) dq \\ p_b &= P(q \geq q_{\text{obs}} | b) = \int_{-\infty}^{q_{\text{obs}}} f(q | b) dq. \end{aligned} \quad (8.9)$$

1605 The signal hypothesis is excluded for a CL α when the following condition is satisfied

$$\text{CL}_s \equiv \frac{p_{s+b}}{p_b} \geq 1 - \alpha. \quad (8.10)$$

₁₆₀₆ The value of μ such that the signal hypothesis leads to $\text{CL}_s = 1 - \alpha = 0.05$ is then the
₁₆₀₇ exclusio upper limit at a 95% CL.

₁₆₀₈ 8.2 Fit results

₁₆₀₉ The signal strength μ , background NFs, $t\bar{t}W$ scaling factors and uncertainty NPs are
₁₆₁₀ simultaneously fitted using a binned profile LLH fit under the background-only hypothesis
₁₆₁₁ to the H_T distribution in the SR and to corresponding distributions shown in Table 6.2 for
₁₆₁₂ CRs.

₁₆₁₃ Before fitting to real data (unblinded fit), the fit was first performed in both the SR
₁₆₁₄ and CRs using Asimov pseudo-datasets, in which the simulated data match exactly to MC
₁₆₁₅ prediction with nominal μ set to 0. This is done for the purpose of optimizing object selection
₁₆₁₆ criteria and region definition, refining background estimation techniques and testing the
₁₆₁₇ statistical interpretation model for signal extraction described in section 8.1. The fit is then
₁₆₁₈ performed with Asimov data in the SR and real data in CRs to validate background modeling,
₁₆₁₉ estimate sensitivity and assess the influence of statistical effects on fitted parameters. Finally,
₁₆₂₀ the fully unblinded fit is performed with real data in all regions.

₁₆₂₁ The unblinded fit results are presented below. No significant excess over SM predictions
₁₆₂₂ is observed, and the fitted signal strength μ is compatible with zero for all Z' mass points.
₁₆₂₃ Figure 8.1 shows the observed and expected upper limits at 95% confidence level on the
₁₆₂₄ cross-section of $pp \rightarrow t\bar{t}Z'$ production times the branching ratio of $Z' \rightarrow t\bar{t}$ as a function of
₁₆₂₅ the Z' resonance mass. The exclusion limits range from 7.9 fb to 9.44 fb depending on $m_{Z'}$.

₁₆₂₆ The background modeling is evaluated under the background-only hypothesis. The fitted
₁₆₂₇ background NFs are shown in Table 8.1 and are consistent with their nominal values within

one standard deviation, or two standard deviations in the case of $\text{NF}_{\text{HF } e}$ and $\text{NF}_{t\bar{t}W^+(4j)}$.
 Figure 8.2 shows good agreement between data and post-fit background distributions in
 non-prompt background CRs and $t\bar{t}W$ CRs. The pre-fit and post-fit background yields
 are shown in Table 8.2. **Discuss differences between pre and post-fit yields. Which one
 increased/decreased? Why, NFs/NPs? Consistent with data within 1-2 stdev?**

Table 8.1: Normalization factors for backgrounds with dedicated CRs, obtained from a simultaneous fit in all CRs and SR under the background-only hypothesis. The nominal pre-fit value is 1 for all NFs and 0 for the scaling factors a_0 and a_1 . Uncertainties shown include both statistical and systematic uncertainties.

Parameter	$\text{NF}_{\text{HF } e}$	$\text{NF}_{\text{HF } \mu}$	$\text{NF}_{\text{Mat. Conv.}}$	$\text{NF}_{\text{Low } m_{\gamma^*}}$	a_0	a_1	$\text{NF}_{t\bar{t}W^+(4j)}$	$\text{NF}_{t\bar{t}W^-(4j)}$
Fit value	$0.68^{+0.23}_{-0.22}$	$0.97^{+0.17}_{-0.16}$	$0.97^{+0.31}_{-0.28}$	$0.97^{+0.23}_{-0.20}$	$0.39^{+0.11}_{-0.11}$	$0.42^{+0.25}_{-0.24}$	$1.21^{+0.18}_{-0.18}$	$1.10^{+0.26}_{-0.26}$

Table 8.3 shows the impact of various sources of uncertainty grouped by their corresponding category on the signal strength. **Largest sources of uncertainty? Why?**

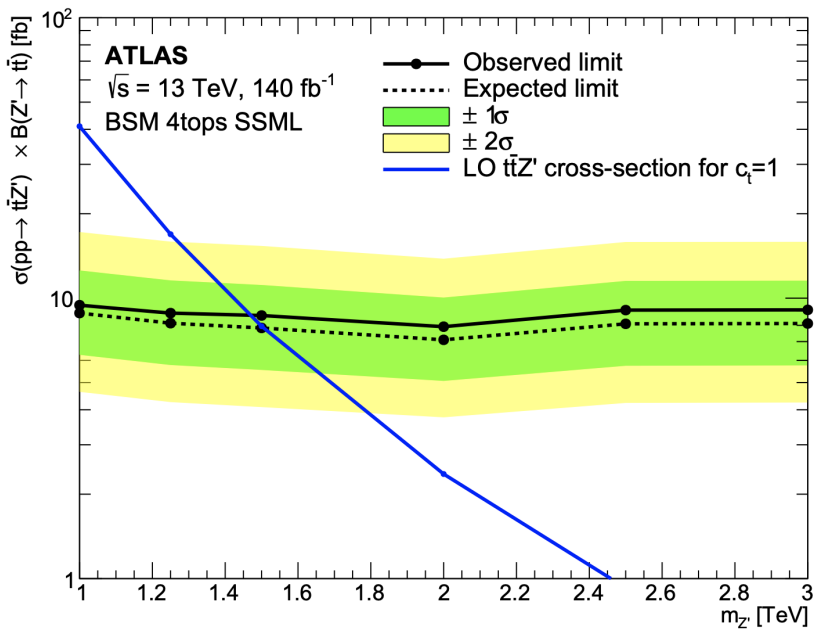


Figure 8.1: Observed (solid line) and expected (dotted line) upper limits as a function of the Z' mass at 95% CL on the cross-section of $pp \rightarrow t\bar{t}Z'$ production times the $Z' \rightarrow t\bar{t}$ branching ratio. The region above the observed limit is excluded. The solid blue line represents the theoretical signal cross-section with $c_t = 1$ at LO in QCD [71]. The green and yellow bands represent the 68% ($\pm\sigma$) and 95% ($\pm 2\sigma$) confidence intervals respectively.

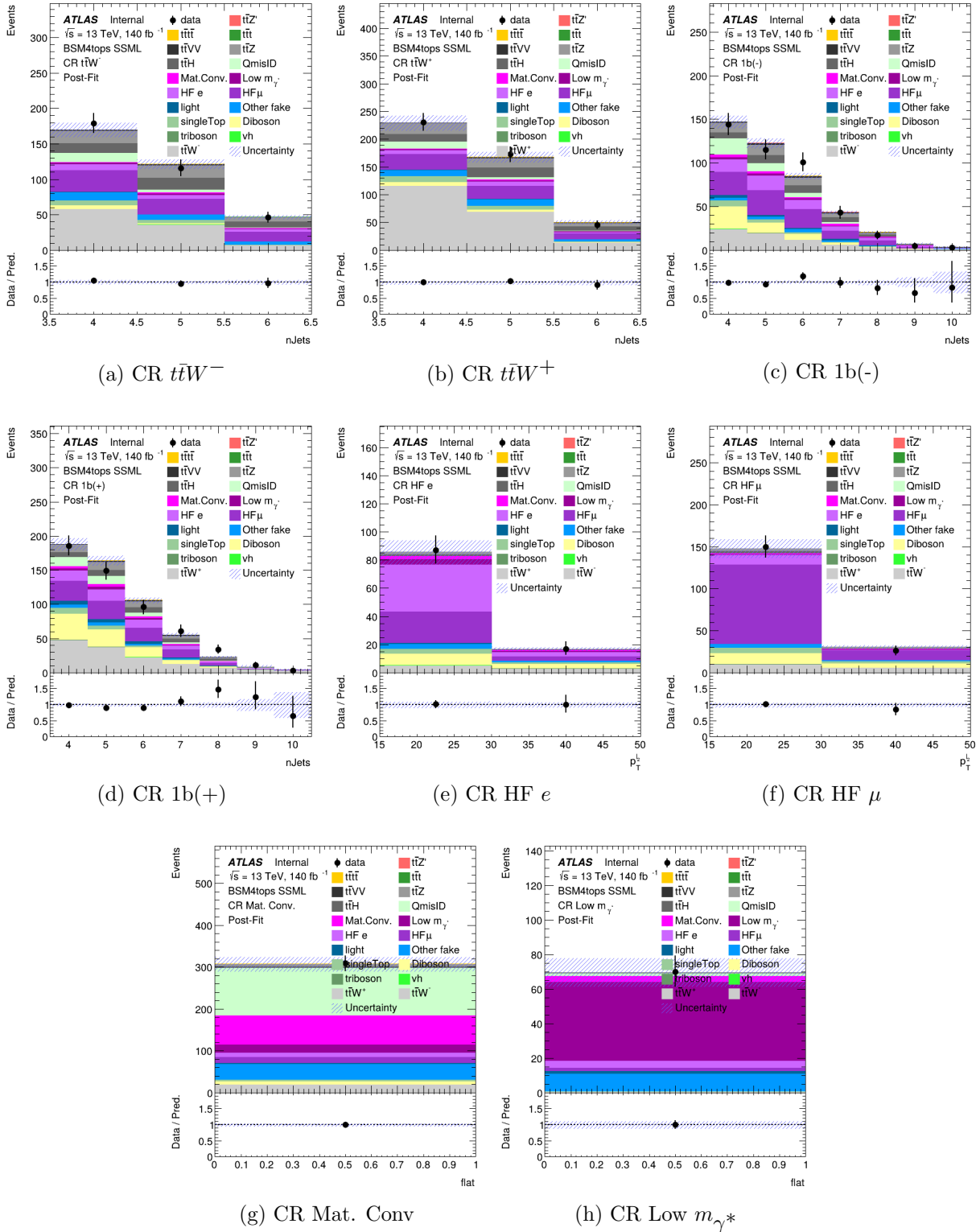


Figure 8.2: Comparison between data and post-fit prediction for the discriminant observable in each non-prompt and $t\bar{t}W$ background CR. The fit is performed simultaneously in all CRs and SR under the background-only hypothesis. The lower panel shows the ratio between data and post-fit predictions. The shaded band represents the total uncertainty on the fit.

Table 8.2: Pre-fit and post-fit background yields in the inclusive SR. The number of data events and pre-fit estimate signal yields are also shown. Background yields shown are obtained from the fit using the $t\bar{t}Z'$ signal sample with $m_{Z'} = 2$ TeV. Total yield uncertainty differs from the quadrature sum of constituent uncertainties due to correlation and anticorrelation effects.

Process	Pre-fit	Post-fit
Background		
$t\bar{t}t\bar{t}$	42.35 ± 5.45	46.91 ± 5.19
$t\bar{t}W^+$	97.38 ± 0.71	103.93 ± 15.91
$t\bar{t}W^-$	56.92 ± 0.42	55.27 ± 11.14
$t\bar{t}Z$	78.02 ± 14.12	75.57 ± 11.13
$t\bar{t}H$	81.00 ± 7.10	82.90 ± 7.30
$t\bar{t}t$	3.33 ± 0.59	3.37 ± 0.60
Single-top (tq , tZq , tWZ , etc.)	13.38 ± 2.87	12.69 ± 2.86
$t\bar{t}VV/t\bar{t}VH/t\bar{t}HH$	17.07 ± 4.66	16.44 ± 4.64
Charge misidentification	40.31 ± 0.32	40.33 ± 0.32
$VV/VVV/VH$	10.01 ± 4.76	6.69 ± 2.75
Mat. Conv.	26.20 ± 0.91	25.76 ± 6.06
Low m_{γ^*}	26.14 ± 0.66	25.62 ± 4.23
HF e	21.99 ± 1.45	15.42 ± 3.70
HF μ	31.33 ± 3.47	31.53 ± 5.06
Light-flavor decays	13.47 ± 0.53	13.54 ± 0.53
Other fake & non-prompt	24.90 ± 2.26	26.00 ± 1.96
Total background	593.90 ± 18.79	576.53 ± 19.86
Signal $t\bar{t}Z' \rightarrow t\bar{t}t\bar{t}$		
$m_{Z'} = 1$ TeV	52.83 ± 1.41	-
$m_{Z'} = 1.25$ TeV	52.94 ± 1.35	-
$m_{Z'} = 1.5$ TeV	53.07 ± 1.47	-
$m_{Z'} = 2$ TeV	52.49 ± 1.43	-
$m_{Z'} = 2.5$ TeV	53.07 ± 1.47	-
$m_{Z'} = 3$ TeV	52.45 ± 1.50	-
Data	604	

Table 8.3: Post-fit impact of uncertainty sources on the signal strength μ , grouped by categories. Values shown are obtained from the fit using the $t\bar{t}Z'$ signal sample with $m_{Z'} = 2$ TeV. Impact on μ is evaluated for each uncertainty category by re-fitting with the corresponding set of NPs fixed to their best-fit values. Total uncertainty differs from the quadrature sum of constituent uncertainties due to correlation between NPs in the fit.

Uncertainty source	$\Delta\mu$	
Signal modeling		
$t\bar{t}Z'$	+0.00	-0.00
Background modeling		
$t\bar{t}\bar{t}$	+0.15	-0.13
$t\bar{t}W$	+0.04	-0.03
$t\bar{t}Z$	+0.02	-0.02
$t\bar{t}H$	+0.02	-0.02
Non-prompt leptons	+0.00	-0.00
Other backgrounds	+0.02	-0.02
Instrumental		
Luminosity	+0.00	-0.00
Jet uncertainties	+0.04	-0.04
Jet flavor tagging (b -jets)	+0.04	-0.04
Jet flavor tagging (c -jets)	+0.01	-0.01
Jet flavor tagging (light-jets)	+0.02	-0.01
MC simulation sample size	+0.01	-0.01
Other experimental uncertainties	+0.01	-0.01
Total systematic uncertainty	+0.15	-0.17
Statistical		
$t\bar{t}W$ NFs and scaling factors	+0.01	-0.01
Non-prompt lepton NFs (HF, Mat. Conv., Low m_{γ^*})	+0.00	-0.00
Total statistical uncertainty	+0.25	-0.23
Total uncertainty	+0.29	-0.29

1635 Chapter 9. Summary

1636 References

- 1637 [1] J. Schwinger. *On Quantum-Electrodynamics and the Magnetic Moment of the Elec-*
tron. *Phys. Rev.* **73** (4 1948), pp. 416–417 (cit. on p. 1).
- 1638 [2] R. P. Feynman. *Space-Time Approach to Quantum Electrodynamics.* *Phys. Rev.* **76**
1639 (6 1949), pp. 769–789 (cit. on p. 1).
- 1640 [3] S. Tomonaga. *On a relativistically invariant formulation of the quantum theory of*
wave fields. *Prog. Theor. Phys.* **1** (1946), pp. 27–42 (cit. on p. 1).
- 1641 [4] E. Fermi. *An attempt of a theory of beta radiation. I.* *Nuclear Physics B* **4** (1967).
1642 Translated from the original 1934 German article by C. P. Enz and C. H. Beck, pp. 1–
1643 27 (cit. on p. 1).
- 1644 [5] D. J. Griffiths. *Introduction to Elementary Particles.* 2nd. Weinheim: Wiley-VCH,
1645 2008. ISBN: 978-3-527-40601-2 (cit. on p. 1).
- 1646 [6] C. Yang and R. Mills. *Conservation of Isotopic Spin and Isotopic Gauge Invariance.*
1647 *Phys. Rev.* **96** (1 1954), pp. 191–195 (cit. on pp. 1, 10).
- 1648 [7] A. Milsted and T. J. Osborne. *Quantum Yang-Mills theory: An overview of a program.*
1649 *Phys. Rev. D* **98** (1 2018), p. 014505 (cit. on pp. 1, 10).
- 1650
- 1651

- 1652 [8] S. L. Glashow. *Partial-symmetries of weak interactions*. Nuclear Physics 22.4 (1961),
1653 pp. 579–588. ISSN: 0029-5582 (cit. on p. 1).
- 1654 [9] D. J. Gross and F. Wilczek. *Ultraviolet Behavior of Non-Abelian Gauge Theories*.
1655 Phys. Rev. Lett. 30 (26 1973), pp. 1343–1346 (cit. on p. 1).
- 1656 [10] H. D. Politzer. *Reliable Perturbative Results for Strong Interactions?* Phys. Rev. Lett.
1657 30 (26 1973), pp. 1346–1349 (cit. on p. 1).
- 1658 [11] P. Higgs. *Broken symmetries and the masses of gauge bosons*. Phys. Rev. Lett. 13 (16
1659 1964), pp. 508–509 (cit. on pp. 1, 14).
- 1660 [12] P. Higgs. *Broken symmetries, massless particles and gauge fields*. Physics Letters 12.2
1661 (1964), pp. 132–133. ISSN: 0031-9163 (cit. on pp. 1, 14).
- 1662 [13] F. Englert and R. Brout. *Broken Symmetry and the Mass of Gauge Vector Mesons*.
1663 Phys. Rev. Lett. 13 (9 1964), pp. 321–323 (cit. on pp. 1, 14).
- 1664 [14] S. Weinberg. *The making of the Standard Model*. The European Physical Journal C
1665 34.1 (May 2004), 513. ISSN: 1434-6052. arXiv: hep-ph/0401010 [hep-ph] (cit. on
1666 p. 2).
- 1667 [15] D. P. Barber et al. *Discovery of Three-Jet Events and a Test of Quantum Chromody-
1668 namics at PETRA*. Phys. Rev. Lett. 43 (12 1979), pp. 830–833 (cit. on p. 2).
- 1669 [16] G. Arnison et al. *Experimental Observation of Isolated Large Transverse Energy Elec-
1670 trons with Associated Missing Energy at $\sqrt{s} = 540 \text{ GeV}$* . Phys. Lett. B 122 (1983),
1671 pp. 103–116 (cit. on p. 2).

- 1672 [17] G. Arnison and others. *Experimental Observation of Lepton Pairs of Invariant Mass*
1673 *Around $95 \text{ GeV}/c^2$ at the CERN SPS Collider.* *Phys. Lett. B* **126** (1983), pp. 398–410
1674 (cit. on p. 2).
- 1675 [18] CDF Collaboration. *Observation of Top Quark Production in $\bar{p}p$ Collisions with the*
1676 *Collider Detector at Fermilab.* *Phys. Rev. Lett.* **74** (14 1995), pp. 2626–2631 (cit. on
1677 p. 2).
- 1678 [19] DØ Collaboration. *Observation of the Top Quark.* *Phys. Rev. Lett.* **74** (14 1995),
1679 pp. 2632–2637 (cit. on p. 2).
- 1680 [20] ATLAS Collaboration. *Observation of a new particle in the search for the Standard*
1681 *Model Higgs boson with the ATLAS detector at the LHC.* *Phys. Lett. B* **716** (2012),
1682 p. 1. arXiv: [1207.7214 \[hep-ex\]](#) (cit. on pp. 2, 14).
- 1683 [21] CMS Collaboration. *Observation of a new boson at a mass of 125 GeV with the CMS*
1684 *experiment at the LHC.* *Phys. Lett. B* **716** (2012), p. 30. arXiv: [1207.7235 \[hep-ex\]](#)
1685 (cit. on pp. 2, 14).
- 1686 [22] S. Navas et al. *Review of particle physics.* *Phys. Rev. D* **110.3** (2024), p. 030001 (cit.
1687 on pp. 2, 8).
- 1688 [23] Y. Fukuda et al. *Evidence for Oscillation of Atmospheric Neutrinos.* *Phys. Rev. Lett.*
1689 **81** (8 1998), pp. 1562–1567 (cit. on p. 2).
- 1690 [24] M. Cristinziani and M. Mulders. *Top-quark physics at the Large Hadron Collider.*
1691 *Journal of Physics G: Nuclear and Particle Physics* **44.6** (2017), p. 063001. arXiv:
1692 [1606.00327 \[hep-ex\]](#) (cit. on pp. 2, 8).

- 1693 [25] ATLAS and CMS Collaborations. *Combination of inclusive top-quark pair production*
1694 *cross-section measurements using ATLAS and CMS data at $\sqrt{s} = 7$ and 8 TeV.* *JHEP*
1695 **07** (2023), p. 213. arXiv: [2205.13830 \[hep-ex\]](#) (cit. on p. 3).
- 1696 [26] C. Degrande, J.-M. Grard, C. Grojean, F. Maltoni, and G. Servant. *Non-resonant new*
1697 *physics in top pair production at hadron colliders.* *Journal of High Energy Physics*
1698 **2011.3** (Mar. 2011). ISSN: 1029-8479. arXiv: [1010.6304 \[hep-ph\]](#) (cit. on p. 3).
- 1699 [27] ATLAS Collaboration. *The ATLAS Experiment at the CERN Large Hadron Collider.*
1700 *JINST* **3** (2008), S08003 (cit. on pp. 3, 22, 25, 26, 28–32).
- 1701 [28] ATLAS Collaboration. *Search for top-philic heavy resonances in pp collisions at $\sqrt{s} =$*
- 1702 *13 TeV with the ATLAS detector.* *Eur. Phys. J. C* **84** (2024), p. 157. arXiv: [2304.01678 \[hep-ex\]](#) (cit. on pp. 3, 4, 17, 20).
- 1703 [29] H. P. Nilles. *Supersymmetry, Supergravity and Particle Physics.* *Phys. Rept.* **110**
1704 (1984), pp. 1–162 (cit. on p. 3).
- 1705 [30] G. R. Farrar and P. Fayet. *Phenomenology of the Production, Decay, and Detection*
1706 *of New Hadronic States Associated with Supersymmetry.* *Phys. Lett. B* **76** (1978),
1707 pp. 575–579 (cit. on p. 3).
- 1708 [31] T. Plehn and T. M. P. Tait. *Seeking sgluons.* *Journal of Physics G: Nuclear and*
1709 *Particle Physics* **36.7** (2009), p. 075001. arXiv: [0810.3919 \[hep-ph\]](#) (cit. on p. 3).
- 1710 [32] S. Calvet, B. Fuks, P. Gris, and L. Valry. *Searching for sgluons in multitop events*
1711 *at a center-of-mass energy of 8 TeV.* *Journal of High Energy Physics* **2013.4** (Apr.
1712 2013). ISSN: 1029-8479. arXiv: [1212.3360 \[hep-ph\]](#) (cit. on p. 3).
- 1713

- 1714 [33] A. Pomarol and J. Serra. *Top quark compositeness: Feasibility and implications*. Phys-
1715 ical Review D 78.7 (Oct. 2008). ISSN: 1550-2368. arXiv: 0806.3247 [hep-ph] (cit. on
1716 p. 3).
- 1717 [34] K. Kumar, T. M. Tait, and R. Vega-Morales. *Manifestations of top compositeness at*
1718 *colliders*. Journal of High Energy Physics 2009.05 (May 2009), 022022. ISSN: 1029-
1719 8479. arXiv: 0901.3808 [hep-ph] (cit. on p. 3).
- 1720 [35] G. Banelli, E. Salvioni, J. Serra, T. Theil, and A. Weiler. *The present and future of*
1721 *four top operators*. Journal of High Energy Physics 2021.2 (Feb. 2021). ISSN: 1029-
1722 8479. arXiv: 2010.05915 [hep-ph] (cit. on p. 3).
- 1723 [36] R. Aoude, H. El Faham, F. Maltoni, and E. Vryonidou. *Complete SMEFT predictions*
1724 *for four top quark production at hadron colliders*. Journal of High Energy Physics
1725 2022.10 (Oct. 2022). ISSN: 1029-8479. arXiv: 2208.04962 [hep-ph] (cit. on p. 3).
- 1726 [37] C. Zhang. *Constraining qqtt operators from four-top production: a case for enhanced*
1727 *EFT sensitivity*. Chinese Physics C 42.2 (Feb. 2018), p. 023104. ISSN: 1674-1137.
1728 arXiv: 1708.05928 [hep-ph] (cit. on p. 3).
- 1729 [38] L. Darmé, B. Fuks, and F. Maltoni. *Topophilic heavy resonances in four-top final*
1730 *states and their EFT interpretation*. Journal of High Energy Physics 2021.9 (Sept.
1731 2021). ISSN: 1029-8479. arXiv: 2104.09512 [hep-ph] (cit. on pp. 3, 17).
- 1732 [39] N. Craig, F. D’Eramo, P. Draper, S. Thomas, and H. Zhang. *The Hunt for the Rest*
1733 *of the Higgs Bosons*. JHEP 06 (2015), p. 137. arXiv: 1504.04630 [hep-ph] (cit. on
1734 pp. 3, 17, 19).

- 1735 [40] N. Craig, J. Hajer, Y.-Y. Li, T. Liu, and H. Zhang. *Heavy Higgs bosons at low $\tan \beta$:
1736 from the LHC to 100 TeV*. *Journal of High Energy Physics* 2017.1 (Jan. 2017). ISSN:
1737 1029-8479. arXiv: [1605.08744 \[hep-ph\]](#) (cit. on pp. 3, 17, 19).
- 1738 [41] G. C. Branco et al. *Theory and phenomenology of two-Higgs-doublet models*. *Phys.
1739 Rept.* 516 (2012), pp. 1–102. arXiv: [1106.0034 \[hep-ph\]](#) (cit. on pp. 3, 17, 19).
- 1740 [42] S. Gori, I.-W. Kim, N. R. Shah, and K. M. Zurek. *Closing the wedge: Search strategies
1741 for extended Higgs sectors with heavy flavor final states*. *Phys. Rev. D* 93 (7 2016),
1742 p. 075038 (cit. on pp. 3, 17, 19).
- 1743 [43] P. S. B. Dev and A. Pilaftsis. *Maximally symmetric two Higgs doublet model with
1744 natural Standard Model alignment*. *Journal of High Energy Physics* 2014.12 (Dec.
1745 2014), p. 024. arXiv: [1408.3405 \[hep-ph\]](#) (cit. on pp. 3, 17, 19).
- 1746 [44] ATLAS Collaboration. *Observation of four-top-quark production in the multilepton
1747 final state with the ATLAS detector*. *Eur. Phys. J. C* 83 (2023), p. 496. arXiv: [2303.
1748 15061 \[hep-ex\]](#) (cit. on pp. 3, 4, 17, 50, 62, 68, 77).
- 1749 [45] N. Greiner, K. Kong, J.-C. Park, S. C. Park, and J.-C. Winter. *Model-independent
1750 production of a topophilic resonance at the LHC*. *Journal of High Energy Physics*
1751 2015.4 (2015), p. 29. ISSN: 1029-8479. arXiv: [1410.6099 \[hep-ph\]](#) (cit. on pp. 3, 17–
1752 20).
- 1753 [46] ATLAS Collaboration. *Evidence for $t\bar{t}t\bar{t}$ production in the multilepton final state in
1754 proton–proton collisions at $\sqrt{s} = 13\text{TeV}$ with the ATLAS detector*. *Eur. Phys. J. C*
1755 80 (2020), p. 1085. arXiv: [2007.14858 \[hep-ex\]](#) (cit. on pp. 4, 67).
- 1756 [47] D. H. Perkins. *Introduction to High Energy Physics*. 4th. Cambridge, UK: Cambridge
1757 University Press, Apr. 2000. ISBN: 9780521621960 (cit. on p. 5).

- 1758 [48] C. Burgard and D. Galbraith. *Standard Model of Physics*. URL: <https://texample.net/model-physics/> (visited on 06/02/2025) (cit. on p. 6).
- 1759
- 1760 [49] H. Georgi. *Lie Algebras in Particle Physics: from Isospin to Unified Theories*. 2nd.
- 1761 CRC Press, 2000. ISBN: 9780429499210 (cit. on pp. 7, 10).
- 1762 [50] ATLAS and CMS Collaborations. *Combination of Measurements of the Top Quark*
- 1763 *Mass from Data Collected by the ATLAS and CMS Experiments at $\sqrt{s} = 7$ and 8 TeV*.
- 1764 *Phys. Rev. Lett.* **132** (2023), p. 261902. arXiv: [2402.08713 \[hep-ex\]](https://arxiv.org/abs/2402.08713) (cit. on p. 8).
- 1765 [51] H. de la Torre and T. Farooque. *Looking beyond the Standard Model with Third Gen-*
- 1766 *eration Quarks at the LHC*. *Symmetry* **14**.3 (2022), p. 444 (cit. on p. 8).
- 1767 [52] Q.-H. Cao, J.-N. Fu, Y. Liu, X.-H. Wang, and R. Zhang. *Probing Top-philic New*
- 1768 *Physics via Four-Top-Quark Production*. *Chinese Physics C* **45**.9 (2021), p. 093107.
- 1769 arXiv: [2105.03372 \[hep-ph\]](https://arxiv.org/abs/2105.03372) (cit. on p. 8).
- 1770 [53] H. Beauchesne et al. *A case study about BSM vector resonances with direct couplings*
- 1771 *to the third quark generation*. *European Physical Journal C* **80**.5 (2020), p. 485. arXiv:
- 1772 [1908.11619 \[hep-ph\]](https://arxiv.org/abs/1908.11619) (cit. on p. 8).
- 1773 [54] F. Maltoni, D. Pagani, and S. Tentori. *Top-quark pair production as a probe of light*
- 1774 *top-philic scalars and anomalous Higgs interactions*. *Journal of High Energy Physics*
- 1775 **2024**.9 (Sept. 2024), p. 098. arXiv: [2406.06694 \[hep-ph\]](https://arxiv.org/abs/2406.06694) (cit. on p. 8).
- 1776 [55] CMS Collaboration. *Search for $t\bar{t}H$ production in the $H \rightarrow b\bar{b}$ decay channel with*
- 1777 *leptonic $t\bar{t}$ decays in proton–proton collisions at $\sqrt{s} = 13$ TeV*. *JHEP* **03** (2019),
- 1778 p. 026. arXiv: [1804.03682 \[hep-ex\]](https://arxiv.org/abs/1804.03682) (cit. on p. 8).

- 1779 [56] Y. Grossman and Y. Nir. *The Standard Model: From Fundamental Symmetries to Ex-*
1780 *perimental Tests*. See Chapter 8.2. Cambridge University Press, 2023. ISBN: 9781009320378
1781 (cit. on p. 9).
- 1782 [57] M. E. Peskin and D. V. Schroeder. *An Introduction to Quantum Field Theory*. 1st.
1783 Reading, MA, USA: AddisonWesley, 1995. ISBN: 978-0-201-50397-5 (cit. on p. 9).
- 1784 [58] D. J. Gross. *The role of symmetry in fundamental physics*. Proceedings of the National
1785 Academy of Sciences of the United States of America 93.25 (Dec. 1996), pp. 14256–
1786 14259 (cit. on p. 9).
- 1787 [59] M. Bañados and I. Reyes. *A short review on Noethers theorems, gauge symmetries*
1788 *and boundary terms*. International Journal of Modern Physics D 25.10 (Aug. 2016),
1789 p. 1630021. ISSN: 1793-6594. arXiv: 1601.03616 [hep-th] (cit. on p. 9).
- 1790 [60] A. Pich. *The Standard Model of electroweak interactions. 2004 European School of*
1791 *High-Energy Physics*. Feb. 2005, pp. 1–48. arXiv: hep-ph/0502010 [hep-ex] (cit. on
1792 pp. 11–13).
- 1793 [61] P. Dev and A. Pilaftsis. *High-temperature electroweak symmetry non-restoration from*
1794 *new fermions and implications for baryogenesis*. Journal of High Energy Physics
1795 2020.9 (Sept. 2020), p. 012. arXiv: 2002.05174 [hep-ph] (cit. on p. 13).
- 1796 [62] J. Riebesell. *Higgs Potential*. URL: <https://tikz.net/higgs-potential/> (visited on
1797 07/07/2025) (cit. on p. 15).
- 1798 [63] J. Goldstone, A. Salam, and S. Weinberg. *Broken Symmetries*. Phys. Rev. 127 (3
1799 1962), pp. 965–970 (cit. on p. 15).
- 1800 [64] J. Ellis. *Higgs Physics. 2013 European School of High-Energy Physics*. 2015, pp. 117–
1801 168. arXiv: 1312.5672 [hep-ph] (cit. on pp. 15, 16).

- 1802 [65] CDF Collaboration. *Search for New Physics in High-Mass Electron-Positron Events*
1803 *in $p\bar{p}$ Collisions at $\sqrt{s} = 1.96$ TeV.* Phys. Rev. Lett. 99 (17 2007), p. 171802. arXiv:
1804 0707.2524 [hep-ex] (cit. on p. 17).
- 1805 [66] M. Battaglia and G. Servant. *Four-top production and $t\bar{t}$ +missing energy events at*
1806 *multi TeV e^+e^- colliders.* Nuovo Cim. C 033N2 (2010), pp. 203–208. arXiv: 1005.4632
1807 [hep-ex] (cit. on p. 17).
- 1808 [67] N. Arkani-Hamed, A. G. Cohen, and H. Georgi. *Electroweak symmetry breaking from*
1809 *dimensional deconstruction.* Physics Letters B 513.1-2 (July 2001), pp. 232–240. arXiv:
1810 hep-ph/0105239 [hep-ph] (cit. on p. 17).
- 1811 [68] T. Han, H. E. Logan, B. McElrath, and L.-T. Wang. *Phenomenology of the little Higgs*
1812 *model.* Phys. Rev. D 67 (9 2003), p. 095004. arXiv: hep-ph/0301040 [hep-ph] (cit. on
1813 p. 17).
- 1814 [69] P. Langacker and M. Plümacher. *Flavor changing effects in theories with a heavy Z'*
1815 *boson with family nonuniversal couplings.* Phys. Rev. D 62 (1 2000), p. 013006. arXiv:
1816 hep-ph/0001204 [hep-ph] (cit. on p. 17).
- 1817 [70] P. Langacker. *The Physics of Heavy Z' Gauge Bosons.* Rev. Mod. Phys. 81 (2009),
1818 pp. 1199–1228. arXiv: 0801.1345 [hep-ph] (cit. on p. 17).
- 1819 [71] J. H. Kim, K. Kong, S. J. Lee, and G. Mohlabeng. *Probing TeV scale top-philic*
1820 *resonances with boosted top-tagging at the high luminosity LHC.* Phys. Rev. D 94 (3
1821 2016), p. 035023. arXiv: 1604.07421 [hep-ph] (cit. on pp. 17, 84).
- 1822 [72] P. J. Fox, I. Low, and Y. Zhang. *Top-philic Z' forces at the LHC.* Journal of High
1823 Energy Physics 2018.3 (Mar. 2018). ISSN: 1029-8479. arXiv: 1801.03505 [hep-ph]
1824 (cit. on p. 17).

- 1825 [73] CMS Collaboration. *Observation of four top quark production in proton-proton col-*
1826 *lisions at $\sqrt{s} = 13\text{TeV}$* . Physics Letters B 847 (2023), p. 138290. arXiv: 2305.13439
1827 [hep-ex] (cit. on p. 17).
- 1828 [74] G. Ferretti and D. Karateev. *Fermionic UV completions of composite Higgs models*.
1829 Journal of High Energy Physics 2014.3 (Mar. 2014). ISSN: 1029-8479 (cit. on p. 19).
- 1830 [75] L. Vecchi. *A dangerous irrelevant UV-completion of the composite Higgs*. JHEP 02
1831 (2017), p. 094. arXiv: 1506.00623 [hep-ph] (cit. on p. 19).
- 1832 [76] P. Sabatini. *Evidence for four-top-quarks production with the ATLAS detector at the*
1833 *Large Hadron Collider*. Tech. rep. Geneva: CERN, 2021. URL: <https://cds.cern.ch/record/2784150> (cit. on p. 20).
- 1835 [77] L. Evans and P. Bryant. *LHC Machine*. JINST 3 (2008), S08001 (cit. on p. 22).
- 1836 [78] CMS Collaboration. *The CMS Experiment at the CERN LHC*. JINST 3 (2008),
1837 S08004 (cit. on p. 22).
- 1838 [79] The ALICE Collaboration. *The ALICE experiment at the CERN LHC*. JINST 3
1839 (2008), S08002 (cit. on p. 22).
- 1840 [80] The LHCb Collaboration. *The LHCb Detector at the LHC*. JINST 3 (2008), S08005
1841 (cit. on p. 22).
- 1842 [81] E. e. a. Gschwendtner. *AWAKE, The Advanced Proton Driven Plasma Wakefield*
1843 *Acceleration Experiment at CERN*. Nuclear Instruments and Methods in Physics Re-
1844 search Section A 829 (2016), pp. 76–82. arXiv: 1512.05498 [physics.acc-ph] (cit. on
1845 p. 23).

- 1846 [82] J. L. Feng, I. Galon, F. Kling, and S. Trojanowski. *ForwArd Search ExpeRiment at*
1847 *the LHC*. Phys. Rev. D 97 (3 2018), p. 035001. arXiv: 1708.09389 [hep-ph] (cit. on
1848 p. 23).
- 1849 [83] The KATRIN collaboration. *The design, construction, and commissioning of the KA-*
1850 *TRIN experiment*. Journal of Instrumentation 16.08 (2021), T08015. arXiv: 2103.
1851 04755 [physics.ins-det] (cit. on p. 23).
- 1852 [84] E. Lopienska. *The CERN accelerator complex, layout in 2022*. General Photo. 2022.
1853 URL: <https://cds.cern.ch/record/2800984> (visited on 07/08/2025) (cit. on p. 23).
- 1854 [85] High Luminosity LHC Project Organization. *The HL-LHC project*. 2025. URL: <https://hilumilhc.web.cern.ch/content/hl-lhc-project> (visited on 06/11/2025) (cit. on
1855 p. 24).
- 1856 [86] ATLAS Collaboration. *Performance of the ATLAS detector using first collision data*.
1857 JHEP 09 (2010), p. 056. arXiv: 1005.5254 [hep-ex] (cit. on p. 24).
- 1859 [87] ATLAS Collaboration. *Luminosity determination in pp collisions at $\sqrt{s} = 13 \text{ TeV}$*
1860 *using the ATLAS detector at the LHC*. Eur. Phys. J. C 83 (2023), p. 982. arXiv:
1861 2212.09379 [hep-ex] (cit. on pp. 25, 50, 70).
- 1862 [88] J. M. Butterworth, G. Dissertori, and G. P. Salam. *Hard Processes in Proton-Proton*
1863 *Collisions at the Large Hadron Collider*. Annu. Rev. Nucl. Part. Sci. 62 (2012),
1864 pp. 387–405. arXiv: 1202.0583 [hep-ex] (cit. on p. 25).
- 1865 [89] J. Campbell, J. Huston, and W. J. Stirling. *Hard interactions of quarks and gluons:*
1866 *a primer for LHC physics*. Reports on Progress in Physics 70.1 (2006), p. 89. arXiv:
1867 hep-ph/0611148 [hep-ex] (cit. on p. 25).

- 1868 [90] ATLAS Collaboration. *Standard Model Summary Plots October 2023*. ATL-PHYS-
1869 PUB-2023-039. 2023. URL: <https://cds.cern.ch/record/2882448> (cit. on p. 26).
- 1870 [91] J. Pequenao and P. Schaffner. *How ATLAS detects particles: diagram of particle*
1871 *paths in the detector*. 2013. URL: <https://cds.cern.ch/record/1505342> (visited on
1872 07/08/2025) (cit. on p. 27).
- 1873 [92] J. Pequenao. *Computer generated image of the ATLAS inner detector*. 2008. URL:
1874 <https://cds.cern.ch/record/1095926> (visited on 07/08/2025) (cit. on p. 28).
- 1875 [93] J. Pequenao. *Computer Generated image of the ATLAS calorimeter*. 2008. URL: <https://cds.cern.ch/record/1095927> (visited on 07/08/2025) (cit. on p. 30).
- 1877 [94] ATLAS Collaboration. *Operation of the ATLAS trigger system in Run 2*. **JINST** 15
1878 (2020), P10004. arXiv: [2007.12539 \[physics.ins-det\]](https://arxiv.org/abs/2007.12539) (cit. on p. 33).
- 1879 [95] ATLAS Collaboration. *Performance of the ATLAS track reconstruction algorithms*
1880 *in dense environments in LHC Run 2*. **Eur. Phys. J. C** 77 (2017), p. 673. arXiv:
1881 [1704.07983 \[hep-ex\]](https://arxiv.org/abs/1704.07983) (cit. on p. 34).
- 1882 [96] T. Cornelissen et al. *Concepts, design and implementation of the ATLAS New Track-*
1883 *ing (NEWT)*. Tech. rep. Geneva: CERN, 2007. URL: <https://cds.cern.ch/record/1020106> (cit. on p. 34).
- 1885 [97] A. Salzburger. *Optimisation of the ATLAS Track Reconstruction Software for Run-2*.
1886 *Journal of Physics: Conference Series* 664.7 (2015), p. 072042 (cit. on p. 34).
- 1887 [98] R. Frühwirth. *Application of Kalman filtering to track and vertex fitting*. **Nucl. In-**
1888 *strum. Methods Phys. Res. A* 262.2 (1987), pp. 444–450. ISSN: 0168-9002 (cit. on
1889 p. 34).

- 1890 [99] T. Cornelissen et al. *The global χ^2 track fitter in ATLAS*. Journal of Physics: Con-
1891 ference Series 119.3 (2008), p. 032013 (cit. on p. 34).
- 1892 [100] ATLAS Collaboration. *Improved electron reconstruction in ATLAS using the Gaus-
1893 sian Sum Filter-based model for bremsstrahlung*. ATLAS-CONF-2012-047. 2012. URL:
1894 <https://cds.cern.ch/record/1449796> (cit. on p. 34).
- 1895 [101] D. Wicke. *A new algorithm for solving tracking ambiguities*. Tech. rep. Oct. 1998.
1896 URL: <https://cds.cern.ch/record/2625731> (cit. on p. 35).
- 1897 [102] ATLAS Collaboration. *Reconstruction of primary vertices at the ATLAS experiment
1898 in Run 1 proton–proton collisions at the LHC*. Eur. Phys. J. C 77 (2017), p. 332.
1899 arXiv: [1611.10235 \[physics.ins-det\]](https://arxiv.org/abs/1611.10235) (cit. on p. 35).
- 1900 [103] W. Waltenberger, R. Frühwirth, and P. Vanlaer. *Adaptive vertex fitting*. Journal of
1901 Physics G: Nuclear and Particle Physics 34.12 (2007), N343 (cit. on p. 35).
- 1902 [104] ATLAS Collaboration. *Secondary vertex finding for jet flavour identification with the
1903 ATLAS detector*. ATL-PHYS-PUB-2017-011. 2017. URL: <https://cds.cern.ch/record/2270366> (cit. on p. 35).
- 1905 [105] ATLAS Collaboration. *Performance of pile-up mitigation techniques for jets in pp
1906 collisions at $\sqrt{s} = 8 \text{ TeV}$ using the ATLAS detector*. Eur. Phys. J. C 76 (2016),
1907 p. 581. arXiv: [1510.03823 \[hep-ex\]](https://arxiv.org/abs/1510.03823) (cit. on pp. 36, 39).
- 1908 [106] ATLAS Collaboration. *Topological cell clustering in the ATLAS calorimeters and its
1909 performance in LHC Run 1*. Eur. Phys. J. C 77 (2017), p. 490. arXiv: [1603.02934](https://arxiv.org/abs/1603.02934)
1910 [hep-ex] (cit. on pp. 36, 37).

- 1911 [107] ATLAS Collaboration. *Jet reconstruction and performance using particle flow with*
1912 *the ATLAS Detector.* *Eur. Phys. J. C* **77** (2017), p. 466. arXiv: [1703.10485 \[hep-ex\]](#)
1913 (cit. on p. 38).
- 1914 [108] M. Cacciari, G. P. Salam, and G. Soyez. *The anti- k_t jet clustering algorithm.* *JHEP*
1915 **04** (2008), p. 063. arXiv: [0802.1189 \[hep-ph\]](#) (cit. on p. 38).
- 1916 [109] ATLAS Collaboration. *Jet energy scale and resolution measured in proton–proton*
1917 *collisions at $\sqrt{s} = 13\text{ TeV}$ with the ATLAS detector.* *Eur. Phys. J. C* **81** (2021),
1918 p. 689. arXiv: [2007.02645 \[hep-ex\]](#) (cit. on pp. 39, 72–74).
- 1919 [110] ATLAS Collaboration. *Jet energy scale measurements and their systematic uncertainties*
1920 *in proton–proton collisions at $\sqrt{s} = 13\text{ TeV}$ with the ATLAS detector.* *Phys. Rev.*
1921 **D 96** (2017), p. 072002. arXiv: [1703.09665 \[hep-ex\]](#) (cit. on pp. 39, 72).
- 1922 [111] ATLAS Collaboration. *Transforming jet flavour tagging at ATLAS.* Tech. rep. Sub-
1923 mitted to: Nature Communications. Geneva: CERN, 2025. arXiv: [2505.19689](#) (cit. on
1924 pp. 40–42).
- 1925 [112] A. Vaswani et al. *Attention Is All You Need.* 2023. arXiv: [1706.03762 \[cs.CL\]](#) (cit. on
1926 p. 40).
- 1927 [113] ATLAS Collaboration. *Measurements of b -jet tagging efficiency with the ATLAS de-*
1928 *tector using $t\bar{t}$ events at $\sqrt{s} = 13\text{ TeV}.$* *JHEP* **08** (2018), p. 089. arXiv: [1805.01845](#)
1929 [[hep-ex](#)] (cit. on pp. 42, 74).
- 1930 [114] ATLAS Collaboration. *Electron reconstruction and identification in the ATLAS ex-*
1931 *periment using the 2015 and 2016 LHC proton–proton collision data at $\sqrt{s} = 13\text{ TeV}.$*
1932 *Eur. Phys. J. C* **79** (2019), p. 639. arXiv: [1902.04655 \[physics.ins-det\]](#) (cit. on
1933 pp. 43–45).

- 1934 [115] ATLAS Collaboration. *Electron Identification with a Convolutional Neural Network*
1935 *in the ATLAS Experiment*. ATL-PHYS-PUB-2023-001. 2023. URL: <https://cds.cern.ch/record/2850666> (cit. on p. 45).
- 1936
1937 [116] ATLAS Collaboration. *Muon reconstruction and identification efficiency in ATLAS*
1938 *using the full Run 2 pp collision data set at $\sqrt{s} = 13 \text{ TeV}$* . *Eur. Phys. J. C* **81** (2021),
1939 p. 578. arXiv: [2012.00578 \[hep-ex\]](https://arxiv.org/abs/2012.00578) (cit. on pp. 46, 47).
- 1940 [117] ATLAS Collaboration. *Muon reconstruction performance of the ATLAS detector in*
1941 *proton–proton collision data at $\sqrt{s} = 13 \text{ TeV}$* . *Eur. Phys. J. C* **76** (2016), p. 292. arXiv:
1942 [1603.05598 \[hep-ex\]](https://arxiv.org/abs/1603.05598) (cit. on p. 47).
- 1943 [118] ATLAS Collaboration. *Performance of missing transverse momentum reconstruction*
1944 *with the ATLAS detector using proton–proton collisions at $\sqrt{s} = 13 \text{ TeV}$* . *Eur. Phys.*
1945 *J. C* **78** (2018), p. 903. arXiv: [1802.08168 \[hep-ex\]](https://arxiv.org/abs/1802.08168) (cit. on pp. 48, 74).
- 1946 [119] ATLAS Collaboration. *E_T^{miss} performance in the ATLAS detector using 2015–2016*
1947 *LHC pp collisions*. ATLAS-CONF-2018-023. 2018. URL: <https://cds.cern.ch/record/2625233> (cit. on p. 49).
- 1948
1949 [120] J. Alwall et al. *The automated computation of tree-level and next-to-leading order*
1950 *differential cross sections, and their matching to parton shower simulations*. *JHEP* **07**
1951 (2014), p. 079. arXiv: [1405.0301 \[hep-ph\]](https://arxiv.org/abs/1405.0301) (cit. on pp. 51, 53, 54).
- 1952 [121] NNPDF Collaboration, R. D. Ball, et al. *Parton distributions for the LHC run II*.
1953 *JHEP* **04** (2015), p. 040. arXiv: [1410.8849 \[hep-ph\]](https://arxiv.org/abs/1410.8849) (cit. on pp. 51, 53, 54).
- 1954 [122] T. Sjöstrand et al. *An introduction to PYTHIA 8.2*. *Comput. Phys. Commun.* **191**
1955 (2015), p. 159. arXiv: [1410.3012 \[hep-ph\]](https://arxiv.org/abs/1410.3012) (cit. on pp. 51, 53, 54).

- 1956 [123] ATLAS Collaboration. *ATLAS Pythia 8 tunes to 7 TeV data*. ATL-PHYS-PUB-2014-
1957 021. 2014. URL: <https://cds.cern.ch/record/1966419> (cit. on pp. 53, 54).
- 1958 [124] S. Frixione, E. Laenen, P. Motylinski, and B. R. Webber. *Angular correlations of*
1959 *lepton pairs from vector boson and top quark decays in Monte Carlo simulations*.
1960 JHEP 04 (2007), p. 081. arXiv: [hep-ph/0702198](https://arxiv.org/abs/hep-ph/0702198) (cit. on p. 53).
- 1961 [125] P. Artoisenet, R. Frederix, O. Mattelaer, and R. Rietkerk. *Automatic spin-entangled*
1962 *decays of heavy resonances in Monte Carlo simulations*. JHEP 03 (2013), p. 015.
1963 arXiv: [1212.3460 \[hep-ph\]](https://arxiv.org/abs/1212.3460) (cit. on p. 53).
- 1964 [126] D. J. Lange. *The EvtGen particle decay simulation package*. Nucl. Instrum. Meth. A
1965 462 (2001), p. 152 (cit. on p. 53).
- 1966 [127] R. Frederix, D. Pagani, and M. Zaro. *Large NLO corrections in $t\bar{t}W^\pm$ and $t\bar{t}t\bar{t}$*
1967 *hadroproduction from supposedly subleading EW contributions*. JHEP 02 (2018), p. 031.
1968 arXiv: [1711.02116 \[hep-ph\]](https://arxiv.org/abs/1711.02116) (cit. on pp. 53, 76).
- 1969 [128] E. Bothmann et al. *Event generation with Sherpa 2.2*. SciPost Phys. 7.3 (2019), p. 034.
1970 arXiv: [1905.09127 \[hep-ph\]](https://arxiv.org/abs/1905.09127) (cit. on pp. 53, 54).
- 1971 [129] S. Schumann and F. Krauss. *A parton shower algorithm based on Catani–Seymour*
1972 *dipole factorisation*. JHEP 03 (2008), p. 038. arXiv: [0709.1027 \[hep-ph\]](https://arxiv.org/abs/0709.1027) (cit. on
1973 p. 53).
- 1974 [130] S. Höche, F. Krauss, M. Schönher, and F. Siegert. *A critical appraisal of NLO+PS*
1975 *matching methods*. JHEP 09 (2012), p. 049. arXiv: [1111.1220 \[hep-ph\]](https://arxiv.org/abs/1111.1220) (cit. on p. 53).
- 1976 [131] S. Höche, F. Krauss, M. Schönher, and F. Siegert. *QCD matrix elements + parton*
1977 *showers. The NLO case*. JHEP 04 (2013), p. 027. arXiv: [1207.5030 \[hep-ph\]](https://arxiv.org/abs/1207.5030) (cit. on
1978 p. 53).

- 1979 [132] S. Catani, F. Krauss, B. R. Webber, and R. Kuhn. *QCD Matrix Elements + Parton
Showers*. JHEP 11 (2001), p. 063. arXiv: [hep-ph/0109231](#) (cit. on p. 53).
- 1980
- 1981 [133] S. Höche, F. Krauss, S. Schumann, and F. Siegert. *QCD matrix elements and truncated
showers*. JHEP 05 (2009), p. 053. arXiv: [0903.1219 \[hep-ph\]](#) (cit. on p. 53).
- 1982
- 1983 [134] F. Cascioli, P. Maierhöfer, and S. Pozzorini. *Scattering Amplitudes with Open Loops*.
Phys. Rev. Lett. 108 (2012), p. 111601. arXiv: [1111.5206 \[hep-ph\]](#) (cit. on p. 53).
- 1984
- 1985 [135] A. Denner, S. Dittmaier, and L. Hofer. *COLLIER: A fortran-based complex one-loop
library in extended regularizations*. Comput. Phys. Commun. 212 (2017), pp. 220–238.
arXiv: [1604.06792 \[hep-ph\]](#) (cit. on p. 53).
- 1986
- 1987
- 1988 [136] F. Buccioni et al. *OpenLoops 2*. Eur. Phys. J. C 79.10 (2019), p. 866. arXiv: [1907.13071
\[hep-ph\]](#) (cit. on p. 53).
- 1989
- 1990 [137] ATLAS Collaboration. *ATLAS data quality operations and performance for 2015–
2018 data-taking*. JINST 15 (2020), P04003. arXiv: [1911.04632 \[physics.ins-det\]](#)
(cit. on p. 55).
- 1991
- 1992
- 1993 [138] ATLAS Collaboration. *Analysis of $t\bar{t}H$ and $t\bar{t}W$ production in multilepton final states
with the ATLAS detector*. ATLAS-CONF-2019-045. 2019. URL: <https://cds.cern.ch/record/2693930> (cit. on pp. 62, 65, 78).
- 1994
- 1995
- 1996 [139] ATLAS Collaboration. *Measurement of the total and differential cross-sections of $t\bar{t}W$
production in pp collisions at $\sqrt{s} = 13$ TeV with the ATLAS detector*. JHEP 05 (2024),
p. 131. arXiv: [2401.05299 \[hep-ex\]](#) (cit. on p. 62).
- 1997
- 1998
- 1999 [140] ATLAS Collaboration. *Search for new phenomena in events with same-charge leptons
and b -jets in pp collisions at $\sqrt{s} = 13$ TeV with the ATLAS detector*. JHEP 12 (2018),
p. 039. arXiv: [1807.11883 \[hep-ex\]](#) (cit. on p. 65).
- 2000
- 2001

- 2002 [141] ATLAS Collaboration. *Search for R-parity-violating supersymmetry in a final state*
2003 *containing leptons and many jets with the ATLAS experiment using $\sqrt{s} = 13 \text{ TeV}$*
2004 *proton–proton collision data.* *Eur. Phys. J. C* **81** (2021), p. 1023. arXiv: [2106.09609](https://arxiv.org/abs/2106.09609)
2005 [[hep-ex](#)] (cit. on p. 68).
- 2006 [142] E. Gerwick, T. Plehn, S. Schumann, and P. Schichtel. *Scaling Patterns for QCD Jets.*
2007 *JHEP* **10** (2012), p. 162. arXiv: [1208.3676](https://arxiv.org/abs/1208.3676) [[hep-ph](#)] (cit. on p. 68).
- 2008 [143] G. Avoni et al. *The new LUCID-2 detector for luminosity measurement and moni-*
2009 *toring in ATLAS.* *JINST* **13.07** (2018), P07017 (cit. on p. 70).
- 2010 [144] ATLAS Collaboration. *Tagging and suppression of pileup jets.* ATL-PHYS-PUB-2014-
2011 001. 2014. URL: <https://cds.cern.ch/record/1643929> (cit. on pp. 72, 74).
- 2012 [145] ATLAS Collaboration. *Measurements of inclusive and differential fiducial cross-sections*
2013 *of $t\bar{t}$ production with additional heavy-flavour jets in proton–proton collisions at $\sqrt{s} =$*
2014 *13 TeV with the ATLAS detector.* *JHEP* **04** (2019), p. 046. arXiv: [1811.12113](https://arxiv.org/abs/1811.12113) [[hep-ex](#)]
2015 (cit. on p. 76).
- 2016 [146] D. de Florian et al. *Handbook of LHC Higgs Cross Sections: 4. Deciphering the Nature*
2017 *of the Higgs Sector.* CERN Yellow Rep. Monogr. **2** (2017), pp. 1–869. arXiv: [1610.07922](https://arxiv.org/abs/1610.07922) [[hep-ph](#)] (cit. on p. 76).
- 2019 [147] ATLAS Collaboration. *Measurement of the production cross-section of a single top*
2020 *quark in association with a Z boson in proton–proton collisions at 13 TeV with the*
2021 *ATLAS detector.* ATLAS-CONF-2017-052. 2017. URL: <https://cds.cern.ch/record/2273868> (cit. on p. 76).

- 2023 [148] F. Demartin, B. Maier, F. Maltoni, K. Mawatari, and M. Zaro. *tWH associated*
2024 *production at the LHC.* EPJC 77.1 (2017). arXiv: 1607.05862 [hep-ph]. URL: <https://doi.org/10.1140/epjc/s10052-017-4601-7> (cit. on p. 76).
- 2025
- 2026 [149] ATLAS Collaboration. *Measurement of $W^\pm Z$ production cross sections and gauge*
2027 *boson polarisation in pp collisions at $\sqrt{s} = 13 \text{ TeV}$ with the ATLAS detector.* Eur.
2028 Phys. J. C 79 (2019), p. 535. arXiv: 1902.05759 [hep-ex] (cit. on p. 76).
- 2029 [150] G. Cowan, K. Cranmer, E. Gross, and O. Vitells. *Asymptotic formulae for likelihood-*
2030 *based tests of new physics.* The European Physical Journal C 71.2 (Feb. 2011). ISSN:
2031 1434-6052. arXiv: 1007.1727 [physics.data-an]. URL: <http://dx.doi.org/10.1140/epjc/s10052-011-1554-0> (cit. on p. 80).
- 2032
- 2033 [151] J. Neyman and E. S. Pearson. *IX. On the problem of the most efficient tests of*
2034 *statistical hypotheses.* Philosophical Transactions of the Royal Society of London.
2035 Series A, Containing Papers of a Mathematical or Physical Character 231.694-706
2036 (1933), pp. 289–337 (cit. on p. 80).
- 2037 [152] S. S. Wilks. *The large-sample distribution of the likelihood ratio for testing composite*
2038 *hypotheses.* Annals of Mathematical Statistics 9.1 (1938), pp. 60–62 (cit. on p. 81).
- 2039 [153] T. Junk. *Confidence level computation for combining searches with small statistics.*
2040 Nuclear Instruments and Methods in Physics Research Section A: Accelerators, Spec-
2041 *rometers, Detectors and Associated Equipment* 434.23 (Sept. 1999), 435443. ISSN:
2042 0168-9002. arXiv: hep-ex/9902006 [hep-ex] (cit. on p. 82).
- 2043 [154] A. L. Read. *Modified frequentist analysis of search results: The CLs method.* Tech.
2044 rep. CERN-OPEN-2000-205. Presented at Workshop on Confidence Limits, Geneva,
2045 Switzerland. CERN, 2000. URL: <https://cds.cern.ch/record/451614> (cit. on p. 82).